

INFORMATION TO USERS

This manuscript has been reproduced from the microfilm master. UMI films the text directly from the original or copy submitted. Thus, some thesis and dissertation copies are in typewriter face, while others may be from any type of computer printer.

The quality of this reproduction is dependent upon the quality of the copy submitted. Broken or indistinct print, colored or poor quality illustrations and photographs, print bleedthrough, substandard margins, and improper alignment can adversely affect reproduction.

In the unlikely event that the author did not send UMI a complete manuscript and there are missing pages, these will be noted. Also, if unauthorized copyright material had to be removed, a note will indicate the deletion.

Oversize materials (e.g., maps, drawings, charts) are reproduced by sectioning the original, beginning at the upper left-hand corner and continuing from left to right in equal sections with small overlaps. Each original is also photographed in one exposure and is included in reduced form at the back of the book.

Photographs included in the original manuscript have been reproduced xerographically in this copy. Higher quality 6" x 9" black and white photographic prints are available for any photographs or illustrations appearing in this copy for an additional charge. Contact UMI directly to order.

UMI

A Bell & Howell Information Company
300 North Zeeb Road, Ann Arbor MI 48106-1346 USA
313/761-4700 800/521-0600

**The Top Quark
in Muon + Jet Events
From 1.8 TeV Proton–Antiproton
Collisions**

A Dissertation

Submitted to the Graduate Division of the
University of Hawaii in Partial Fulfillment of the
Requirements for the Degree of

Doctor of Philosophy

In

Physics

May 1996

By

Cary Y. Yoshikawa

Dissertation Committee:

Michael W. Peters, Chairperson

Frederick A. Harris

Xerxes R. Tata

Pui K. Lam

David D. Bleecker

UMI Number: 9629868

UMI Microform 9629868
Copyright 1996, by UMI Company. All rights reserved.
This microform edition is protected against unauthorized
copying under Title 17, United States Code.

UMI
300 North Zeeb Road
Ann Arbor, MI 48103

Dedication

To Colleen, Emily, and mom . . .

Acknowledgements

There are so many people to whom I am indebted who have, in one way or another, contributed to the completion of this endeavor. My first thanks has to go to Mike Peters for giving me the opportunity to collaborate with DØ. Mike's vigorous attention to detail and correctness in the development of his top quark mass analysis instilled in me the energy and dedication I used in the analyses presented in this thesis.

The two people I owe my greatest thanks to are Mike Jones and Joey Thompson. Mike's relative frequent trips to Fermilab forced upon him the role of being my remote advisor. Mike's help spanned the entire spectrum—from resolving the most complex issues in very convoluted and complicated analyses to secretarial tasks of making copies available to those in Hawaii interested in this work. Among his many talents, Joey was an inexhaustible resource regarding anything related to events with muon + jets. He was the first person in the trenches in this analysis and I have greatly benefitted from his long-lasting scars.

When I first arrived at Fermilab in 1990, Nobu Oshima graciously took me under his wings and taught me something about every aspect of what physicists *really* do. (I found out many of them fly planes.) Throughout the years, Nobu would check up on me to make sure my agenda was focused. For all this I am grateful to have met Nobu Oshima.

I would like to thank Susumu Igarashi whom I had the pleasure of working with on the muon monitoring system. His easy-going nature provided a proper perspective in a sometimes acrimonious environment.

Serban Protopopescu is the person most responsible for my choice of thesis topic. Early on (~ 1991), Serban had written code to analyze top quark events in the lepton + jets channels. I found the physics in the code to be so interesting, I knew I wanted to pursue this type of analysis. Serban has also been an authoritative resource for understanding any type of physical process.

During the earliest stages of my top quark mass analysis (*a la* Dalitz–Goldstein), Andrzej and Daria Zieminski and Jim Green were invaluable sources of physics knowledge. In the middle (matured Dalitz–Goldstein) to latter (using H_T) stages of the mass analysis, Tom Ferbel was always there to offer constructive help.

Jim Linnemann was very crucial to the success of the grid search. Harrison Prosper and Chip Stewart were instrumental to many ideas surrounding the grid search and the mass analysis, as well.

I would like to express many thanks to Bob Kehoe who was a bottomless (thank God not topless, *really*) resource regarding anything reconstructed with the calorimeter. In the same breath, I must also thank God, again, for not getting shot at while being a passenger in the rental car driven by Bob in California during the 1995 SLAC Summer School.

I would also like to thank John Hobbs for finishing the work started by Steve Wimpenny's team (Jim Cochran, Joey Thompson, ...) in dealing with one of the most complicated issues at $D\bar{0}$, standardizing the identification of muons.

Shuichi Kunori took an interest in my work as it matured and asked many probing questions that resulted in a better understanding of the analyses. Ryuji Yamada was always there to keep me hip with the latest happenings around the lab regarding the top quark.

I have greatly benefitted from several discussions about my analyses with the core group of the lunchroom crowd: David Cullen-Vidal, Freedy (the first e is silent) Nang, and Jim Jaques. More importantly is the friendship developed over the years that includes the rest of the lunch crowd—Brad Abbot, Tom Fahland, and a newcomer, Bryan Lauer. Speaking of friendships, the list would by no means be close to complete without the mention of Gene Alvarez, who taught me the game of basketball as it is played in New York—which explains his dedication to martial arts and lack of any practice in shooting the ball.

I also value the friendship developed within the Hawaii group at DØ with John Balderston and Mary Anne Cummings.

I would like to acknowledge the best teacher I've ever had, Mrs. Lois Takemori. An experiment employing cold air to crush a steel container impressed this stompin' third grader who couldn't put a dent in it. In the sixth grade, Mrs. Takemori offered to teach me algebra after school. Infringing on my play time, I, of course, declined the opportunity. I only came to appreciate her dedication after I had taught a few classes of my own. Whether or not I do become an educator, Mrs. Takemori's excellence and dedication has set the standard I can only strive for.

Finally, no achievement would be worthwhile without the love and support of my wife Colleen and the rest of my family. Because of my mother's total dedication to her two sons, I am sure she will find as much gratification as I do, if not more. But, foremost, I thank Colleen for putting up with this manic-depressive who repeatedly found the top quark at least 20 times over the past few years, only to be recanted at least 19 times because of some problem. Notwithstanding the years on the emotional roller coaster, Colleen has given me a most precious bundle of joy, Emily. I am truly blessed.

Abstract

An optimized search for the top (or truth) quark is performed in $t\bar{t} \rightarrow \mu +$ jet events produced by $p\bar{p}$ collisions with $\sqrt{s} = 1.8$ TeV at the Fermilab Tevatron and observed with the DØ detector. The data set analyzed is identical to that used by the DØ Collaboration in its reported discovery of the top quark which engaged other decay channels as well.¹ Four events are observed with an expected background of 1.40 ± 0.71 events. The probability for an upward fluctuation of the background to produce the observed number of events is 0.081 (equivalent to 1.7 standard deviations). An analysis for the top quark mass is carried out based on the amount of jet activity transverse to the $p\bar{p}$ beam direction. The resultant top quark mass value is measured to be $185_{-26}^{+16}(\text{stat.})_{-8}^{+6}(\text{syst.})$ GeV/c² with a corresponding production cross section of 5.3 ± 4.4 pb.

Contents

Dedication	iii
Acknowledgements	iv
Abstract	vii
List of Tables	xi
List of Figures	xiii
1 Introduction	1
1.1 The Standard Model	2
1.1.1 The Elementary Particles and Their Interactions	3
1.1.2 Symmetries in the Formulation of the Standard Model	7
1.2 Motivation For Existence of the Top Quark	24
1.2.1 Renormalizability of the Electroweak Theory	25
1.2.2 Test of B Quark Being an $SU_L(2)$ Doublet	25
1.2.3 Test of B Quark Being an $SU_L(2)$ Singlet	26
1.2.4 Examination of the Last Surviving Topless Model	27
1.3 Standard Model Constraint on M_{top}	28
1.4 Is Top the Last Quark?	29
1.5 Production and Decay of the Top Quark	30
2 The Apparatus	34
2.1 The Accelerator	34
2.2 The Coordinate System at DØ	37
2.3 The DØ Detector	38

2.3.1	Central Detectors	42
2.3.2	Calorimeters	50
2.3.3	Muon Detectors	57
3	Data Collection and Particle Identification	64
3.1	Data Collection	64
3.2	Particle Reconstruction and Identification	66
3.2.1	Jets	66
3.2.2	Missing Transverse Energy	71
3.2.3	Muons	73
3.3	Luminosity	78
4	Search For the Top Quark	79
4.1	Description of Top and Its Backgrounds	80
4.1.1	Top Quark Events	80
4.1.2	W + Jets Background	81
4.1.3	QCD Background	82
4.1.4	Z + Jets Background	85
4.2	The Variables	86
4.3	Calculation of the Number of Top and Background Events	97
4.3.1	Top Quark Events	98
4.3.2	W + Jets Background	99
4.3.3	QCD Background	101
4.3.4	Z + Jets Background	102
4.4	Derivation of Optimal Selection Cuts (Grid Search)	104
4.4.1	General Discussion	104
4.4.2	Application to $t\bar{t} \rightarrow \mu + \text{Jet}$ Events	106
4.5	Application of Optimal Cuts to Data	109

5 Top Quark Mass Analysis	114
5.1 Explanation of the Technique and Its Error	115
5.1.1 Parameterization of H_T	115
5.1.2 Mass Extraction Procedure	117
5.2 Application To Data	119
5.2.1 Best Fit Top Mass Value and Its Statistical Error	119
5.2.2 Error Attributed to the Method	120
5.2.3 Error Due to Uncertainty of Jet Energy Scale	123
5.2.4 Error Due to Uncertainty in Top Quark MC Generator	124
5.2.5 Top Quark Mass Result	126
6 Conclusions	128
A Verification of VECBOS MC Jet Activity With Data	130
B Comparison Between a Cut in E_T^{min} and a Contour Cut in $\Delta\phi(\vec{\mu}, \vec{E}_T) - E_T$ Space	132
C Dependence of Optimal Selection Cut Values and Its Validity on $\int \mathcal{L} dt$	135
D Optimization Probability Projected In Pairs of Variables	137
E Candidate Events	151
F Fitting Results For Most Probable Top Mass Values From Simulated Experiments	153
Bibliography	157

List of Tables

1.1	Particles in the (Minimal) Standard Model	3
1.2	The partial and total widths of the Z as predicted by the Standard Model and the Ma Model and their comparison to the measured values.	28
1.3	Summary of probability for various decay modes of the $t\bar{t}$ system.	33
2.1	Tevatron Parameters.	37
2.2	VTX detector parameters.	44
2.3	CDC detector parameters.	48
2.4	FDC detector parameters.	50
2.5	Central Calorimeter Module Parameters.	54
2.6	End Calorimeter Module Parameters.	55
2.7	Muon Detector Parameters.	63
3.1	Jet energy resolution parameters.	71
4.1	Examples of upper and lower limits for measured μ momenta.	84
4.2	Trigger and reconstruction μ efficiencies.	99
4.3	Range and granularity for each quantity in the Grid Search.	106
4.4	Optimal cut values resulting from the Grid Search.	106
4.5	Cut efficiencies for top events.	107
4.6	Expected number of signal and background events passing optimal cuts.	107
4.7	Values of variables for candidate events.	110
4.8	Cross Section values of excess events for different top quark masses.	112
5.1	H_T values of candidate events	119
5.2	RMS of m_{top}^{fit} for simulated experiments.	121

5.3	Most probable m_{top} from the simulated experiments and the resulting estimated systematic error due to the method.	123
5.4	Effect of jet energy scale uncertainty on top quark mass result . . .	124
6.1	Summary of discoveries of the top quark by DØ and CDF, with supporting evidence from this analysis.	129
B.1	Comparison between \cancel{E}_T^{min} cut and contour cut for rejection of events with poorly measured μ momenta and efficiency of top MC.	133
C.1	Optimal cut values resulting from the Grid Search for two cases of $\int \mathcal{L} dt$	135
C.2	Expected number of signal and background events passing optimal cuts designed for two cases of $\int \mathcal{L} dt$	136
E.1	Four-vector of objects in Run 58192, Event 137.	151
E.2	Four-vector of objects in Run 58203, Event 4980.	151
E.3	Four-vector of objects in Run 63183, Event 13926.	152
E.4	Four-vector of objects in Run 82694, Event 25595.	152
F.1	Means of fitted gaussian functions on simulated experiments generated with $m_{top} = 160 \text{ GeV}/c^2$	154
F.2	Means of fitted gaussian functions on simulated experiments generated with $m_{top} = 180 \text{ GeV}/c^2$	155
F.3	Means of fitted gaussian functions on simulated experiments generated with $m_{top} = 200 \text{ GeV}/c^2$	156

List of Figures

1.1	Feynman diagrams illustrating the strong force.	5
1.2	Feynman diagrams illustrating the electromagnetic force.	6
1.3	Feynman diagrams illustrating the weak force.	6
1.4	Dynamics of $SU_C(3)$ group.	9
1.5	Feynman diagrams illustrating the charge changing weak current. . .	12
1.6	Dynamics of $SU_L(2)$ group.	13
1.7	Example of an anomaly in the Standard Model.	24
1.8	Interference of $\gamma - Z$ in $e^+e^- \rightarrow b\bar{b}$	25
1.9	Hypothetical b-quark decay for left-handed b singlets.	26
1.10	The Standard Model relation between m_{top} , m_W , and m_H	29
1.11	Lowest order $t\bar{t}$ production processes.	31
1.12	Next to leading order calculation for fractional contributions of $q\bar{q} \rightarrow t\bar{t}$ and $gg \rightarrow t\bar{t}$ processes in $t\bar{t}$ production.	31
1.13	Theoretical $t\bar{t}$ production cross section.	32
1.14	Topology of $t\bar{t}$ production and decay.	33
2.1	An overview of the Fermilab accelerator complex with the DØ and CDF detectors.	35
2.2	An overall view of the DØ detector.	40
2.3	Schematic of the Central Detectors.	42
2.4	Endview of a quadrant of the VTX.	44
2.5	Endview of an azimuthal slice of the TRD's conversion and detection regions for one layer.	46
2.6	Endview of an azimuthal slice of the CDC.	47
2.7	dE/dx for one and two tracks in the CDC.	48
2.8	Exploded view of the FDC.	49

2.9	Isometric view of the CC and two ECs along with the CD encased within.	51
2.10	Typical calorimeter cell.	53
2.11	Side view of a quarter of the calorimeter and tracking chambers. . .	56
2.12	Nuclear interaction lengths vs. polar angle.	57
2.13	Side view of the DØ detector showing the five toroids and three layers of PDT muon chambers.	58
2.14	Endview of a WAMUS B/C chamber showing the stagger of the cells.	60
2.15	The WAMUS cell cathode pad.	60
2.16	Schematic of the end view of a single WAMUS cell with its equipotential surfaces.	61
2.17	Cross section and PDT configurations of a SAMUS chamber.	62
3.1	Jet energy scale correction as a function of the jet E_T , $R_{had}(E_T)$. . .	69
3.2	Resolution of \cancel{E}_T^{cal} determined from minimum bias data.	72
4.1	Feynman diagram of $t\bar{t}$ production and decay to μ + jets.	81
4.2	Feynman diagram of W + Jets background.	83
4.3	Feynman diagram of QCD background.	84
4.4	Feynman diagram of Z + Jets background.	86
4.5	Distribution of $\eta(\mu)$ for Top(180).	89
4.6	Distribution of $P_T(\mu)$ for Top(180) and its backgrounds.	89
4.7	Distribution of \cancel{E}_T for Top(180) and its backgrounds.	90
4.8	Geometry for \cancel{E}_T^{min} variable.	91
4.9	Distribution of \cancel{E}_T^{min} for Top(180) and its backgrounds.	92
4.10	Distribution of \cancel{E}_T^{cal} for Top(180) and its backgrounds.	93
4.11	Distribution of η for four highest E_T jets in Top(180).	94
4.12	Distribution of E_T^{Jet4} for Top(180) and its backgrounds.	94
4.13	Distribution of H_T for Top(180) and its backgrounds.	95

4.14	Distribution of \mathcal{A} for Top(180) and its backgrounds.	97
4.15	Jet multiplicity distribution in $W(\rightarrow e + \nu) + \text{jet MC events}$, $W(\rightarrow e + \nu) + \text{jet real data events}$, and QCD real data events. . . .	100
4.16	Cumulative probability lego plots in H_T and \cancel{E}_T^{cal}	108
4.17	Consistency check of the jet scaling assumption with \cancel{E}_T^{cal}	109
4.18	\cancel{E}_T^{cal} vs. H_T for real data passing loose cuts.	111
4.19	\mathcal{A} vs. \cancel{E}_T^{min} for real data passing loose cuts.	111
4.20	Cross Section of excess events as a function of top quark mass. . . .	113
5.1	Feynman diagram of gluon radiation within the $t\bar{t}$ system	115
5.2	H_T of top events	116
5.3	Fit of the double gaussian parameters for the top mass dependence	117
5.4	H_T probability density curves for top and background	118
5.5	Result of fit for candidate events to the mass likelihood function	120
5.6	RMS(H_T) for simulated experiments.	121
5.7	Top mass of best fit to the likelihood function for 1000 simulated experiments and samples of fits for the most probable m_{top} values. . . .	122
5.8	Effect of jet energy scale uncertainty on top quark mass result	125
5.9	H_T of HERWIG MC top events	126
5.10	HERWIG result of fit for candidate events to the mass likelihood function	127
A.1	Verification of VECBOS MC jet activity with data	131
B.1	Effect of \cancel{E}_T^{min} and contour cuts in $\Delta\phi(\vec{\mu}, \vec{\cancel{E}}_T) - \cancel{E}_T$ space for real data with a nonisolated μ and for top MC.	134
D.1	Optimization probability for \cancel{E}_T^{cal} vs. $P_T(\mu)$	138
D.2	Optimization probability for \cancel{E}_T vs. $P_T(\mu)$	139
D.3	Optimization probability for \cancel{E}_T^{min} vs. $P_T(\mu)$	139
D.4	Optimization probability for E_T^{Jet4} vs. $P_T(\mu)$	140

D.5	Optimization probability for H_T vs. $P_T(\mu)$	140
D.6	Optimization probability for \mathcal{A} vs. $P_T(\mu)$	141
D.7	Optimization probability for \cancel{E}_T vs. \cancel{E}_T^{cal}	141
D.8	Optimization probability for \cancel{E}_T^{min} vs. \cancel{E}_T^{cal}	142
D.9	Optimization probability for E_T^{Jet4} vs. \cancel{E}_T^{cal}	143
D.10	Optimization probability for H_T vs. \cancel{E}_T^{cal}	144
D.11	Optimization probability for \mathcal{A} vs. \cancel{E}_T^{cal}	144
D.12	Optimization probability for \cancel{E}_T^{min} vs. \cancel{E}_T	145
D.13	Optimization probability for E_T^{Jet4} vs. \cancel{E}_T	145
D.14	Optimization probability for H_T vs. \cancel{E}_T	146
D.15	Optimization probability for \mathcal{A} vs. \cancel{E}_T	146
D.16	Optimization probability for E_T^{Jet4} vs. \cancel{E}_T^{min}	147
D.17	Optimization probability for H_T vs. \cancel{E}_T^{min}	147
D.18	Optimization probability for \mathcal{A} vs. \cancel{E}_T^{min}	148
D.19	Optimization probability for H_T vs. E_T^{Jet4}	149
D.20	Optimization probability for \mathcal{A} vs. E_T^{Jet4}	150
D.21	Optimization probability for \mathcal{A} vs. H_T	150
F.1	Fits used in determining the most probable outcome for the 1000 simulated experiments generated with $m_{top} = 160$ GeV/ c^2	153
F.2	Fits used in determining the most probable outcome for the 1000 simulated experiments generated with $m_{top} = 180$ GeV/ c^2	154
F.3	Fits used in determining the most probable outcome for the 1000 simulated experiments generated with $m_{top} = 200$ GeV/ c^2	155

Chapter 1

Introduction

Scientists have always pondered two of the most fundamental questions of nature:

1. What are the most elementary constituents of matter?
2. How do these constituents interact with one another?

Today, the best theory that explains the observed phenomena is known as the Standard Model. Up to the beginning of 1995, there had been two (actually three) particles that had not been directly observed which are predicted to exist by the Standard Model. They are the Higgs boson and the top quark (and ν_τ). However, in March 1995, the DØ¹ and CDF² collaborations claimed discovery of the top quark, also known as the *truth* quark. This thesis presents the strategy behind the optimization in the discovery of the top quark by DØ¹ as well as an independent determination for its mass value. The analysis here evaluates the same data set used in the DØ result for the $t\bar{t} \rightarrow \mu + \text{jets}$ (with and without b-tag) channels, but results in different cut values as well as a slightly altered list of candidate events. The discrepancies are attributed to a modified list of variables as well as the involvement of *all* variables in the optimization.

The structure of this thesis will be to first briefly review, in Chapter 1, the Standard Model and some of its symmetries that pertain to the motivation that the top quark should exist, even before its announcement in March 1995. More

background information about the production and decay of the top quark is also presented here. Chapter 2 explains the experimental apparatus (accelerator and detector) in this study while the following chapter describes the identification of particles. Descriptions of the signal ($t\bar{t} \rightarrow \mu+\text{jets}$) and its various backgrounds begin chapter 4. This is followed with the optimized search resulting in a handful of candidate events. These events are then used to extract a mass value for the top quark in chapter 5. The final chapter summarizes the result of the search for the top quark and its mass value.

1.1 The Standard Model

The Standard Model is the currently accepted description for the ultimate constituents of matter and their interactions with one another. It is able to explain three of the four known forces down to distance scales of the order $\sim 10^{-18}$ m. The three forces are the strong, electromagnetic, and weak. The latter two have been unified into the electroweak force. The fourth remaining force which the standard model neglects is the gravitational force. It is believed that the gravitational force between elementary particles is so weak that it is negligible compared to the other three forces until the distance scale is of the order $\sim 10^{-35}$ m. Furthermore, attempts to quantize gravity result in a nonrenormalizable theory, unable to provide quantitative predictions. As it is irrelevant for the considerations here, the gravitational force will not be discussed any further.

1.1.1 The Elementary Particles and Their Interactions

All of matter is thought to be made up of quarks, leptons, gauge bosons, and the Higgs scalar particle. (Practically speaking, normal matter is made up of the up and down quarks and the electron.) These particles and some of their properties are listed in Table 1.1. The quarks interact via all three types of forces: the strong, electromagnetic, and weak. Leptons, on the other hand, only exhibit the electromagnetic and weak interactions. Within the lepton family, the electrically neutral neutrinos (ν 's) can interact only via the weak force.

Table 1.1: Particles in the (Minimal) Standard Model.³

(a) Weak isospin pertains only to the left-handed helicity states of the quarks and leptons. The right-handed components of quarks and charged leptons do not possess any weak isospin.

(b) Not observed yet.

(c) The gluon possesses eight combinations of the R,G,B color charges.

Particle Class	Particle Name	Mass (GeV/c ²)	Spin	Weak Isospin ^(a)	Charge	
					Electric	Color
Quarks	u	0.002 to 0.008	1/2	+1/2	+2/3	R,G,B
	d	0.005 to 0.015	1/2	-1/2	-1/3	R,G,B
	c	1.0 to 1.6	1/2	+1/2	+2/3	R,G,B
	s	0.100 to 0.300	1/2	-1/2	-1/3	R,G,B
	t	163 to 228	1/2	+1/2	+2/3	R,G,B
	b	4.1 to 4.5	1/2	-1/2	-1/3	R,G,B
Leptons	ν_e	0	1/2	+1/2	0	-
	e	5.11×10^{-4}	1/2	-1/2	-1	-
	ν_μ	0	1/2	+1/2	0	-
	μ	0.106	1/2	-1/2	-1	-
	$\nu_\tau^{(b)}$	0	1/2	+1/2	0	-
	τ	1.777	1/2	-1/2	-1	-
Gauge Bosons	γ	0	1	-	0	-
	W^\pm	80.22	1	-	± 1	-
	Z	91.187	1	-	0	-
	g	0	1	-	0	(c)
Higgs	H ^(b)	?	0	-	0	-

The gauge bosons mediate the interactions for the appropriate forces among the particles. The gluons (g) moderate the strong force between particles possessing a net color charge. Quarks (which come in the three colors; R(ed), G(reen), and B(lue)) have their strong reactions arbitrated by the gluons as described by the Feynman diagram in Figure 1.1(a). The gluons themselves also possess a net color charge (having eight colored combinations of R, G, and B) and are able to couple with one another via the three and four point interactions as illustrated in Figure 1.1(b,c). The photon (γ) mediates the electromagnetic force between particles possessing an electric charge. Unlike the gluons which are endowed with a net color charge which it couples to, the photon does not have an electric charge, itself, resulting in photons being unable to directly interact with one another. Hence, it only couples to the quarks, electrically charged leptons, and the W^\pm gauge bosons as illustrated in Figure 1.2. The W^\pm and Z bosons are the mediators of the weak force. These bosons couple primarily to the left-handed chirality of the fermions (quarks and leptons). The observed interactions involving the weak force suggest a symmetry that groups the left-handed helicity states of the quarks and leptons into three generations each. The grouping for the leptons are:

$$\begin{pmatrix} \nu_{e,L} \\ e_L^- \end{pmatrix} \quad \begin{pmatrix} \nu_{\mu,L} \\ \mu_L^- \end{pmatrix} \quad \begin{pmatrix} \nu_{\tau,L} \\ \tau_L^- \end{pmatrix} \quad (1.1)$$

while that of the quarks are:

$$\begin{pmatrix} u_L \\ d_L \end{pmatrix} \quad \begin{pmatrix} c_L \\ s_L \end{pmatrix} \quad \begin{pmatrix} t_L \\ b_L \end{pmatrix}. \quad (1.2)$$

A lepton couples weakly only with its corresponding partner within the generation (via the charged weak current) or with its antiparticle (via the neutral weak current). The neutral weak current involving quarks is similar to that of the leptons with respect to a quark only interacting with its antiparticle. However, the charged weak

current engaging quarks differs from that involving the leptons. Quarks are allowed to couple across generations as long as the interaction is with a quark of a different electric charge. The strengths of the couplings between particular quarks i and j are represented by the V_{ij} elements in the Cabibbo-Kobayashi-Maskawa (CKM) Matrix:³

$$\begin{pmatrix} V_{ud} & V_{us} & V_{ub} \\ V_{cd} & V_{cs} & V_{cb} \\ V_{td} & V_{ts} & V_{tb} \end{pmatrix} = \begin{pmatrix} 0.9747 \text{ to } 0.9759 & 0.218 \text{ to } 0.224 & 0.002 \text{ to } 0.005 \\ 0.218 \text{ to } 0.224 & 0.9738 \text{ to } 0.9752 & 0.032 \text{ to } 0.048 \\ 0.004 \text{ to } 0.015 & 0.030 \text{ to } 0.048 & 0.9988 \text{ to } 0.9995 \end{pmatrix} \quad (1.3)$$

Feynman diagrams illustrating the charged and neutral weak currents are shown in Figure 1.3.

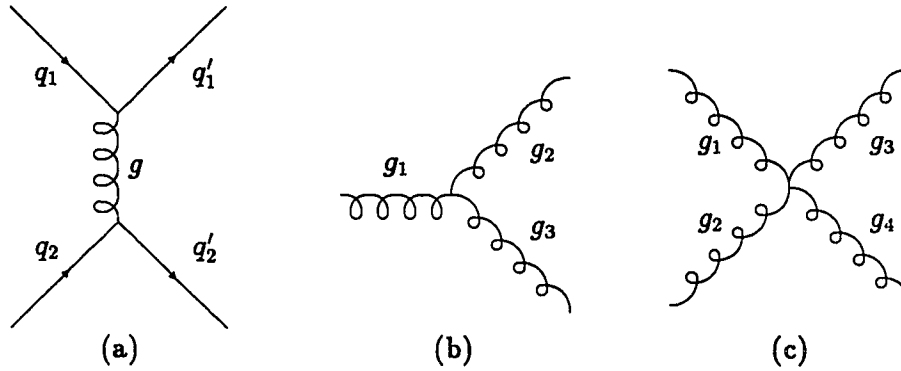


Figure 1.1: Feynman diagrams illustrating the strong force. The gluon mediates the interaction between two quarks in (a). Gluons also couple to themselves via the three and four-point interactions in (b) and (c), respectively.

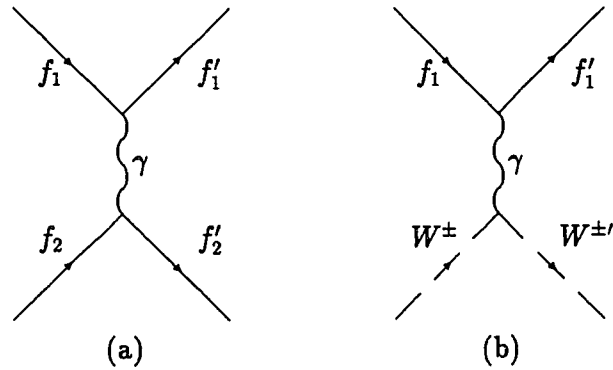


Figure 1.2: Feynman diagrams illustrating the electromagnetic force. The photon mediates the interaction between two charged fermions (quarks and leptons) f_1 and f_2 in (a) and between a fermion and a gauge boson in (b).

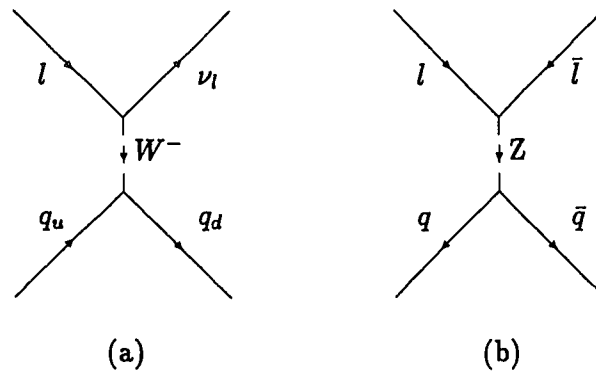


Figure 1.3: Feynman diagrams illustrating the weak force. The W^{\pm} gauge boson mediates the charged weak current in (a), while the Z gauge boson arbitrates the neutral weak current in (b). The l and ν_l is any lepton and its neutrino. The q_u is any one of (u,c,t) and q_d represents any of (d,s,b).

1.1.2 Symmetries in the Formulation of the Standard Model

The goal of Elementary Particle Physics is to explain, as much as possible, the phenomena observed in nature with a minimal amount of arbitrary input. Symmetries are used in the reduction for the number of the parameters needed. The Standard Model organizes the three forces (no gravitation) into an $SU_C(3) \times SU_L(2) \times U_Y(1)$ group symmetry. The $SU_C(3)$ group describes the strong interaction, while the $SU_L(2) \times U_Y(1)$ accommodates the unified electroweak force.

The relativistic wave equations (Dirac and Klein-Gordon) can be rewritten in the Lagrangian formalism. Imposing a local phase invariance on the free fermion (having no external influences) Lagrangian will necessitate the existence of the gauge bosons which counter any unphysical phase introduced by the generators of the above symmetry groups. In the electroweak case, the symmetry will need to be broken to allow for the observed *massive* W^\pm and Z bosons. It is convenient that the same broken symmetry also affords the leptons and quarks to similarly acquire nonzero masses.

The final symmetry to be discussed here (in passing only) is the relationship between the number of quark families to the number of lepton families that is born out of the renormalizability of the electroweak theory. For the electroweak theory to remain calculable, the number of quark families must be equal to that of leptons.

$SU_C(3)$ of the Strong Force

The strong force can be modeled by an $SU_C(3)$ symmetry where the R(ed), G(reen), and B(lue) color charges form the fundamental representation of the group.

(The set of unitary 3 X 3 matrices with $\det U = 1$ form the group $SU(3)$.) The color charges can be represented by:

$$R = \begin{pmatrix} 1 \\ 0 \\ 0 \end{pmatrix} \quad G = \begin{pmatrix} 0 \\ 1 \\ 0 \end{pmatrix} \quad B = \begin{pmatrix} 0 \\ 0 \\ 1 \end{pmatrix}.$$

There are eight generators in this group which can be represented by 3 X 3 matrices.

They are:

$$\begin{aligned} \lambda_1 &= \begin{pmatrix} 0 & 1 & 0 \\ 1 & 0 & 0 \\ 0 & 0 & 0 \end{pmatrix} & \lambda_2 &= \begin{pmatrix} 0 & -i & 0 \\ i & 0 & 0 \\ 0 & 0 & 0 \end{pmatrix} & \lambda_3 &= \begin{pmatrix} 1 & 0 & 0 \\ 0 & -1 & 0 \\ 0 & 0 & 0 \end{pmatrix} \\ \lambda_4 &= \begin{pmatrix} 0 & 0 & 1 \\ 0 & 0 & 0 \\ 1 & 0 & 0 \end{pmatrix} & \lambda_5 &= \begin{pmatrix} 0 & 0 & -i \\ 0 & 0 & 0 \\ i & 0 & 0 \end{pmatrix} & \lambda_6 &= \begin{pmatrix} 0 & 0 & 0 \\ 0 & 0 & 1 \\ 0 & 1 & 0 \end{pmatrix} \\ \lambda_7 &= \begin{pmatrix} 0 & 0 & 0 \\ 0 & 0 & -i \\ 0 & i & 0 \end{pmatrix} & \lambda_8 &= \sqrt{\frac{1}{3}} \begin{pmatrix} 0 & -i & 0 \\ i & 0 & 0 \\ 0 & 0 & 0 \end{pmatrix} \end{aligned} \quad (1.4)$$

where the following commutation relation holds among the generators:

$$\left[\frac{\lambda_i}{2}, \frac{\lambda_j}{2} \right] = i \sum_k f_{ijk} \frac{\lambda_k}{2} \quad (1.5)$$

and the nonzero terms for the completely antisymmetric f_{ijk} are permutations of

$$\begin{aligned} f_{123} &= 1, \quad f_{458} = f_{678} = \frac{\sqrt{3}}{2}, \\ f_{147} &= f_{165} = f_{246} = f_{257} = f_{345} = f_{376} = \frac{1}{2}. \end{aligned}$$

A feeling for the dynamics between the R,G,B eigenvectors and the λ matrices providing the transformations between the eigenvectors may be achieved by referencing Figure 1.4. The R,G,B base states are plotted in terms of their λ_3, λ_8 eigenvalues. The remaining six generators give analogues of the “step up” and “step down” operators of different $SU(2)$ subgroups of $SU(3)$.

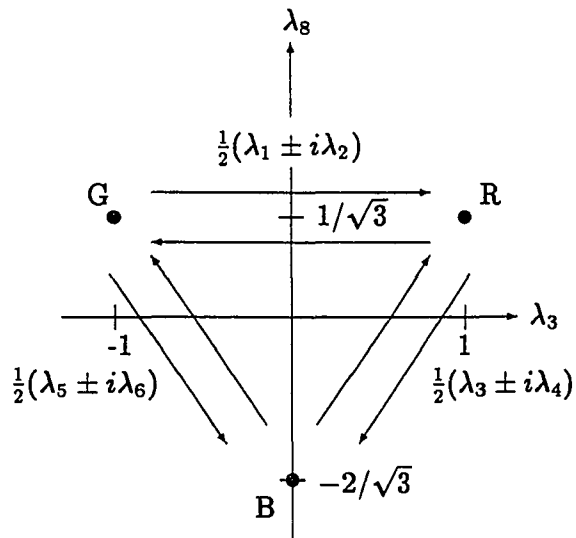


Figure 1.4: Dynamics of $SU_C(3)$ group.

Lagrangian of the Strong Force

The relativistic wave equations are rewritten in the Lagrangian formalism by constructing a Lagrangian \mathcal{L} such that when it is substituted into

$$\frac{\partial}{\partial x_\mu} \left(\frac{\partial \mathcal{L}}{\partial (\partial \phi / \partial x_\mu)} \right) - \frac{\partial \mathcal{L}}{\partial \phi} = 0, \quad (1.6)$$

the desired relativistic wave equation results. For example, inserting the lagrangian

$$\mathcal{L}_{Dirac} = -i(\partial^\mu \bar{\psi}) \gamma_\mu \psi - m \psi \bar{\psi} \quad (1.7)$$

into equation 1.6 will produce the Dirac equation:

$$(i\gamma^\mu \partial_\mu - m)\bar{\psi} = 0 \quad (1.8)$$

where $\phi = \bar{\psi}$ in (1.6) derives (1.8) from (1.7). The wavefunction ψ has four components to accommodate the two spin states of the fermion and antifermion. (See [4, chapter 5] for details, for example.)

The innate impossibility to observe a quantity is associated with the existence of a symmetry. For example, the absence of an absolute position in space follows from spatial translation invariance...it is only the relative positions that provide any physics. In a quantum mechanical description for the state of a system, the absolute phase is also immeasurable, while the relative phase differences render the physics. Hence, it is anticipated that a similar symmetry be expected of the phase. In general, the immeasurable phase may vary over space-time x , so it is natural to impose an invariance of the physics with respect to the phase $\alpha(x)$. This invariance is implemented by the requirement for the lagrangian of a fermion (to describe quarks; the carriers of the strong RGB charges) to be unchanged when the wavefunction ψ undergoes a local phase transformation

$$\psi(x) \rightarrow e^{i\alpha_a(x)T_a}\psi(x). \quad (1.9)$$

where $T_a = \frac{\lambda_a}{2}$ and λ_a are the eight generators of the color force in (1.4). As it stands, the present free fermion lagrangian, equation 1.7, is not invariant with the general phase transformation of (1.9). The algebraic procedures in constructing a phase (or gauge) invariant form of (1.7) starts by considering the infinitesimal phase transformations

$$\psi(x) \rightarrow [1 + i\alpha_a(x)T_a]\psi(x) \quad (1.10)$$

and

$$\partial_\mu\psi(x) \rightarrow [1 + i\alpha_a(x)T_a]\partial_\mu\psi(x) + iT_a\psi(x)\partial_\mu\alpha_a(x). \quad (1.11)$$

The last term in (1.11) destroys the invariance of \mathcal{L}_μ . It is desired to construct a covariant derivative \mathcal{D}_μ which transforms as (1.10), namely

$$\mathcal{D}_\mu\psi(x) \rightarrow [1 + i\alpha_a(x)T_a]\mathcal{D}_\mu\psi(x). \quad (1.12)$$

In the process of creating \mathcal{D}_μ ,

$$\mathcal{D}_\mu = \partial_\mu + ig_S T_a G_\mu^a, \quad (1.13)$$

eight gauge fields are introduced, each transforming as

$$G_\mu^a \rightarrow G_\mu^a - \frac{1}{g_S} \partial_\mu \alpha_a - f_{abc} \alpha_b G_\mu^c. \quad (1.14)$$

Adding a gauge invariant kinetic energy term for each of the G_μ^a fields (the association of this term with the kinetic energy is learned by experience with the lagrangian giving rise to the Klein–Gordon equation) results in the final QCD lagrangian:

$$\mathcal{L}_{\text{QCD}} = \bar{\psi}(i\gamma^\mu \mathcal{D}_\mu - m)\psi - \frac{1}{4} G_{\mu\nu}^a G_a^{\mu\nu} \quad (1.15)$$

or

$$\mathcal{L}_{\text{QCD}} = \bar{\psi}(i\gamma^\mu \partial_\mu - m)\psi - g_S (\bar{\psi} \gamma^\mu T_a \psi) G_\mu^a - \frac{1}{4} G_{\mu\nu}^a G_a^{\mu\nu} \quad (1.16)$$

with

$$G_{\mu\nu}^a = \partial_\mu G_\nu^a - \partial_\nu G_\mu^a - g_S f_{abc} G_\mu^b G_\nu^c. \quad (1.17)$$

The emphasis here is that imposing the “natural” local phase symmetry upon the $SU_C(3)$ group describing the strong interaction demands the introduction of the gauge fields, the gluons.

$SU_L(2) \times U_Y(1)$ of the Electroweak Force

The electroweak interaction is explained by a $SU_L(2) \times U_Y(1)$ symmetry. Each of the left-handed fermion doublets in Equations 1.1 and 1.2 form the bases of the $SU_L(2)$ group. The weak isospin currents are:

$$J_\mu^i = \bar{\chi}_L \gamma_\mu \frac{1}{2} \tau_i \chi_L, \text{ with } i = 1, 2, 3 \quad (1.18)$$

where χ_L are the 2x1 column matrices representing the doublets of Equations 1.1 and 1.2. (Each fermion in a doublet is represented by a Dirac spinor 4x1 matrix

consisting of information for the two spin states of the particle and its antiparticle as well.) The τ_i are the Pauli spin matrices:

$$\tau_1 = \begin{pmatrix} 0 & 1 \\ 1 & 0 \end{pmatrix} \quad \tau_2 = \begin{pmatrix} 0 & -i \\ i & 0 \end{pmatrix} \quad \tau_3 = \begin{pmatrix} 1 & 0 \\ 0 & -1 \end{pmatrix}. \quad (1.19)$$

The motivation for this $SU_L(2)$ symmetry is provided by the “step up” and “step down” operators $\tau_{\pm} = \frac{1}{2}(\tau_1 \pm \tau_2)$:

$$\tau_+ = \begin{pmatrix} 0 & 1 \\ 0 & 0 \end{pmatrix} \quad \tau_- = \begin{pmatrix} 0 & 0 \\ 1 & 0 \end{pmatrix} \quad (1.20)$$

which model the charge changing (CC) weak currents. For example, the CC weak currents for the first lepton family in (1.1) are described by:

$$J_{\mu}^{+} = \bar{\chi}_L \gamma_{\mu} \tau_+ \chi_L = \bar{\nu}_{e,L} \gamma_{\mu} e_L \quad (1.21)$$

and

$$J_{\mu}^{-} = \bar{\chi}_L \gamma_{\mu} \tau_- \chi_L = \bar{e}_L \gamma_{\mu} \nu_{e,L} \quad (1.22)$$

which are pictured in Figure 1.5.

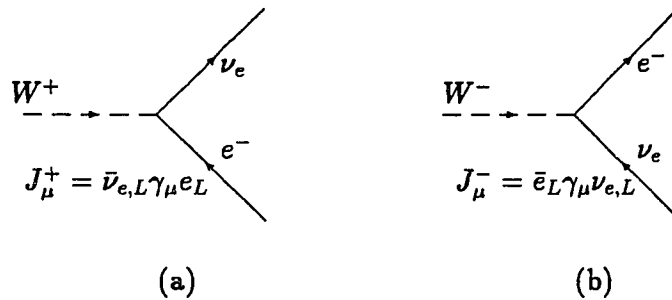


Figure 1.5: Feynman diagrams illustrating the charge changing weak current. Charge raising current, J_{μ}^{+} , in (a) and lowering current, J_{μ}^{-} , in (b).

The dynamics of the $SU_L(2)$ group are depicted in Figure 1.6 where the fermion base states f_{upper} ($u, c, t, \nu_e, \nu_\mu, \nu_\tau$) and f_{lower} ($d, s, b, e^-, \mu^-, \tau^-$) are shown in terms of their J_μ^3 eigenstates.

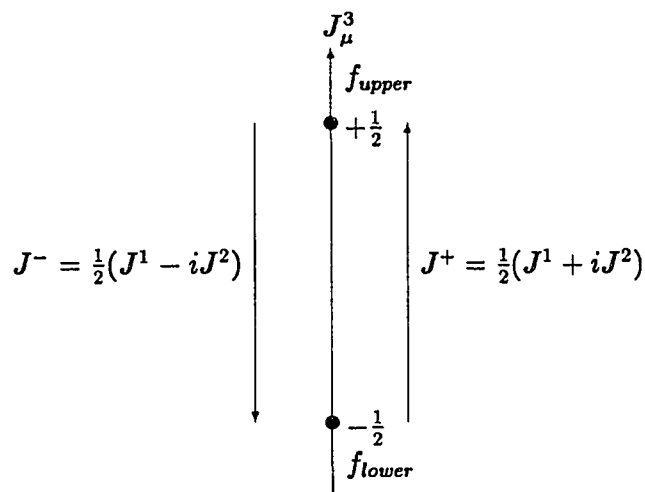


Figure 1.6: Dynamics of $SU_L(2)$ group.

Integrating (1.18) over all space with $\mu = 0$,

$$T^i = \int J_0^i(x) d^3x = \int [\chi^\dagger \frac{1}{2} \tau_i \chi_L] d^3x \quad (1.23)$$

gives the corresponding charges that satisfy the commutation rule:

$$[T^i, T^j] = i\epsilon_{ijk} T^k. \quad (1.24)$$

T^3 is called the weak isospin. The weak isospin values in Table 1.1 can easily be verified by recognizing the doublets in (1.1) and (1.2) as χ_L in (1.23) and using τ_3 of (1.19). (The measured T^3 value for the b quark provides the most convincing evidence that the top quark should have existed even before its direct observation. This point will be reiterated in the section, "Motivation For Existence of the Top Quark.")

Association of J_μ^3 with the electrically neutral electromagnetic current is not possible since the photon couples to right handed chiralities whereas the J_μ^3 , by definition, can only accommodate left-handed currents. Thus, another current (which also includes a right-handed component) is introduced which will mix with the electrically neutral left-handed J_μ^3 and result in the observed currents of the photon and Z boson. (The mixing comes about “naturally” in the Higgs Symmetry Breaking mechanism as the W^\pm and Z bosons acquire their nonzero masses). The inclusion of a new neutral current Y (and no new charged current) means that the group has to be enlarged by a $U_Y(1)$ factor to $SU_L(2) \times U_Y(1)$ and is given by

$$j_\mu^Y = \bar{\varphi} \gamma_\mu Y \varphi \quad (1.25)$$

where φ is either a left-handed or right-handed chiral field. The weak hypercharge Y transforms as $U_Y(1)$ and is defined by

$$Q = T^3 + \frac{Y}{2} \quad (1.26)$$

where Q is the electric charge of the fermion involved in the neutral current process.

Lagrangian of the Electroweak Force Before Symmetry Breaking

Just as the gauge bosons of the strong force were necessarily generated to preserve the local phase symmetry of the lagrangian under the $SU_C(3)$ transformations, the “primordial” (before symmetry breaking) gauge bosons of the electroweak force will also be inescapably created to ensure the local phase symmetry of $SU_L(2) \times U_Y(1)$. The phase invariance is required for each of the two groups, independently. So, the lagrangian is demanded to be unchanged by the introduction of any phase by either group on the wavefunctions for both helicity states:

$$\chi_L \rightarrow e^{i\alpha_a(x)T^a + i\beta(x)Y} \chi_L \quad (1.27)$$

and

$$\psi_R \rightarrow e^{i\beta(x)Y} \psi_R \quad (1.28)$$

where the summation over “a” runs over the three weak isospin charges given by (1.23). Except for a massive $m\bar{\chi}_L\chi_L$ term which destroys phase invariance, similar arguments that led to the lagrangian in (1.16) for QCD result in a phase invariant lagrangian accommodating the electroweak $SU_L(2)\times U_Y(1)$ symmetry:

$$\begin{aligned} \mathcal{L}_{EW}^{primal} = & \bar{\chi}_L\gamma^\mu(i\partial_\mu - g\frac{1}{2}\boldsymbol{\tau} \cdot \mathbf{W}_\mu - g'\frac{Y}{2}B_\mu)\chi_L + \bar{\psi}_R\gamma^\mu(i\partial - g'\frac{Y}{2}B_\mu)\psi_R \\ & - \frac{1}{4}\mathbf{W}_{\mu\nu} \cdot \mathbf{W}^{\mu\nu} - \frac{1}{4}B_{\mu\nu}B^{\mu\nu} \end{aligned} \quad (1.29)$$

where \mathbf{W}_μ represents three $W_\mu^{a=1,2,3}$ bosons that transform (similarly as the gluons do in (1.14)) as:

$$\mathbf{W}_\mu \rightarrow \mathbf{W}_\mu - \frac{1}{g}\partial_\mu\boldsymbol{\alpha} - \boldsymbol{\alpha}X\mathbf{W}_\mu. \quad (1.30)$$

The kinetic energy is described by the $\mathbf{W}_{\mu\nu}$ and $B_{\mu\nu}$ terms which are:

$$\mathbf{W}_{\mu\nu} = \partial_\mu\mathbf{W}_\nu - \partial_\nu\mathbf{W}_\mu - g\mathbf{W}_\mu X\mathbf{W}_\nu \quad (1.31)$$

and

$$B_{\mu\nu} = \partial_\mu B_\nu - \partial_\nu B_\mu. \quad (1.32)$$

The $\boldsymbol{\tau} \cdot \mathbf{W}_\mu$ is a shorthand notation for the summation $\tau_a W_\mu^a$ with “a” running over (1,2,3). The g and g' are strength coupling constants within the $SU_L(2)$ and $U_Y(1)$ groups which are parameters of the theory that have to be measured.

While the $W_\mu^1, W_\mu^2, W_\mu^3$, and B_μ gauge bosons are necessarily created to maintain the phase symmetry, the lagrangian in (1.29) is unable to explain the observed *massive* electroweak gauge bosons mediating the interaction between *massive* fermions. The lagrangian in (1.29) requires fermions and the four gauge bosons to be massless. The manner in which the W^\pm and Z bosons acquire a nonzero mass description is discussed next.

Electroweak Symmetry Breaking Affording Massive W,Z Bosons

The W^\pm and Z bosons obtain nonzero mass values through what is called the Higgs mechanism. Before an explanation of the phenomenon begins, it is instructive to illustrate the basic associations for the terms involved in the lagrangian that give the Klein-Gordon equation. For an electrically *neutral* particle, the field in the lagrangian,

$$\mathcal{L}_{KG}^{\text{real}} = \frac{1}{2}(\partial_\mu\phi)(\partial^\mu\phi) - \frac{1}{2}m^2\phi^2, \quad (1.33)$$

is a *real* scalar. Substituting Equation 1.33 into Equation 1.6 gives

$$\partial_\mu\partial^\mu\phi + m^2\phi^2 \equiv (\square + m^2)\phi = 0. \quad (1.34)$$

For an electrically *charged* particle, the field in the lagrangian,

$$\mathcal{L}_{KG}^{\text{complex}} = (\partial_\mu\Phi)^*(\partial^\mu\Phi) - m^2\Phi^*\Phi, \quad (1.35)$$

is a *complex* scalar where $\Phi = \frac{1}{\sqrt{2}}(\phi_1 + i\phi_2)$ for real fields ϕ_i . Regarding Φ and Φ^* as independent fields, substitution of Equation 1.35 in Equation 1.6 results in

$$(\square + m^2)\Phi = 0 \quad \text{and} \quad (\square + m^2)\Phi^* = 0. \quad (1.36)$$

The normalization of the complex lagrangian is such that

$$\mathcal{L}_{KG}^{\text{complex}}(\Phi) = \mathcal{L}_{KG}^{\text{real}}(\phi_1) + \mathcal{L}_{KG}^{\text{real}}(\phi_2). \quad (1.37)$$

For either neutral or charged cases, the term proportional to $(\partial_\mu\phi)(\partial^\mu\phi)$ is associated with the kinetic energy. This correspondence had been used previously as $G_{\mu\nu}^a$ in (1.17) was affiliated with the kinetic energy in (1.16) for QCD, while $\mathbf{W}_{\mu\nu}$ and $B_{\mu\nu}$ in (1.31) and (1.32) were connected with the kinetic energies in (1.29) for electroweak. The other association here is that for the mass term:

$$\text{Lagrangian mass term for } \textit{neutral} \text{ particles: } \frac{1}{2}m^2\phi^2 \quad (1.38)$$

and

$$\text{Lagrangian mass term for } \textit{charged} \text{ particles: } m^2\Phi^*\Phi. \quad (1.39)$$

The Higgs mechanism for the Minimal Standard Model introduces four real scalar fields ϕ_i which are arranged in an isospin doublet with weak hypercharge $Y = 1$:

$$\phi = \begin{pmatrix} \phi^+ \\ \phi^0 \end{pmatrix} = \begin{pmatrix} \frac{1}{\sqrt{2}}(\phi_1 + i\phi_2) \\ \frac{1}{\sqrt{2}}(\phi_3 + i\phi_4) \end{pmatrix}. \quad (1.40)$$

These fields are introduced into the electroweak theory by incorporating them in an $SU_L(2) \times U_Y(1)$ invariant lagrangian. An association in the lagrangian for nonzero mass terms for the W^\pm and Z bosons will ultimately be made. The appropriate description for the W^\pm, Z fields is the Klein-Gordon equation. Noting the modified differential term in (1.29), a Klein-Gordon-like lagrangian which can be added to $\mathcal{L}_{EW}^{\text{primordial}}$ is:

$$\mathcal{L}_{EW}^{\text{Higgs}} = | (i\partial_\mu - g\frac{1}{2}\boldsymbol{\tau} \cdot \mathbf{W}_\mu - g'\frac{Y}{2}B_\mu)\phi |^2 - V(\phi) \quad (1.41)$$

with

$$V(\phi) = \mu^2\phi^\dagger\phi + \lambda(\phi^\dagger\phi)^2. \quad (1.42)$$

If $\mu^2, \lambda > 0$, $\mathcal{L}_{EW}^{\text{primordial}} + \mathcal{L}_{EW}^{\text{Higgs}}$ describes a system of four scalar particles, each of mass μ , interacting with the *massless* gauge bosons W_μ^a and B_μ . Instead, the interesting case is for $\mu^2 < 0$ and $\lambda > 0$. The potential $V(\phi)$ of (1.42) then has its minimum at:

$$\phi^\dagger\phi \equiv \frac{1}{2}(\phi_1^2 + \phi_2^2 + \phi_3^2 + \phi_4^2) = -\frac{\mu^2}{2\lambda}. \quad (1.43)$$

The critical step is to exploit the local $SU_L(2) \times U_Y(1)$ symmetry and reparameterize ϕ in (1.40) around a particular choice for the minimum in (1.43) such that three of

the scalar ϕ_i 's in (1.40) can be associated with a phase transformation. The precise choice for the minimum is:

$$\phi_1 = \phi_2 = \phi_4 = 0, \quad \phi_3^2 = -\frac{\mu^2}{\lambda} \equiv v^2 \quad (1.44)$$

which breaks the $SU_L(2)$ invariance for the distribution of solutions given by (1.43) and casts the minimum in the form:

$$\phi_0 = \sqrt{\frac{1}{2}} \begin{pmatrix} 0 \\ v \end{pmatrix} \quad (1.45)$$

which is also referred to as the vacuum expectation value. Fluctuations away from the minimum, ϕ_0 , can be reparameterized in terms of $(\theta_1(x), \theta_2(x), \theta_3(x), h(x))$ instead of $(\phi_1(x), \phi_2(x), \phi_3(x), \phi_4(x))$ in (1.40) with:

$$\phi(x) = e^{i\boldsymbol{\tau} \cdot \boldsymbol{\theta}(x)/v} \begin{pmatrix} 0 \\ \sqrt{\frac{1}{2}}[v + h(x)] \end{pmatrix}. \quad (1.46)$$

Performing the matrix multiplication in (1.46) for small deviations about the minimum:

$$\phi(x) \simeq \sqrt{\frac{1}{2}} \begin{pmatrix} 1 + i\theta_3/v & i(\theta_1 - i\theta_2)/v \\ i(\theta_1 + i\theta_2)/v & 1 - i\theta_3/v \end{pmatrix} \begin{pmatrix} 0 \\ v + h(x) \end{pmatrix} \quad (1.47)$$

$$\simeq \sqrt{\frac{1}{2}} \begin{pmatrix} \theta_2 + i\theta_1 \\ v + h(x) - i\theta_3 \end{pmatrix} \quad (1.48)$$

demonstrates that $(\theta_1(x), \theta_2(x), \theta_3(x), h(x))$ do fully parameterize excursions away from ϕ_0 . From equation (1.46), $(\theta_1, \theta_2, \theta_3)$ are understood to be equivalent to phases of an $SU(2)$ phase transformation. (This can be seen by comparing (1.46) to (1.27) with T^i given by (1.23).) Thus, by the phase symmetry argument, $(\theta_1, \theta_2, \theta_3)$ must be unobservable. Only $h(x)$, the Higgs scalar particle, remains after the reparameterization. Its nonzero mass of $m_h = \sqrt{2v^2\lambda}$ can be realized with the mass term association from (1.38) applied to \mathcal{L}_{EW}^{Higgs} given by (1.41) and (1.42) with μ related to the minimum potential via (1.44).

The gauge boson masses will be identified by substituting the vacuum expectation value, ϕ_0 , into the \mathcal{L}_{EW}^{Higgs} of (1.41) and using the mass term associations given by (1.38) or (1.39). The relevant term in (1.41) is:

$$\begin{aligned} & |(-ig\frac{\boldsymbol{\tau}}{2}\cdot\mathbf{W}_\mu - ig'\frac{B_\mu}{2})\phi|^2 \\ &= \frac{1}{8} \left| \begin{pmatrix} gW_\mu^3 + g'B_\mu & g(W_\mu^1 - iW_\mu^2) \\ g(W_\mu^1 + iW_\mu^2) & -gW_\mu^3 + g'B_\mu \end{pmatrix} \begin{pmatrix} 0 \\ v \end{pmatrix} \right| \end{aligned} \quad (1.49)$$

$$= \frac{1}{8}v^2g^2[(W_\mu^1)^2 + (W_\mu^2)^2] + \frac{1}{8}v^2(g'B_\mu - gW_\mu^3)(g'B_\mu - gW_\mu^3) \quad (1.50)$$

$$= (\frac{1}{2}vg)^2W_\mu^+W_\mu^- + \frac{1}{8}v^2(W_\mu^3, B_\mu) \begin{pmatrix} g^2 & -gg' \\ -gg' & (g')^2 \end{pmatrix} \begin{pmatrix} W_\mu^3 \\ B_\mu \end{pmatrix} \quad (1.51)$$

where $W^\pm = \sqrt{\frac{1}{2}}(W^1 \mp iW^2)$. Comparing the first term in (1.51) to an expected mass term from (1.39), it is seen that the W gauge boson mass is:

$$M_W^\pm = \frac{1}{2}vg. \quad (1.52)$$

The remaining mass term is not diagonal in the W_μ^3, B_μ basis. The physical fields for the photon, A_μ , and Z_μ are obtained by diagonalizing the 2x2 matrix in (1.51). The two eigenvalues are $\lambda_1 = 0$ and $\lambda_2 = g^2 + (g')^2$. Since the eigenvalues will ultimately be associated with the mass values of the photon and Z boson through (1.38), the eigenvector for $\lambda_1 = 0$ will be assigned to that for the photon (A_μ) while the other is to account for the Z boson (Z_μ),

$$A_\mu = \frac{g'W_\mu^3 + gB_\mu}{\sqrt{g^2 + (g')^2}} \quad \text{with } \lambda_1 = 0 \quad (1.53)$$

$$Z_\mu = \frac{gW_\mu^3 - g'B_\mu}{\sqrt{g^2 + (g')^2}} \quad \text{with } \lambda_2 = g^2 + (g')^2. \quad (1.54)$$

Inserting the Z_μ eigenvector from (1.54) into the second term of (1.50) and comparing with the expected form of (1.38) gives the mass of the Z boson:

$$M_Z = \frac{1}{2}v\sqrt{g^2 + (g')^2}. \quad (1.55)$$

Defining the relative coupling strength of g for $SU_L(2)$ to g' for $U_Y(1)$ via

$$\frac{g'}{g} = \tan \theta_W \quad (1.56)$$

gives a familiar recasting of (1.53) and (1.54):

$$A_\mu = \cos \theta_W B_\mu + \sin \theta_W W_\mu^3 \quad (1.57)$$

$$Z_\mu = -\sin \theta_W B_\mu + \cos \theta_W W_\mu^3. \quad (1.58)$$

where θ_W is called the Weinberg or weak mixing angle.

The three degrees of freedom associated with (ϕ_1, ϕ_2, ϕ_4) that seem to have disappeared through the phase invariance of (1.46) is seen to reappear as three required longitudinal helicity states for the now massive W^\pm and Z gauge bosons. The only meaning to their sacrificial existence is to accommodate a phase transformation which breaks the $SU(2)$ symmetry in the family of solutions for the minimal potential and afford the W^\pm and Z bosons to become massive via the additional longitudinal degree of freedom for their helicity.

Electroweak Symmetry Breaking Affording Massive Fermions

The lagrangian $\mathcal{L}_{EW}^{primordial}$ describes massless fermions. A fortunate feature of the Standard Model is that the same symmetry breaking mechanism which generates masses for the W and Z bosons also renders masses for the leptons and quarks.

For the leptons, an $SU_L(2) \times U_Y(1)$ gauge invariant lagrangian term is added to the previous electroweak lagrangian parts, $\mathcal{L}_{EW}^{primordial}$ and \mathcal{L}_{EW}^{Higgs} :

$$\mathcal{L}_{EW}^{lepton\ masses} = -G_l \left[(\bar{\nu}_l, \bar{l})_L \begin{pmatrix} \phi^+ \\ \phi^0 \end{pmatrix} l_R + \bar{l}_R (\phi^-, \bar{\phi}^0) \begin{pmatrix} \nu_l \\ l \end{pmatrix}_L \right]. \quad (1.59)$$

for each lepton doublet. Substituting the SU(2) symmetry breaking vacuum expectation value of (1.46),

$$\phi = \sqrt{\frac{1}{2}} \begin{pmatrix} 0 \\ v + h(x) \end{pmatrix} \quad (1.60)$$

into (1.59) results in:

$$\mathcal{L}_{EW}^{lepton\ masses} = -\frac{G_l}{\sqrt{2}} v (\bar{l}_L l_R + \bar{l}_R l_L) - \frac{G_l}{\sqrt{2}} h (\bar{l}_L l_R + \bar{l}_R l_L). \quad (1.61)$$

Noting the relation:

$$m_l \bar{l} l = m_l \bar{l} \left[\frac{1}{2}(1 - \gamma^5) + \frac{1}{2}(1 + \gamma^5) \right] l \quad (1.62)$$

$$= m_l (\bar{l}_R l_L + \bar{l}_L l_R), \quad (1.63)$$

equation (1.61) becomes:

$$\mathcal{L}_{EW}^{lepton\ masses} = -\frac{G_l}{\sqrt{2}} v \bar{l} l - \frac{G_l}{\sqrt{2}} h \bar{l} l. \quad (1.64)$$

Recognizing the form of the mass term in \mathcal{L}_{Dirac} from (1.7) which is the appropriate lagrangian for fermions, G_l can be related to the mass m_l for a lepton:

$$m_l = \frac{G_l v}{\sqrt{2}}, \quad (1.65)$$

so that (1.64) reduces to:

$$\mathcal{L}_{EW}^{lepton\ masses} = -m_l \bar{l} l - \frac{m_l}{v} \bar{l} l h. \quad (1.66)$$

The first term is the sought-after mass term for the lepton where m_l (derived from G_l) is an arbitrary parameter of the theory which must be measured. The second term is the coupling of the lepton to the Higgs scalar which has its coupling strength proportional to the m_l . Since $v = 246$ GeV, this coupling is small for light leptons.

The quark masses are generated in a similar way. The only modification is for the creation of masses for the upper members in the quark doublets. A charge conjugate version of ϕ in (1.40) is needed such that the SU(2) transformations of ϕ_c are identical to those of ϕ . The construction of ϕ_c is:

$$\phi_c = -i\tau_2\phi^* = \begin{pmatrix} -\bar{\phi}^0 \\ \phi^- \end{pmatrix}, \quad (1.67)$$

which expanding about the symmetry breaking vacuum expectation value gives:

$$\phi_c = \sqrt{\frac{1}{2}} \begin{pmatrix} v + h \\ 0 \end{pmatrix}. \quad (1.68)$$

The additional SU_L(2)×U_Y(1) invariant lagrangian term for generating quark masses is:

$$\begin{aligned} \mathcal{L}_{EW}^{quark\ masses} = & -G_d \left[(\bar{u}, \bar{d})_L \begin{pmatrix} \phi^+ \\ \phi^0 \end{pmatrix} d_R + \bar{d}_R(\phi^-, \bar{\phi}^0) \begin{pmatrix} u \\ d \end{pmatrix}_L \right] \\ & -G_u \left[(\bar{u}, \bar{d})_L \begin{pmatrix} -\bar{\phi}^0 \\ \phi^- \end{pmatrix} u_R + \bar{u}_R(-\phi^0, \phi^+) \begin{pmatrix} u \\ d \end{pmatrix}_L \right] \end{aligned} \quad (1.69)$$

for each quark doublet where u and d represent the upper and lower quarks in any doublet. Expanding about the vacuum expectation value gives:

$$\mathcal{L}_{EW}^{quark\ masses} = -m_d \bar{d}d(1 + \frac{h}{v}) - m_u \bar{u}u(1 + \frac{h}{v}) \quad (1.70)$$

which has a similar form as its leptonic counterpart in (1.66).

Summarizing the electroweak lagrangian, \mathcal{L}_{EW} is made of four parts:

$$\mathcal{L}_{EW} = \mathcal{L}_{EW}^{primordial} + \mathcal{L}_{EW}^{Higgs} + \mathcal{L}_{EW}^{lepton\ masses} + \mathcal{L}_{EW}^{quark\ masses}. \quad (1.71)$$

Gathering the results from (1.29), (1.41), (1.59), and (1.69) provides the final result:

$$\mathcal{L}_{EW} = \bar{\chi}_L \gamma^\mu (i\partial_\mu - g\frac{1}{2}\boldsymbol{\tau} \cdot \mathbf{W}_\mu - g'\frac{Y}{2}B_\mu) \chi_L + \bar{\psi}_R \gamma^\mu (i\partial_\mu - g'\frac{Y}{2}B_\mu) \psi_R$$

$$\begin{aligned}
& -\frac{1}{4}\mathbf{W}_{\mu\nu} \cdot \mathbf{W}^{\mu\nu} - \frac{1}{4}B_{\mu\nu}B^{\mu\nu} \\
& + |(i\partial_\mu - g\frac{1}{2}\boldsymbol{\tau} \cdot \mathbf{W}_\mu - g'\frac{Y}{2}B_\mu)|^2 - V(\phi) \\
& + \sum_{\text{lepton doublets}} -G_l \left[(\bar{\nu}_l, \bar{l})_L \begin{pmatrix} \phi^+ \\ \phi^0 \end{pmatrix} l_R + \bar{l}_R(\phi^-, \bar{\phi}^0) \begin{pmatrix} \nu_l \\ l \end{pmatrix}_L \right] \\
& + \sum_{\text{quark doublets}} \left\{ -G_d \left[(\bar{u}, \bar{d})_L \begin{pmatrix} \phi^+ \\ \phi^0 \end{pmatrix} d_R + \bar{d}_R(\phi^-, \bar{\phi}^0) \begin{pmatrix} u \\ d \end{pmatrix}_L \right] \right. \\
& \quad \left. -G_u \left[(\bar{u}, \bar{d})_L \begin{pmatrix} -\bar{\phi}^0 \\ \phi^- \end{pmatrix} u_R + \bar{u}_R(-\phi^0, \phi^+) \begin{pmatrix} u \\ d \end{pmatrix}_L \right] \right\} \quad (1.72)
\end{aligned}$$

where the potential, $V(\phi)$, is given by (1.42).

Symmetric Ramification From Renormalizability of the Electroweak Theory

In the Standard Model, there are anomalies in the calculations which are potential sources for non-renormalizability. Such an example occurs in the computation of a fermion loop coupled to two vector currents and one axial current as shown in Figure 1.7(a) which comes about from a physical interaction as in Figure 1.7(b). The anomaly is proportional to

$$\sum_{\text{fermion doublets}} Y \quad (1.73)$$

of the $U_Y(1)$ group. Recalling (1.26) transforms (1.73) in terms of the electric charges:

$$\sum_{\text{fermion doublets}} Q = \sum_{\text{lepton doublets}} Q + \sum_{\text{quark doublets}} Q = 0. \quad (1.74)$$

For an arbitrary number of lepton and quark generations, $N_{\text{gen}}^{\text{lepton}}$ and $N_{\text{gen}}^{\text{quark}}$, this reduces to:

$$N_{\text{gen}}^{\text{lepton}}(0 - 1) + 3N_{\text{gen}}^{\text{quark}}\left(\frac{2}{3} - \frac{1}{3}\right) = 0 \quad (1.75)$$

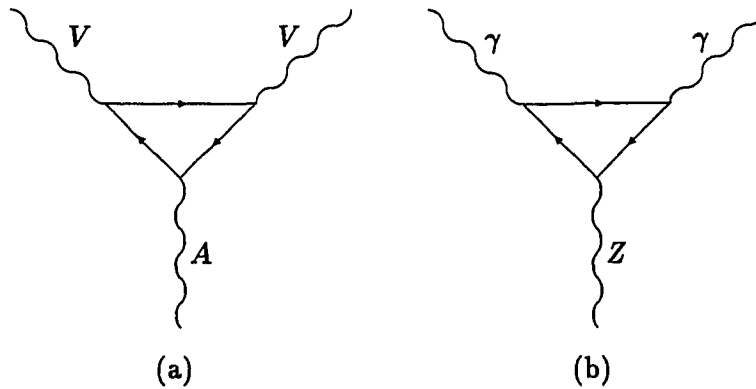


Figure 1.7: Example of an anomaly in the Standard Model. Fermion loop connecting two vector currents and one axial current in (a). A physical process giving rise to the anomaly of (a) is shown in (b).

where the factor of 3 accommodates the R,G,B color charges that are available to the quarks. Equation (1.75) states that the anomalies cancel if $N_{gen}^{lepton} = N_{gen}^{quark}$. Hence, the Standard Model remains calculable provided there is symmetry between the number of lepton and quark generations. (This symmetry will be one of the arguments to reason that the top quark must exist.)

1.2 Motivation For Existence of the Top Quark

Even in the absence for the direct observation of the top quark,^{1,2} there are several compelling arguments to reason that it should exist. Besides providing a natural solution for the Standard Model to remain calculable, a direct measurement for the *consistency* of the left-handed b quark belonging to a doublet is possible. Furthermore, another measurement is capable of testing the *inconsistency* of the left-handed b quark being ascribed to a singlet. Finally, the last remaining topless model is examined; this model is capable of producing the b quark $SU_L(2)$ dou-

plet *consistency* and singlet *inconsistency* experimental results, but fails in another aspect.

1.2.1 Renormalizability of the Electroweak Theory

As mentioned earlier, calculations of anomalies as shown in Figure 1.7 within the electroweak theory are potential sources of divergences. The problem is most easily and naturally (but not necessarily) averted by a symmetry between the number of generations for leptons and quarks. This symmetry requires the existence of top.

1.2.2 Test of B Quark Being an $SU_L(2)$ Doublet

The consistency of the left-handed b quark belonging to an $SU_L(2)$ doublet can be tested by a measurement of the b's weak isospin, T_3^b . This is afforded in $e^+e^- \rightarrow b\bar{b}$ processes where the b quarks are produced via a $\gamma - Z$ interference which gives rise to an asymmetric forward-backward distribution of the b quarks with respect to the e^+e^- beamline. The two interfering subprocesses are illustrated in Figure 1.8.

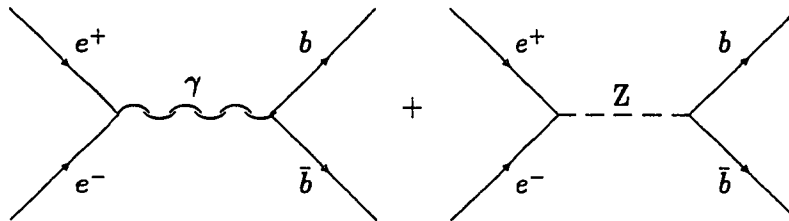


Figure 1.8: Interference of $\gamma - Z$ in $e^+e^- \rightarrow b\bar{b}$.

The coupling of the b quark to the Z boson is proportional to $(T_{3L}^b + \frac{1}{3} \sin^2 \theta_w)$ which takes on the value of $+0.07$ if $T_{3L}^b = 0$ (top quark *does not* exist) or -0.43 if $T_{3L}^b = \frac{1}{2}$ (top quark *does* exist). Experimentally, results from A_{FB} and $\Gamma(Z)$ give⁵ $T_{3L}^b = -0.504^{+0.018}_{-0.011}$ and $T_{3R}^b = -0.008 \pm 0.056$. Thus, when viewed in this model dependent perspective, the left-handed b quark is very much consistent with being the lower member of a weak isospin doublet. Its partner is, by definition, the top quark!

1.2.3 Test of B Quark Being an $SU_L(2)$ Singlet

If the top quark did not exist and *both* helicity states of the b were to be singlets, the only way for the b quark to decay would be by some kind of mixing of the b with the d and s quarks, of which a decay of the s via the usual (virtual) W,Z bosons occur. The W and Z decays of the s quark from these processes are shown in Figure 1.9. Independent of the particular mixing between the b and s quarks, a

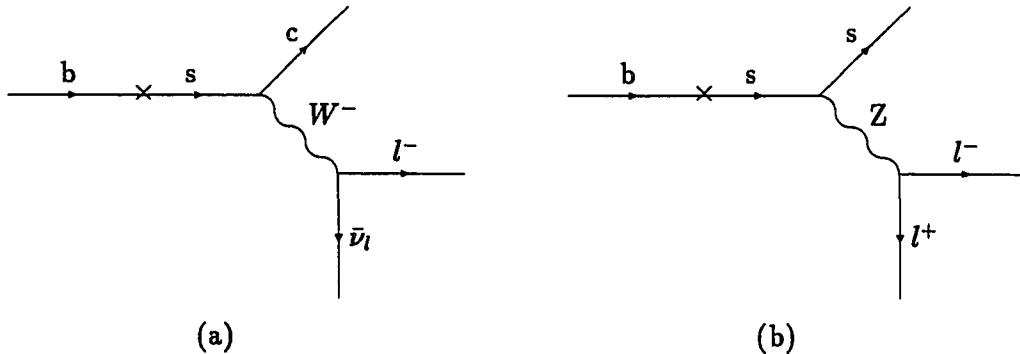


Figure 1.9: Hypothetical b-quark decay for left-handed b singlets. The s quark decays via a W in (a) and through a Z in (b).

relation for the ratio of the s decays via the W to that of the Z is:⁶

$$\frac{\Gamma(b \rightarrow s \rightarrow s + l^- + l^+)}{\Gamma(b \rightarrow s \rightarrow c + l^- + \bar{\nu})_l} \geq 0.12. \quad (1.76)$$

The experimental evidence^{7,8} provides an upper limit $\sim 3 - 4$ orders of magnitude below this lower limit. Thus, the data provides disagreement for *both* helicity states of the b quark to be described by singlets.

1.2.4 Examination of the Last Surviving Topless Model

The last surviving topless model⁹ was proposed by Ma.¹⁰ It is able to produce the observed phenomena that argue the existence of top through the $SU_L(2)$ symmetry assertions above, as well as the measured $B_d^0 - \bar{B}_d^0$ mixing which hasn't been discussed.

This model has two u-type quarks and four d-type quarks. The low-energy interactions in this model are described by an $SU_C(3) \times SU_1(2) \times SU_2(2) \times U_H(1)$ symmetry. For the left-handed helicity states, (u_L, d_L) and (c_L, s_L) transform as $SU_1(2)$ doublets, while b_L does so as a singlet. In the case of the right-handed helicity states, (u_R, d_R) and (c_R, b_R) are ascribed to $SU_2(2)$ doublets, while s_R is a singlet. (Note that the s and b quarks have swapped roles in the left-handed and right-handed groupings. Also, notice that one of the b helicity states is part of a doublet (in $SU_2(2)$), a different situation from that depicted in the $SU_L(2)$ singlet test above where *both* helicity states were singlets.)

The Ma model predicts very different partial width values for $Z \rightarrow \tau^+ \tau^-$ and $Z \rightarrow b \bar{b}$. Differences in the above predictions result in altered expectations for hadronic and total widths as well. Comparisons¹¹ of these widths of the Z boson as

calculated by the Standard Model and the Ma model to that measured experimentally are gathered in Table 1.2. The data clearly rules out this last surviving topless model and argues for the existence of the top quark!

Table 1.2: The partial and total widths of the Z as predicted by the Standard Model and the Ma Model¹⁰ and their comparison¹¹ to the measured values. A * denotes an assumption of three neutrino generations in its calculation.

	Standard Model (MeV)	Ma Model ¹⁰ (MeV)	Experimental Measurement ³ (MeV)
$\Gamma(Z \rightarrow \tau^+ \tau^-)$	83.4	96.7	83.7 ± 0.4
$\Gamma(Z \rightarrow b \bar{b})$	381	24.2	384.7 ± 5.3
$\Gamma(Z \rightarrow \text{hadrons})$	1735	1378	1741 ± 4
$\Gamma(Z)$	2482*	2139*	2490 ± 7

1.3 Standard Model Constraint on M_{top}

Not only is the Standard Model able to argue the existence of the top quark before any direct observation, it is also capable of constraining its mass value, should it indeed exist. A global fit¹² to 15 measured parameters of the Standard Model results in:

$$m_{top}^{SM} = 178_{-11}^{+11} {}_{-19}^{+18} \text{ GeV}/c^2 \quad (1.77)$$

where the first set of errors is calculated assuming the mass of the Higgs to be $300 \text{ GeV}/c^2$. The second set of errors corresponds to the variation of the central value when the Higgs mass is modified over the interval $60 \leq m_H(\text{GeV}/c^2) \leq 1000$. This global fit incorporated data from DØ,¹³ CDF,¹³ UA2,¹⁴ CDHS,¹⁵ CHARM,¹⁶ CCFR,¹⁷ SLD,¹⁸ and the experiments at LEP.¹² The same m_{top} dependence on m_H via the second set of errors in Equation 1.77 will provide constraint information in the search for the Higgs once m_{top} is known. Figure 1.10 shows the interplay

between m_H and m_{top} within the one standard deviation range of m_W . For a review of the current status of the top quark, see [23].

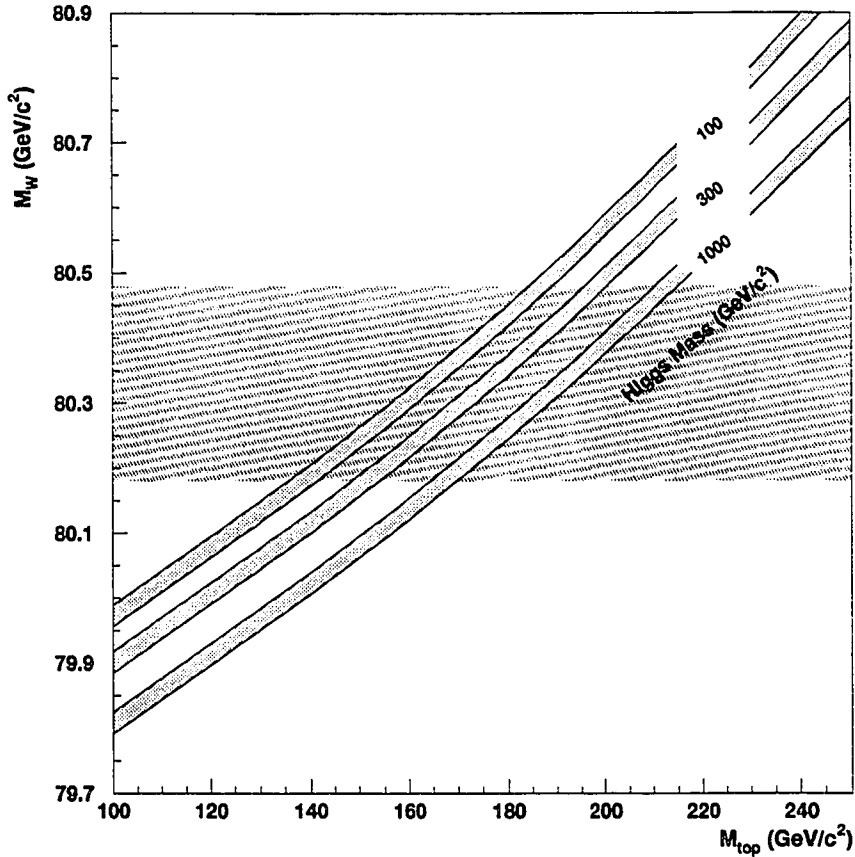


Figure 1.10: The Standard Model relation between m_{top} , m_W , and m_H .¹⁹⁻²¹ The striped band represents the most current world average W mass of $80.33 \pm 0.15 \text{ GeV}/c^2$.²²

1.4 Is Top the Last Quark?

The answer to this question lies in a precision measurement of the Z boson lineshape for the contributions of neutrinos from the different generations and noting

the symmetry between the number of generations for quarks and essentially massless neutrinos. The LEP average²⁴ is:

$$N_\nu = 2.991 \pm 0.016. \quad (1.78)$$

Thus, renormalizability of the electroweak theory in the Standard Model requires the number of quark families also be three, making top the final quark.

1.5 Production and Decay of the Top Quark

The top quark is predominantly produced in pairs (t and \bar{t}) because of its heavy mass²⁵ which is well above the upper threshold of $\sim m_W - m_b$ where single top production is prevalent via $W \rightarrow t + b$. The dominant contributions for the production of $t\bar{t}$ are through the $q\bar{q} \rightarrow t\bar{t}$ and $gg \rightarrow t\bar{t}$ processes illustrated in Figure 1.11. For the 900 GeV colliding p and \bar{p} beams present at the Tevatron, the prevailing production mechanism is through $q\bar{q}$ annihilation since quarks are more abundant than gluons at higher x (proton momentum fraction) values. A next to leading order (NLO) calculation²⁶ for the proportion of $t\bar{t}$ production due to $q\bar{q} \rightarrow t\bar{t}$ and $gg \rightarrow t\bar{t}$, as shown in figure 1.12, demonstrates the increasing fraction of $q\bar{q} \rightarrow t\bar{t}$ for heavier top. The total production cross section for top quarks using an order α_s^3 calculation and a resummation of the leading soft gluon corrections in all orders of perturbation theory²⁷ is shown in Figure 1.13. This top mass dependent cross section is what will be used in this analysis.

After the t and \bar{t} quarks are produced, each will decay weakly before hadronizing if $m_t \gtrsim 150$ GeV.²⁸ The expected weak decays of the t 's are driven by the ratios of $|V_{tb}|^2:|V_{ts}|^2:|V_{td}|^2$ in the CKM matrix given in (1.3). (The elements in the third row of the CKM matrix (V_{tb}, V_{ts}, V_{td}) are determined by unitary constraints.) Thus,

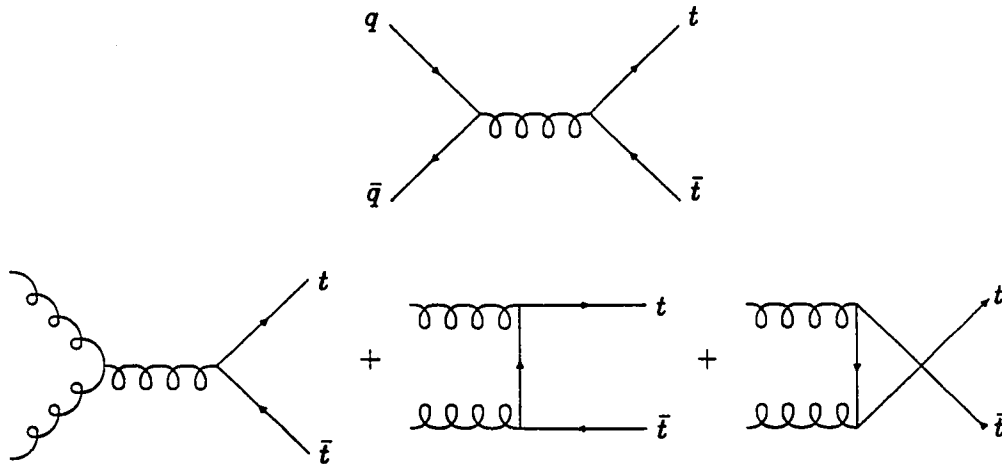


Figure 1.11: Lowest order $t\bar{t}$ production processes.

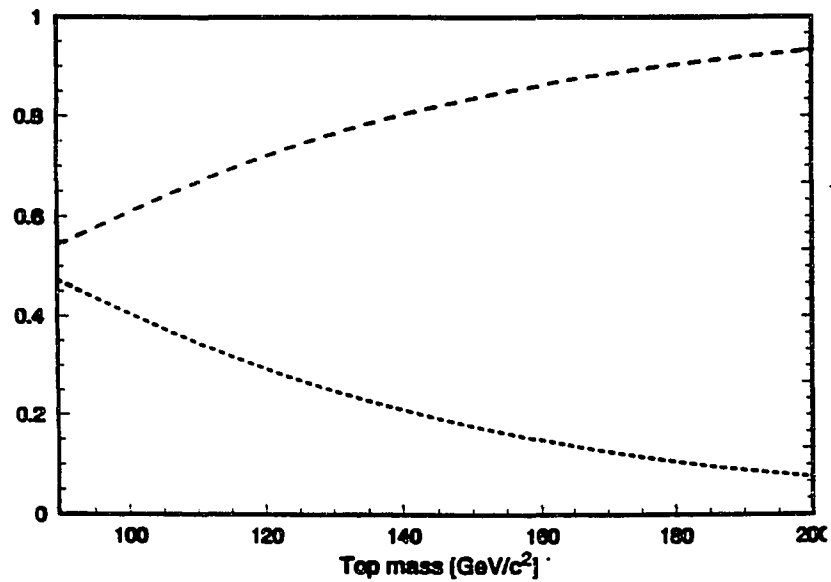


Figure 1.12: Next to leading order calculation for fractional contributions of $q\bar{q} \rightarrow t\bar{t}$ (upper) and $gg \rightarrow t\bar{t}$ (lower) processes in $t\bar{t}$ production.²⁶

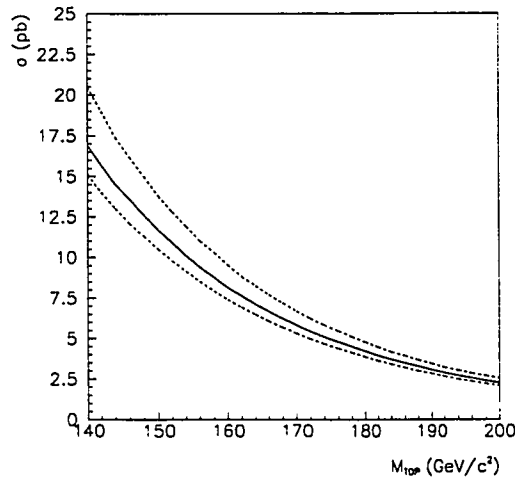


Figure 1.13: Theoretical $t\bar{t}$ production cross section.²⁷ Best estimate is given by the solid line while estimates for upper and lower deviations are shown in dashed.

the anticipated decay of the top quarks are $t \rightarrow W^+ + b$ and $\bar{t} \rightarrow W^- + \bar{b}$. The b and \bar{b} quarks typically produce one jet of secondary particles each. The *massive* real W bosons, however, decay into two well separated fermions. The allowed pairs of fermions the W bosons decay into and their relative frequency among each other are gathered in Table 1.3. For example, the real W^- boson is able to decay into any of the three lepton-antineutrino pairs ($e-\bar{\nu}_e, \mu-\bar{\nu}_\mu, \tau-\bar{\nu}_\tau$) or six quark-antiquark pairs ($\bar{u}-d, \bar{c}-s$), noting that each of the quark-antiquark pairs are available in the three R,G,B color charges. Approximately, each of the nine final states of the W^- decays are equally probable. If the W^- decay is to a quark-antiquark pair, each parton will hadronize into a jet, resulting in two well separated jets. The real W^+ boson decays similarly. Summing the individual decay modes that give rise to the $t\bar{t} \rightarrow \mu + \text{jets}$ signal, the total branching fraction of all $t\bar{t}$ decays that is used in this analysis to

infer the presence of top is: $\frac{12}{81} \simeq 14.8\%$. Figure 1.14 illustrates the production and generalized decay of the $t\bar{t}$ system.

Table 1.3: Summary of probability for various decay modes for the $t\bar{t}$ system.
A * denotes the decay modes sensitive to this analysis.

$W^+ \quad W^- \rightarrow$	$e^-, \bar{\nu}_e$ (1/9)	$\mu^-, \bar{\nu}_\mu$ (1/9)	$\tau^-, \bar{\nu}_\tau$ (1/9)	\bar{u}, d (3/9)	\bar{c}, s (3/9)
e^+, ν_e (1/9)	1/81	1/81	1/81	3/81	3/81
μ^+, ν_μ (1/9)	1/81	1/81	1/81	3/81*	3/81*
τ^+, ν_τ (1/9)	1/81	1/81	1/81	3/81	3/81
u, \bar{d} (3/9)	3/81	3/81*	3/81	9/81	9/81
c, \bar{s} (3/9)	3/81	3/81*	3/81	9/81	9/81

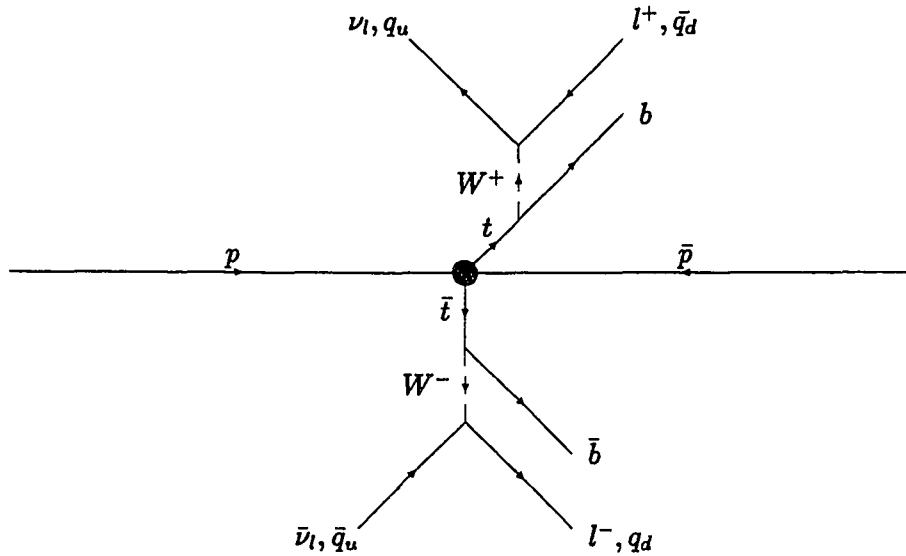


Figure 1.14: Topology of $t\bar{t}$ production and decay. The production details in the solid circle include diagrams like those in figure 1.11. The l and ν_l represent any lepton and its neutrino, while q_u (q_d) are any upper (lower) member of the quark weak isospin doublets.

Chapter 2

The Apparatus

The experimental apparatus that affords the search for the top quark consists of the accelerator (providing the potential production of $t\bar{t}$ events through colliding beams of p and \bar{p}) and the $D\emptyset$ detector (allowing the observation for the decay of $t\bar{t}$). A simple overview of both very complex systems will follow. More information on the accelerator can be found in [29] and the references contained therein. The discussion on the $D\emptyset$ detector below is a brief summary of an exhaustive description compiled in [30].

2.1 The Accelerator

The proton and antiproton beams which collide in the $D\emptyset$ detector are the final result of seven accelerators, the final being the familiar Tevatron. An overview of the Fermilab accelerator complex is shown in Figure 2.1. The process begins with the preaccelerator which creates H^- ions and accelerates them to 750 keV with a Cockcroft–Walton generator. These 750 keV H^- ions are bunched and become the input to the LINAC (a 146 m long linear accelerator) which further increases the energy to 400 MeV. The 400 MeV H^- ions emerging from the LINAC enter the Booster which is a synchrotron with a radius of 75.5 m. (A synchrotron accelerates charged particles in an orbit of fixed radius by continually adjusting the strengths of the bending magnet fields as the particles increase their energy.) Upon entry

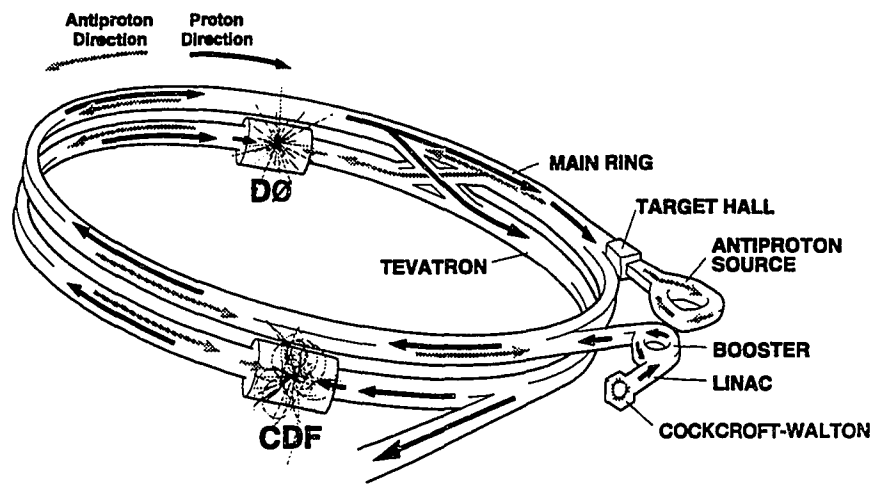


Figure 2.1: An overview of the Fermilab accelerator complex with the DØ and CDF detectors.

into the Booster, the electrons are stripped from the H^- by passing the negatively charged ions through a carbon foil, resulting in a bare H^+ atom, or proton p . The Booster then accelerates the protons from 400 MeV to 8 GeV and delivers them to the Main Ring which is another synchrotron, but with a radius of 1 km! The Main Ring is multipurpose. One of its functions is to boost the 8 GeV protons to 120 GeV which are used in the production of antiprotons. This is accomplished by directing the 120 GeV protons onto an antiproton target, a nickel disk, and capturing 8 GeV negatively charged particles (mostly antiprotons) and directing them to the Debuncher. The Debuncher's purpose is to sharpen the momentum resolution of the antiprotons from $\frac{\delta p}{p} = 4\%$ to $\frac{\delta p}{p} = 0.2\%$ by measuring their deviations in the transverse plane away from the ideal path and sending a corrective signal across the ring which causes a compensating kick to be applied to the particles. The corrections are very small to prevent the noise of the interplay between charged particles from

dominating the corrective signal. This portion of the acceleration cycle is the most time consuming, taking up ≈ 2 of the 2.4 seconds for the entire antiproton cycle. After the momentum resolution is tightened, the antiprotons are injected into the accumulator for storage. The accumulator stores the antiprotons by saving them in a smaller orbit than that when they originally entered. The extraction procedure from the accumulator to the Main Ring is reversed.

The transfer and boosting of protons from the Booster to the Tevatron as well as of the antiprotons from the accumulator to the Tevatron are accomplished through the Main Ring. Fifteen bunches of 8 GeV protons are injected from the Booster into the Main Ring which is then ramped to 150 GeV in ≈ 1.2 seconds. The 15 bunches are then coalesced into one bunch through the addition of lower frequency electromagnetic waves that sum to a linear propagating field over the desired bunches to be brought together. The 8 GeV antiprotons from the accumulator are similarly boosted and coalesced, but with only 11 bunches, since losses in the merging are more costly for the precious antiprotons. This coalescing of the the proton and antiproton bunches result in bunch sizes typically of $\approx 150 \times 10^9$ and $\approx 50 \times 10^9$ for protons and antiprotons, respectively. Six of these large proton bunches are injected individually from the Main Ring into the Tevatron and followed by six antiproton bunches. The Tevatron then ramps the bunches from the input 150 GeV to the current operating energy of 900 GeV. Regions of collisions are controlled by special superconducting quadrupoles (known as low-beta quadrupoles) located on either side of the two interaction regions (at D0 and B0) that squeeze the beam into a spot size of $\sigma_{x,y} \approx 40 \mu\text{m}$, where x, y are transverse to the beam direction. Meanwhile, locations *away* from the luminous regions minimize unwanted interactions between p and \bar{p} with the use of electrostatic separators. A *store* where the $6p \times 6\bar{p}$ collisions

take place in the Tevatron typically lasts about 12 to 20 hours. After this time, the protons and antiprotons are dumped, and the Tevatron is refilled with a new set of six proton bunches and six antiproton bunches. Some of the major parameters of the Tevatron are summarized in Table 2.1.³¹

During a store of $6p \times 6\bar{p}$ collisions in the Tevatron, the other six accelerators function together to continually produce and stockpile antiprotons that will be used in future Tevatron stores.

Table 2.1: Tevatron Parameters.³¹

Accelerator radius	1000 m
Maximum Beam Energy	900 GeV
Peak Instantaneous Luminosity	$\simeq 10 \times 10^{30} \text{ cm}^{-2}\text{s}^{-1}$
Bunch Configuration	$6p \times 6\bar{p}$
Bunch Intensities	$\approx 100 \times 10^9(p), \approx 50 \times 10^9(\bar{p})$
Bunch Length	50 cm
Transverse Beam Radius	43 μm
RF Frequency (# of RF Buckets)	53 MHz (1113)
\bar{p} Stacking Rate	$\approx 3.5 \times 10^{10}/\text{hour}$
Time Between $p\bar{p}$ Interactions	3.5 μs

2.2 The Coordinate System at DØ

The explanation of the various components of the DØ Detector will be facilitated with the use of the coordinate system that is used to describe the momenta and energies of the particles that are detected. The right-handed coordinate system used at DØ has its z -axis defined to be in the direction of the incident proton in the Tevatron (south, defined in Fermilab's geography) and the y -axis upward. This fixes the x -axis to be in Fermilab's east direction. Conventional cylindrical (ρ, ϕ, z) and spherical (r, ϕ, θ) coordinates are used where the z -axis is taken to be the

polar axis. Instead of θ , it is more meaningful to describe the direction of a particle relative to the beam direction in terms of:

$$\eta = -\ln\left[\tan\left(\frac{\theta}{2}\right)\right] \quad (2.1)$$

which is an approximation to the true rapidity,

$$y = \frac{1}{2} \ln\left[\frac{E + p_z}{E - p_z}\right], \quad (2.2)$$

in the limit of $m \ll E$. The rapidity, y , is useful in an environment where the longitudinal momenta of the parent particles are unknown since a Lorentz boost β along the z -axis transforms $y \rightarrow y + \tanh^{-1} \beta$, resulting in an invariant distribution for dN/dy , where N is the multiplicity of daughter particles decayed from the boosted parent. The $p\bar{p}$ collisions provided by the Tevatron is such a situation because of the unknown longitudinal momenta of the quarks and gluons in the proton and antiproton that initiate the interactions. It is for this same reason that the transverse projection of momenta and energies,

$$p_T = p \sin \theta \quad (2.3)$$

and

$$E_T = E \sin \theta, \quad (2.4)$$

of the various particles are often used, since these quantities are also invariant with respect to any boost in the beam direction.

2.3 The DØ Detector

The DØ detector is a multipurpose detector for studying high p_T interactions resulting from $p\bar{p}$ collisions at the Tevatron. The design of the detector was driven

by the observation that new physics typically involve appreciable states with leptons, jets, neutrinos, and perhaps some new nondetectible particles (the Lightest Supersymmetric Particle in SUSY, for example). Therefore, the three physics goals were:

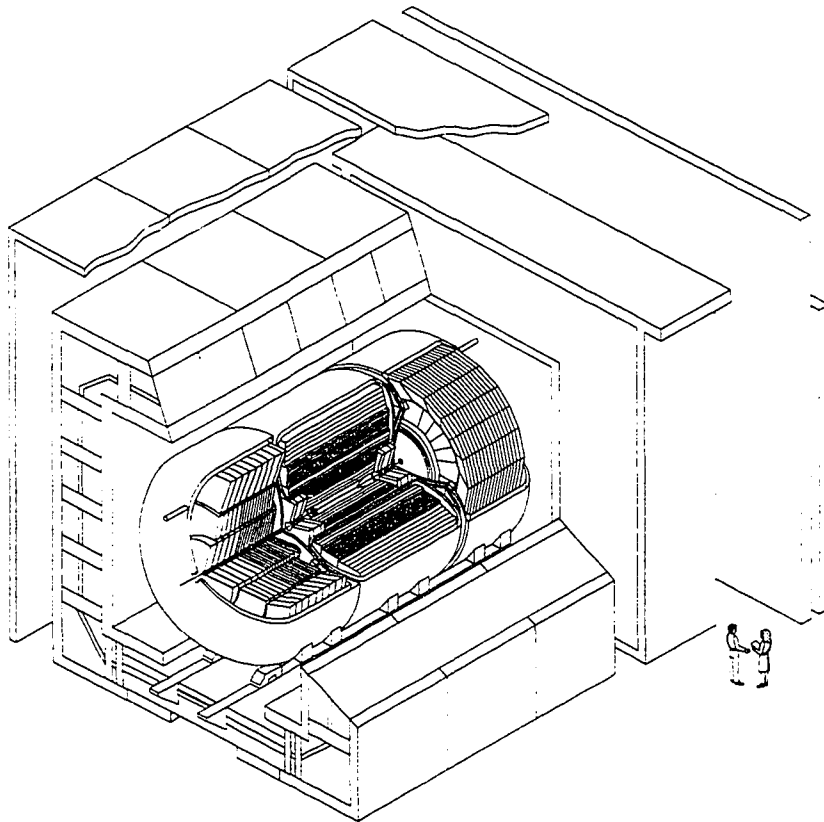
1. Excellent identification and measurement of the more accessible leptons, the electron and the muon.
2. Good measurement of parton jets at large p_T through finely segmented calorimetry with good energy resolution. (The focus on *parton* jets is more relevant to the underlying physics processes than an emphasis on the individual final particles emitted after hadronization.)
3. Excellent measurement of the missing transverse energy (\cancel{E}_T) as a means of inferring the presence of neutrinos and other non-interacting particles.

The resulting detector design that met the above physics goals emerged with the following features at its central portion:

- Compact nonmagnetic tracking system with an emphasis on discriminating multiple closely spaced tracks from a single track (to aid in rejecting fakes to electrons).
- Muon detection with thick magnetized iron absorbers to provide sufficient momentum measurement and to minimize backgrounds from punchthrough of hadrons.
- Hermetic and finely segmented calorimeter to provide a good measurement of \cancel{E}_T and to allow jet and electron identification with profiles of the energy depositions.

The overall layout of the DØ detector, as shown in Figure 2.2, begins with a set of tracking detectors, the Central Detectors (CD), around the beampipe. The CD

consists of the Vertex Chamber (VTX), the Transition Radiation Detector (TRD), the Central Drift Chamber (CDC), and the two Forward Drift Chambers (FDC). Encompassing the Central Detectors are the calorimeters. The Central Calorimeter (CC) surrounds the Central Drift Chamber (CDC), while the two End Calorimeters (EC) encase the Forward Drift Chambers (FDC) in the forward regions. The outermost detector is the muon system consisting of the Wide Angle MUon System (WAMUS) and the Small Angle MUon System (SAMUS). The WAMUS encompasses all three calorimeters while the SAMUS resides only in the most forward regions outside the End Calorimeters.



DØ Detector

Figure 2.2: An overall view of the DØ detector.

The general strategy of the $D\emptyset$ detector in identifying various particles and measuring their energy or momenta are:

1. For Electrons:

- Identification by a *single* track match in the CD to a cluster of energy in the calorimeters with a deposition profile consistent with that of an electron.
- Energy measurement by the amount of deposition in calorimeter.

2. For Muons:

- Identification by matching tracks in the CD to those in the muon system.
- Momentum measurement by the bend of the track in the magnet in the muon system.

3. For Neutrinos:

- Identification by a large missing transverse energy (\cancel{E}_T).
- Measurement by the amount of transverse energy imbalance over the CC and both ECs.

4. For *Partonic* Jets (collimated jetstream of particles which are the decay products of a parton):

- Identification by a deposition of energy in nearby cells in the calorimeter consistent with that expected of jets.
- Energy measurement by the amount of deposition in calorimeter.

Although this analysis used the Central Drift Chamber (CDC), the Central and End Calorimeters (CC and EC), and the Wide Angle MUon System (WAMUS), descriptions of the remaining four subdetectors (VTX, TRD, FDC, and SAMUS) are also included for completeness.

2.3.1 Central Detectors

The Central Detectors (CD) are comprised of the five subdetectors: the Vertex Chamber (VTX), the Transition Radiation Detector (TRD), the Central Drift Chamber (CDC), and the two Forward Drift Chambers (FDC). These are arranged together as shown in Figure 2.3 and occupy a cylindrical volume bounded by $\rho = 78$ cm and $z = \pm 135$ cm. As described above in the identification and measurement of the various particles, the primary function of the CD is to resolve *single* tracks for the identification of leptons. So, the emphasis is on the need to distinguish events with two closely spaced charged tracks from those with one. This is accomplished with the inherent design for the spatial resolution of the drift wires and also by an ionization energy measurement. Furthermore, the TRD is included to increase the rejection of a charged pion faking an electron.

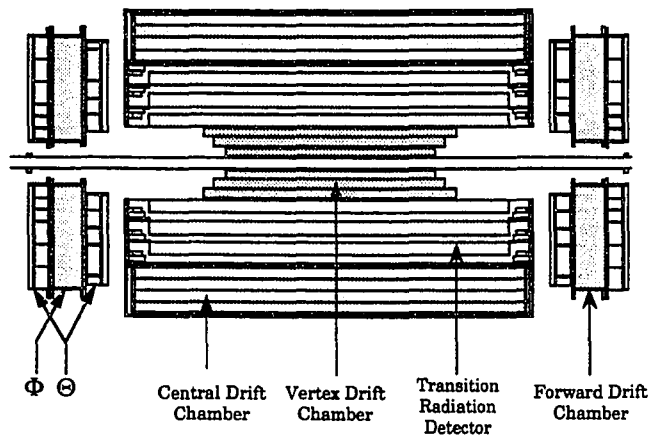


Figure 2.3: Schematic of the Central Detectors.

Vertex Detector

The VTX is the innermost CD subdetector. It wraps around the beryllium $p\bar{p}$ beam pipe from radii 3.7 cm to 16.2 cm and extends along the direction of the beam for an active region of $\sim \pm 50$ cm. An endview of a quadrant is shown in Figure 2.4. The VTX consists of three concentric chambers with 16 cells in the azimuthal direction for the innermost layer and 32 cells for the outer two layers, where the borders of the cells are the cathode wires. The sense wires run parallel to the beam direction. The grounded grid wires, the outer cathode field wires, the fine field wires, and the coarse aluminum traces all aid in providing a uniform field in the region away from the gas amplification region; the amplification region being around the sense wires and bordered by the grid wires. The sense wires are staggered by $\pm 100 \mu\text{m}$ to resolve the left-right ambiguities in track reconstruction. These wires also have a resistivity of $1.8 \text{ k}\Omega/\text{m}$ that provides a measurement of the coordinate parallel to the beam (z) through charge division. The position resolutions in the ρ - ϕ and z directions as measured in a test beam setup are $\approx 60 \mu\text{m}$ and $\approx 1 \text{ cm}$, respectively. Some of the interesting parameters are gathered in Table 2.2.

Transition Radiation Detector

The purpose of the Transition Radiation Detector is to identify electrons. This is accomplished by exploiting the phenomenon that lighter charged particles traversing media of differing dielectric constants will more readily radiate photons as compared to heavier charged particles. The relativistic γ factor necessary for detection of such an effect is ~ 1000 . Thus, an electron with mass 0.511 MeV will give a measurable

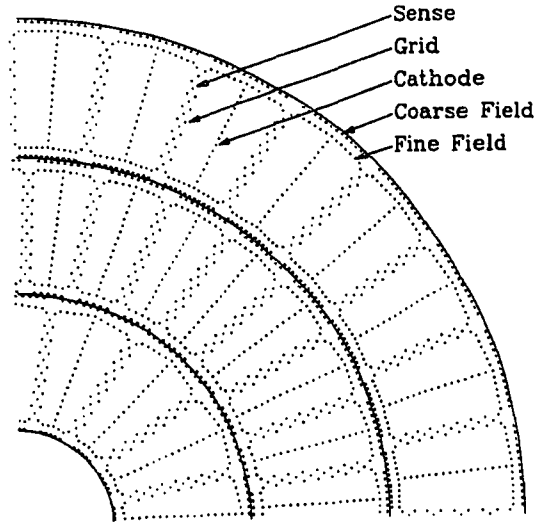


Figure 2.4: Endview of a quadrant of the VTX.

Table 2.2: VTX detector parameters.^{30,32}

Overall Active Radii	3.7 cm – 16.2 cm
Number of Concentric Layers	3
Active Lengths per Layer	96.6 cm, 106.6 cm, 116.6 cm
Number of Cells	16 inner layer, 32 outer two
Number of Sense Wires	8 per cell; 640 total
Sense Wire Separation	4.57 mm radially with 100 μm stagger
Wire Specifications	Sense Wires: 25 μm NiCoTin; 80 g tension Field Wires: 152 μm Au plated Al; 360 g tension
Sense Wire Voltage	+2.5 kV
Gas	CO ₂ 95%; Ethane 5%; H ₂ O 0.5%
Average Drift Field	1 kV/cm
Average Drift Velocity	$\approx 7.3 \mu\text{m}/\text{nsec}$
Maximum Drift Distance	1.6 cm
Position Resolution	$\rho\text{-}\phi$: $\approx 60 \mu\text{m}$ z : $\approx 1 \text{ cm}$

signal when its energy surpasses $\sim 0.511 \text{ GeV}$. A charged pion, on the other hand, has a mass of 140 MeV and will not provide detectable radiation below $\sim 140 \text{ GeV}$!

The TRD is just outside the VTX and inside the CDC. It consists of three concentric layers, each having a radiator, a conversion region, and an amplification/detection region. Figure 2.5 shows an azimuthal slice of an endview of the conversion and amplification/detection regions. The radiator provides the media of differing dielectric constants that radiate the photons off the electrons traversing it. The radiator is made of 393 layers of 18 μm thick polypropylene foil with a mean separation of 150 μm which is filled with nitrogen. A pair of 23 μm milar windows are used to separate the nitrogen gas of the radiator from the Xe(91%)/CH₄(7%)/C₂H₆(2%) mixture used in the conversion and amplification/detection regions. The transition radiation entering the conversion region is typically 8 keV and knocks electrons out from the gas molecules. These electrons drift across the 15 mm conversion region and are collected in the 8 mm amplification/detection portion. In addition to the electrons from transition radiation, there are also electrons from the ionization from the original charged particle traversing the TRD. So, a π^\pm would typically deposit electrons onto the anode by ionizing the gas, whereas an electron would give these and the additional electrons from the transition radiation. By simply totaling the energy deposited on the anode wires from the three layers, the TRD achieves a factor of ten rejection against π^\pm while keeping 90% of isolated electrons.

Central Drift Chamber

The CDC is the outermost CD subdetector, surrounding the TRD with dimensions $49.5 \text{ cm} \leq \rho \leq 74.5 \text{ cm}$ and $|z| \leq 92 \text{ cm}$. An endview of an azimuthal slice of the CDC is shown in Figure 2.6. It consists of four concentric layers with 32 azimuthal cells per layer. Adjacent layers are rotated in ϕ by half a cell. In each

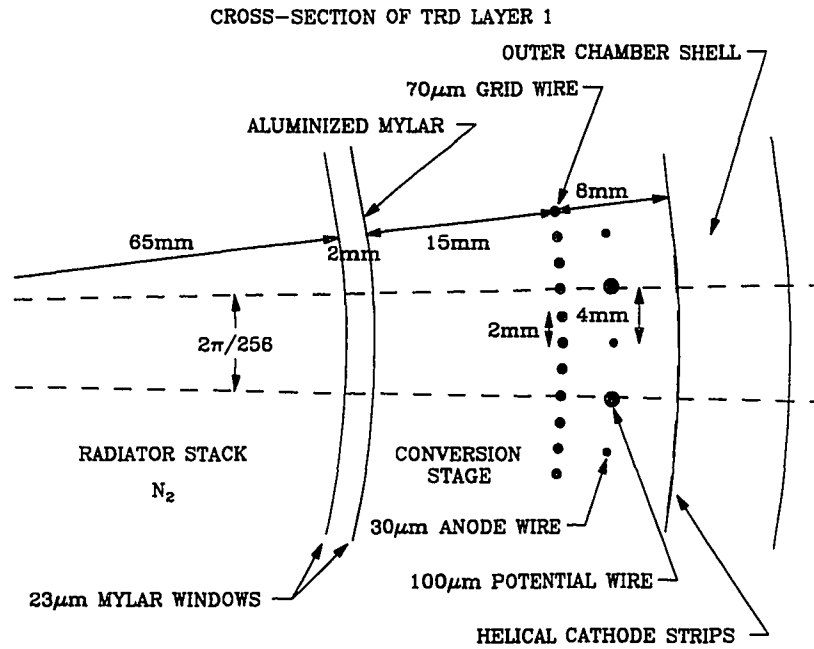


Figure 2.5: Endview of an azimuthal slice of the TRD's conversion and detection regions for one layer.

cell are seven sense wires to measure the ρ - ϕ coordinates. Adjacent sense wires are staggered by $\pm 200 \mu\text{m}$ to resolve left-right ambiguities in the track reconstruction. Also, in each cell are two delay lines, embedded in the inner and outer plates of the cells, to determine the z coordinate via a measurement of the difference in arrival times on both ends. These delay lines are coil windings around a carbon fiber epoxy core with a charge propagation velocity $\approx 2.35 \text{ mm/ns}$. The position resolutions in the ρ - ϕ and z directions as measured in the test beam setup are $150 \sim 200 \mu\text{m}$ and $\simeq 2 \text{ mm}$, respectively.

As mentioned earlier, one of the primary functions for the CD subdetectors is to resolve hits created by one track from those produced by two tracks, primarily for electron identification. The CDC uses the amount of energy deposited on its

wires as a way of discriminating between the two cases. Figure 2.7 illustrates the rejection power with an ionization signal defined to be the sum of the smallest 70% of the hits on the track; this procedure reduces the effect from delta-rays. The two track events were made by an offline overlay of single track events.

Some of the interesting parameters for the CDC are gathered in Table 2.3.

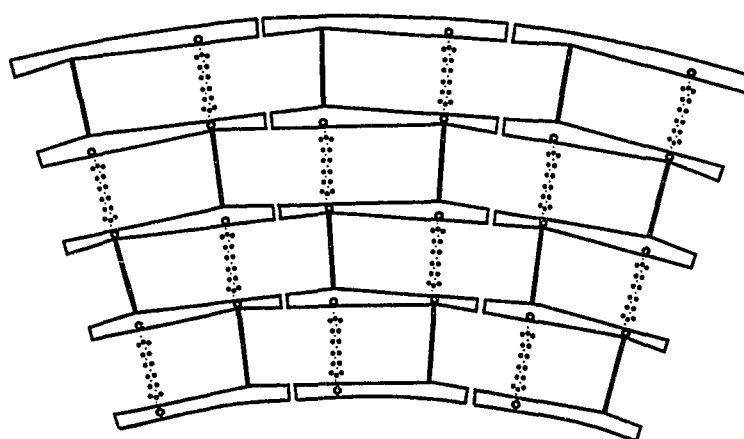


Figure 2.6: Endview of an azimuthal slice of the CDC.

Forward Drift Chamber

The two Forward Drift Chambers extend the forward-backward coverage of the CD tracking capabilities from where the CDC ends down to $5^\circ \lesssim \theta \lesssim 175^\circ$. An exploded view of an FDC is given in Figure 2.8 which also indicates the orientations of the sense wires for the different modules. Each FDC consists of two Θ modules sandwiching a Φ module. The Θ modules are segmented into four quadrants, each containing six rectangular cells at increasing radii. Each cell has eight sense wires

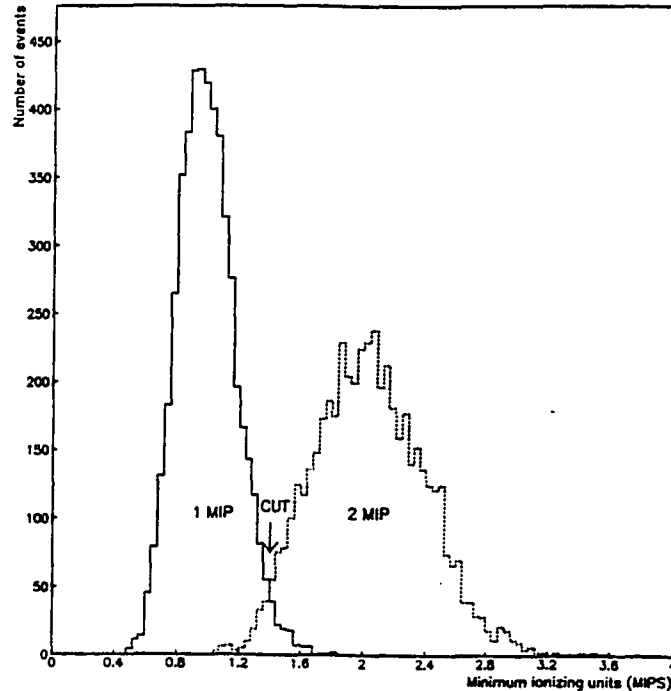


Figure 2.7: dE/dx for one and two tracks in the CDC.

Table 2.3: CDC detector parameters.^{30,32}

Overall Active Radii	49.5 cm – 74.5 cm
Number of Concentric Layers	4
Active Length	184 cm
Number of Cells per Layer	32
Number of Sense Wires	7 per cell; 896 total
Sense Wire Separation	6.0 mm radially with 200 μm stagger
Wire Specifications	Sense Wires: 30 μm Au plated W; 110 g tension Field Wires: 125 μm Au plated CuBe; 670 g tension
Sense Wire Voltage	1.45 kV (inner 5); 1.54 kV (outer 2)
Gas	Ar 92.5%; CH ₄ 4%; CO ₂ 3%; H ₂ O 0.5%
Average Drift Field	0.620 kV/cm
Average Drift Velocity	34 $\mu\text{m}/\text{nsec}$
Maximum Drift Distance	7 cm
Delay Lines	2 per cell; 256 total
Delay Line Velocity	2.35 mm/ns
Position Resolution	ρ - ϕ : 150 ~ 200 μm z : \approx 2 mm

organized in planes parallel to the z -axis and normal to the radial direction at the midpoint of the cell. The sense wires in the inner three layers are at one edge of the cell to remove the left-right ambiguity in the track reconstruction. Each of these Θ cells has one delay line identical to that of the CDC. Within an FDC, the two Θ modules are rotated 45° with respect to each other. The Φ modules are segmented into 36 azimuthal cells, each containing 16 sense wires extending outward radially. The arrangement of the sense wires within a cell lie in a plane containing the z -axis. Unlike the Θ cells, the Φ cells are not equipped with any delay lines for measurements along the directions of the sense wires. The position resolutions in the drift directions for the Θ and Φ modules are $\approx 250 \mu\text{m}$ and $\approx 200 \mu\text{m}$, respectively. Selected parameters for the two types of FDC modules are collected in Table 2.4.

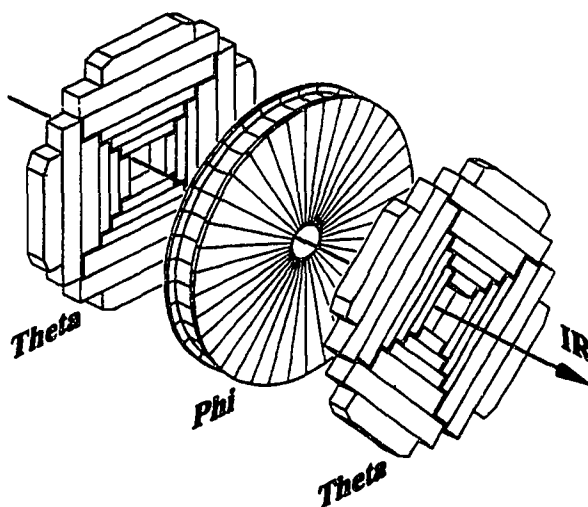


Figure 2.8: Exploded view of the FDC.

Table 2.4: FDC detector parameters.^{30,32}

	Θ	Φ
Radius	11.0 – 62 cm	11.0 – 61.3 cm
z Boundaries	104.8 – 111.2 cm 128.8 – 135.2 cm	113.0 – 127.0 cm
Number of Cells/Layer	4 quadrants of 6 cells	36 azimuthally
Number of Sense Wires	8/cell; 384/FDC	16/cell; 576/FDC
Sense Wire Separation	8.0 mm in z with 200 μm stagger	
Sense Wire Voltage	1.66 kV	1.55 kV
Wire Specifications	Sense Wires: 30 μm Au plated W; 50 – 100 g tension Field Wires: 163 μm Au plated Al; 100 – 150 g tension	
Delay Lines	1/cell; 48/FDC	None
Delay Line Velocity	2.35 mm/ns	–
Gas	Ar 93%; CH ₄ 4%; CO ₂ 3%; H ₂ O 0.5%	
Average Drift Field	1.0 kV/cm	
Average Drift Velocity	40 $\mu\text{m}/\text{ns}$	37 $\mu\text{m}/\text{ns}$
Maximum Drift Distance	5.3 cm	
Drift Position Resolution	$\approx 250 \mu\text{m}$	$\approx 200 \mu\text{m}$

2.3.2 Calorimeters

There are three calorimeters to provide hermetic coverage ($|\eta| \lesssim 4.5$) as well as a modular design to easily accommodate the CD subdetectors. The three calorimeters are the Central Calorimeter ($|\eta| \lesssim 1.0$) and two End Calorimeters ($0.8 \lesssim |\eta| \lesssim 4.5$). Figure 2.9 shows the arrangement of the CC and ECs along with the CD subdetectors within. Each of the calorimeters is designed to measure energies of electrons and hadrons and is thus equipped with less absorbing material close to the interaction region (in the EM layers) to accommodate the early electromagnetic showering of electrons while having increased absorber further away (in the Fine Hadronic and Coarse Hadronic layers: FH and CH) to contain and measure the more penetrating hadrons. Appended to the poorly instrumented region between the CC and ECs are more detecting devices in the form of ionization induced charge collectors (Massless

Gaps) and scintillators (InterCryostat Detectors or ICDs). A description of the basic calorimeter cell is very instructive before discussing the arrangements of these cells within the CC and ECs.

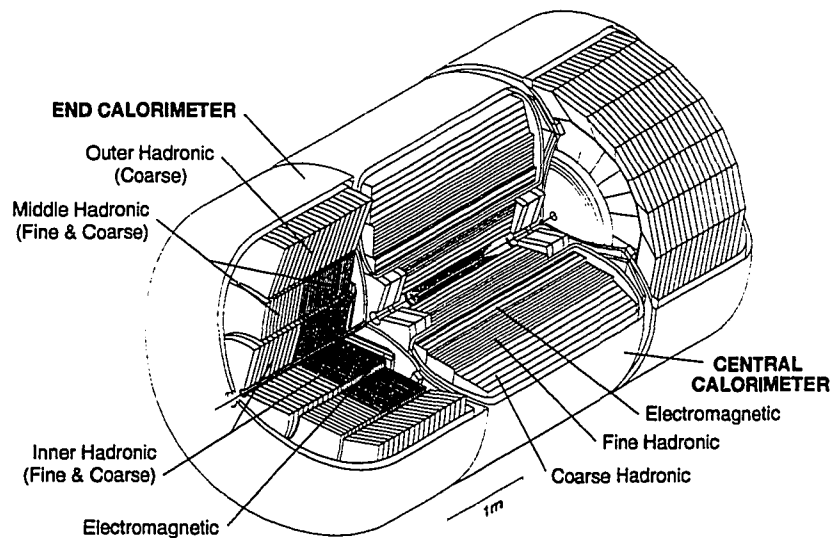


Figure 2.9: Isometric view of the CC and two ECs along with the CD encased within.

Typical Calorimeter Cell

A typical calorimeter cell is shown in Figure 2.10. It consists of an absorber and a signal board, both submerged in liquid argon at a temperature of 78 °K. The basic operation is to measure the energy of a particle as it traverses the absorber, imparting some of its energy to the debris of lower energy particles. The subset of charged particles in the debris ionize the liquid argon and the resulting electrons drift toward the signal board with the aid of an electric field. These electrons then induce the signal charges on the signal board.

The absorbers vary in both material and size, depending on its distance in radiation/interaction lengths from the $p\bar{p}$ interaction region. The absorber plates in the EM layers are made of depleted uranium 3 mm (4 mm) thick in the CC (EC), while the FH layers are uranium–niobium (2%) 6 mm thick. The CH sections contain 46.4 mm thick plates of copper (stainless steel) in the CC (EC).

At the center of the signal board are copper readout pads formed in the $\Delta\eta \times \Delta\phi = 0.1 \times 0.1$ segmentation. These copper pads are sandwiched between two dielectric G-10 boards 0.5 mm thick. The outer surfaces of the G-10 boards are coated with a highly resistive ($\sim 40 \text{ M}\Omega/\square$) carbon-loaded epoxy.

The electric field that causes the electrons to drift across the gap is produced by subjecting the highly resistive epoxy surfaces to a large positive voltage (2.0–2.5 kV) while grounding the absorber. The maximum drift time across the 2.3 mm gap is $\approx 450 \text{ ns}$.

The signals induced on signal boards from different layers are ganged together to form one particular readout. The number of layers involved vary as discussed below and summarized in Tables 2.5 and 2.6.

Central Calorimeter

The Central Calorimeter (CC) is comprised of three major components which primarily differ in the amount of absorber material and sampling rate. The arrangement is in concentric cylinders with the innermost member stressing the detection of electrons via electromagnetic radiation (and pair production) and is appropriately called the electromagnetic portion of the CC, or CCEM. Around the CCEM are the Middle Hadronic and Outer Hadronic Central Calorimeters, or CCMH and CCOH,

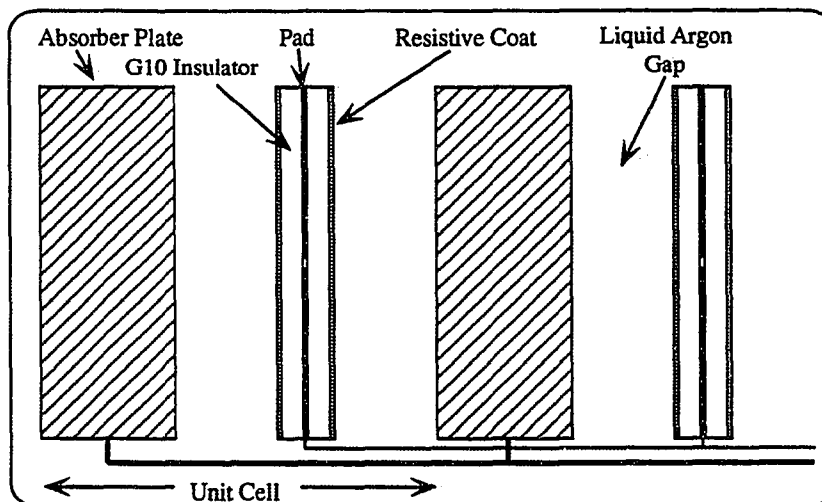


Figure 2.10: Typical calorimeter cell.

where the CCOH has the most absorbing material to contain the hadrons at the expense of a poorer sampling rate.

The CCEM consists of 32 azimuthally segmented modules that extend the full z range of the CC. Within each CCEM module, the absorbers and signal boards are arranged with the $\Delta\eta \times \Delta\phi = 0.1 \times 0.1$ segmentation, except for the cells in the third depth readout which have $\Delta\eta \times \Delta\phi = 0.05 \times 0.05$ granularity. Cells in the same $(\Delta\eta, \Delta\phi)$ tower are ganged together along the direction of the tower in groups of 2, 2, 7, and 10 corresponding to 2.0, 2.0, 6.8, and 9.8 radiation lengths. More details of the CCEM are given in Table 2.5.

The CCFH and CCCH both consist of 16 azimuthally segmented modules, extending the entire z range of the CC. The transverse arrangements of the cells within both modules obey the $\Delta\eta \times \Delta\phi = 0.1 \times 0.1$ segmentation. Cells are ganged in the (Δ, ϕ) towers of 20, 16, and 14 corresponding to 1.3, 1.0, 0.9 interaction lengths,

while the CCCH modules contain just one ganging of nine cells with 3.2 interaction lengths. More details of the CCFH and CCCH are summarized in Table 2.5.

Table 2.5: Central Calorimeter Module Parameters.^{30,32}

	EM	FH	CH
Number of Modules	32	16	16
Absorber	U	UNb	Cu
Absorber Thickness (mm)	3	6	46.5
Argon Gap (mm)	2.3	2.3	2.3
Number of Readout Layers	4	3	1
Cells per Readout Layer	2, 2, 7, 10	20, 16, 14	9
Total Radiation Lengths (X_0)	20.5	96.0	32.9
Total Interaction Lengths (λ)	0.76	3.2	3.2
Sampling Fraction (%)	11.79	6.79	1.45

End Calorimeters

The End Calorimeters consist of four components as shown in Figure 2.9. They are the electromagnetic (ECEM), the Inner Hadronic (ECIH), the Middle Hadronic (ECMFH), and the Outer Hadronic (ECOH) sections. The ECIH and ECMH have both fine and coarse sampling sections, while the ECOH has only the coarse. Thus, the ECIH is subdivided into the Inner Fine Hadronic (ECIFH) and the Inner Coarse Hadronic (ECICH) portions; the ECMH is similarly apportioned into the Middle Fine Hadronic (ECMFH) and Middle Coarse Hadronic (ECMCH) sections. The ECEM and ECIH were not constructed in a modular fashion as was done for the CC. Instead, these were each made as one module. Details for the particular makeup of the cells as well as the ganging arrangements for their readouts are provided in Table 2.6.

Table 2.6: End Calorimeter Module Parameters.^{30,32}

* The ECIFH and ECICH, together, make up one ECIH module.

** Each ECMH module (there are 16) consists of a fine (ECMFH) and a coarse (ECMCH) section.

	EM	IFH	ICH	MFH	MCH	OH
Number of Modules	1	1*	1*	16**	16**	16
Absorber	U	UNb	SS	UNb	SS	SS
Absorber Thickness (mm)	4	6	46.5	6	46.5	46.5
Argon Gap (mm)	0.23	0.21	0.21	0.22	0.22	0.22
Number of Readout Layers	4	4	1	4	1	3
Cells per Readout Layer	2, 2, 6, 8	16	14	15	12	8
Total Radiation Lengths (X_0)	20.5	121.8	32.8	115.5	37.9	65.1
Total Interaction Lengths (λ)	0.95	4.9	3.6	4.0	4.1	7.0
Sampling Fraction (%)	11.9	5.7	1.5	6.7	1.6	1.6

Massless Gaps and InterCryostat Detectors

As seen in Figure 2.11, the region $0.8 \lesssim |\eta| \lesssim 1.4$ contains a large amount of uninstrumented material. In order to reconcile the energy loss in the uninstrumented material, a ring of signal boards is placed on the endplates of the CCFH modules, as well as on the frontplates of the ECMH and ECOH modules with the standard $\Delta\eta \times \Delta\phi = 0.1 \times 0.1$ segmentation. Because the signal boards are not accompanied with any absorbers, these detecting devices are called the massless gaps.

Further rectification of the energy loss in the dead material is accomplished with the introduction of two scintillation counter arrays placed between the cryostats of the CC and ECs called the InterCryostat Detectors (ICDs). The actual mounting is on the front surface of the ECs. Each ICD consists of 384 scintillator tiles to provide the standard $\Delta\eta \times \Delta\phi = 0.1 \times 0.1$ transverse granularity. The massless gaps and ICDs are both shown in Figure 2.11.

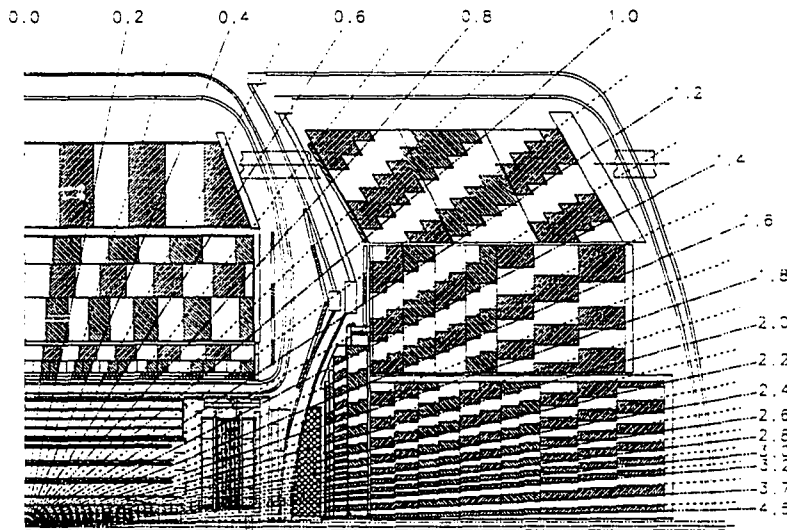


Figure 2.11: Side view of a quarter of the calorimeter and tracking chambers.

Calorimeter Performance

A discussion on the energy resolution for jets will be deferred to the chapter discussing identification of particles. A measure of the calorimeters' performance was conducted in a test beam environment. Single electrons were directed onto the ECEM module, while charged pions were aimed onto an ECMH module. The energy resolutions for both can be parameterized by the functional form:

$$\left(\frac{\sigma_E}{E}\right)^2 = C^2 + S^2 \cdot \frac{1}{E} + N^2 \cdot \frac{1}{E^2} \quad (2.5)$$

where the constants C , S , and N represent the calibration errors, sampling fluctuations, and noise contributions, respectively. The measured energy resolution constants for electrons are $C = 0.003 \pm 0.002$, $S = 0.157 \pm 0.005 \sqrt{\text{GeV}}$, and $N \approx 0.140 \text{ GeV}$, while the corresponding values for charged pions are $C = 0.032 \pm 0.004$, $S = 0.41 \pm 0.04 \sqrt{\text{GeV}}$, and $N \approx 1.25 \text{ GeV}$.^{30,33}

2.3.3 Muon Detectors

The detection of muons relies on the virtue that muons are typically the only charged particles that are able to penetrate the vast amount of calorimeter material. This is due to the muon's lack of strong interactions as well as its heavy mass ($\approx 200m_e$) that discourages the creation of an electromagnetic shower. The Muon Detectors are appropriately placed outside the calorimeters and consist of the Wide Angle Muon System (WAMUS) with coverage of $|\eta_\mu| \lesssim 2.5$ and the Small Angle Muon System (SAMUS) designed to be sensitive to forward-backward muons in the range $2.5 \lesssim |\eta_\mu| \lesssim 3.6$. The improbability of hadrons surviving up to the entrance and exit of the muon toroids is illustrated in Figure 2.12 in terms of the nuclear interaction lengths. A side view of the entire DØ detector which shows the various toroids and muon PDTs to be discussed below is given in Figure 2.13.

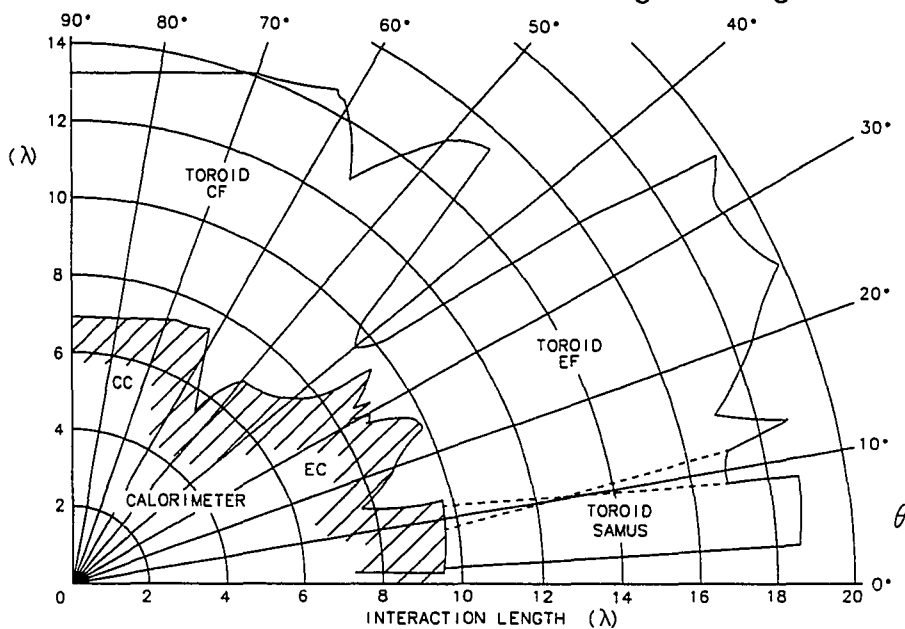


Figure 2.12: Nuclear interaction lengths vs. polar angle.³⁰

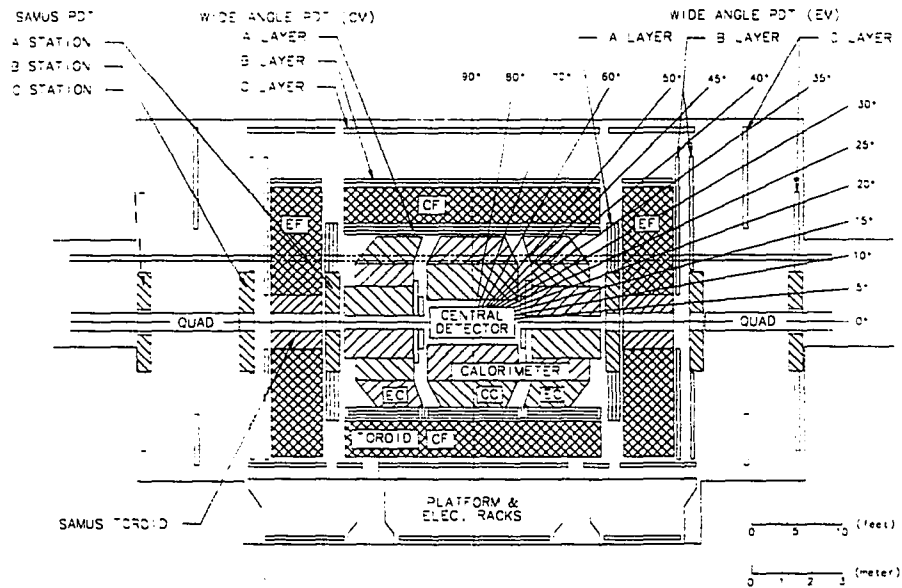


Figure 2.13: Side view of the $DØ$ detector showing the five toroids and three layers of PDT muon chambers.³⁰

Wide Angle Muon System

The Wide Angle Muon System (WAMUS) consists of three toroids and 164 chambers of proportional drift tubes (PDTs). The three toroids are the CF (Central Fe) encompassing $|\eta_\mu| \lesssim 1$ and two EFs (End Fe) covering $1 \lesssim |\eta_\mu| \lesssim 2.5$. The field lines within each toroid are in the azimuthal direction. The 164 PDT chambers are arranged to have one layer (the A layer) alongside the magnet's edge on the interaction side and two layers (the B and C layers) on the other side of the magnet with the B layer flush against the magnet. The directions of the sense wires in the PDT chambers are roughly parallel to the directions of the magnetic field lines in the toroid in order to maximize the sensitivity of a measurement in the bending direction (polar angle θ with respect to the beam direction) induced by the magnet

on a charged particle. The A layer chambers are made with four planes of PDTs while the B and C layer chambers consist of three. The extra plane in the A layer chambers is to enhance the determination of the muon's direction before the magnet compared to the B and C layer chambers which typically have a lever arm of $\geq 1\text{m}$ to aid their angular measurement of the exiting muon.

As mentioned above, each chamber is composed of three or four planes of PDTs, with 14 to 24 cells in each plane (same number in each plane) of lengths varying between 191 cm and 579 cm (same length in each chamber). The planes within the chambers are staggered to eliminate the left-right ambiguities, as shown in Figure 2.14 for a three plane chamber. Each PDT cell is rectangular in cross section with dimensions $5.5\text{ cm} \times 10.1\text{ cm}$. In each PDT is a sense wire and two cathode pads; each pad being at the top and bottom of the cell. The cathode pads are arranged with a diamond pattern separating the two pads into inner and outer regions with a repeat distance of 61 cm as illustrated in Figure 2.15. A schematic for the end view of a single cell including the equipotential surfaces is shown in Figure 2.16. The sense wires and pads are ganged together in pairs on the end opposite the electronics to allow the readout of the signals to be on one side of the chamber.

A position measurement perpendicular to the wire with a resolution of $\pm 0.53\text{ mm}$ is accomplished with a drift time measurement and knowledge of the drift velocity in the $\text{Ar}(90\%)/\text{CF}_4(5\%)/\text{CO}_2(5\%)$ gas which is typically $6.5\text{ cm}/\mu\text{s}$. A position measurement parallel to the wire is determined in two steps. The first is to measure the difference in arrival times of the signal at the two ends of the signal wire with a precision corresponding to 10 to 20 cm in space. Since this error is smaller than half the repeat distance of the pads, it is able to dictate which

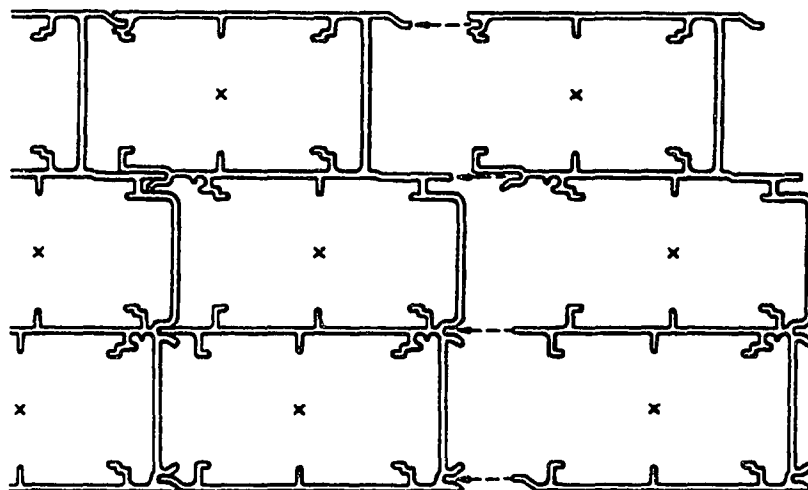


Figure 2.14: Endview of a WAMUS B/C chamber showing the stagger of the cells.³⁰

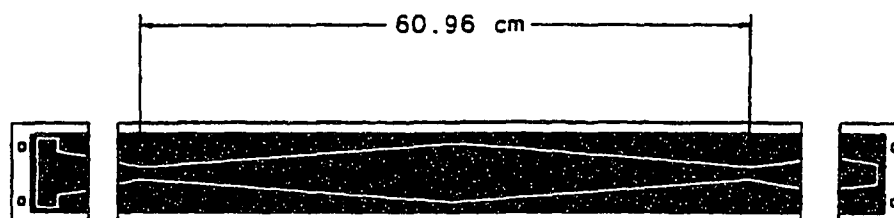


Figure 2.15: The WAMUS cell cathode pad.³⁰

particular half cycle the hit occurred in. Furthermore, the pads in different planes are staggered by 10 cm to reduce ambiguities introduced by the symmetry of the diamond pattern. Once the hit is deduced to be in a particular pad half cycle, the ratio of the amount of charge induced on the inner to outer pad further increases the precision of this position measurement to ± 3 mm. The electronics on the chambers can accommodate up to two hits in order to allow for detection of δ -rays.

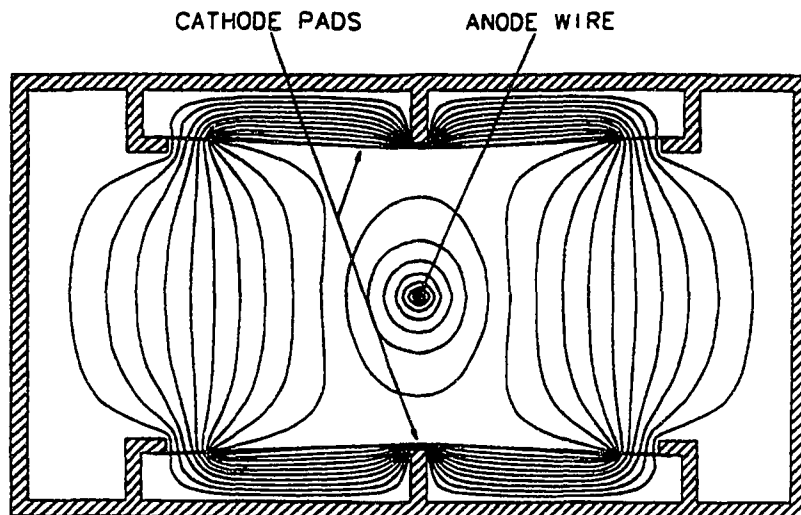


Figure 2.16: Schematic of the end view of a single WAMUS cell with its equipotential surfaces.³⁰

The momentum of a wide angle muon can be measured using the WAMUS alone, through an angular difference between the exiting and entering muon directions in the bending (ρ - z) plane. However, a global fit using information from the Calorimeter and Central Detectors improves the momentum resolution and reduces the fake muon rate. The identification of muons and a discussion of their momentum resolution will be deferred until the chapter dedicated for the identification of particles. More information about the WAMUS is collected in Table 2.7.

Small Angle Muon System

The Small Angle Muon System (SAMUS) is comprised of two toroids located in the forward regions ($2.5 \lesssim |\eta_\mu| \lesssim 3.6$) and six chambers of tightly packed cylindrical PDTs arranged in an A-B-C layer configuration around the toroids, similar to the WAMUS setup which has the A layer chamber situated before the toroid while the B

and C chambers are outside the magnet. Each chamber consists of three orientations of PDTs; the X, Y, and U planes as shown in Figure 2.17(b). The PDTs in the U plane are rotated by 45° with respect to both X and Y planes to aid in the reduction of ambiguities in this high hit multiplicity environment. In each of these planes are two staggered subplanes of cylindrical PDTs as illustrated in Figure 2.17(a). Each PDT has a diameter of 30 mm and is filled with a $\text{CF}_4(90\%)/\text{CH}_4(10\%)$ gas mixture providing an average drift velocity of $9.7 \text{ cm}/\mu\text{s}$. The coordinate resolution in a single drift tube is about 0.3–0.5 mm. Further parameters of SAMUS are given in Table 2.7.

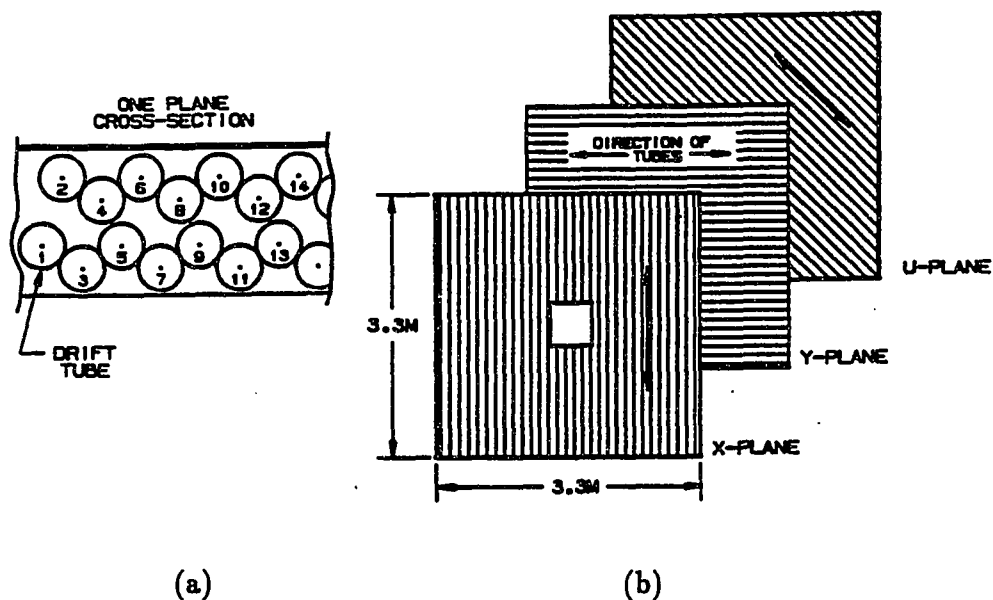


Figure 2.17: Cross section and PDT configurations of a SAMUS chamber.³⁴
 (a) Cross section of a plane in a SAMUS chamber.
 (b) The orientations of the planes in a SAMUS chamber.

Table 2.7: Muon Detector Parameters.^{30,34}

* Region of WAMUS *chambers* only, no overlap with any SAMUS chambers.

** Overlap with WAMUS chambers allowed.

	WAMUS*	SAMUS**
η coverage	$ \eta_\mu \lesssim 1.7$	$1.7 \lesssim \eta_\mu \lesssim 3.6$
Magnetic field	1.9 T	1.9 T
Thickness in λ_A	≈ 13.4	≈ 18.7
Number of modules	164	6
Number of drift cells	11,386	5232
Sense wire specs	50 μm Au-plated W, 300 g tension	50 μm Au-plated W, 208 g tension
Gas	Ar(90%)/CF ₄ (5%)/CO ₂ (5%)	CF ₄ (90%)/CH ₄ (10%)
Sense wire voltage	+4.56 kV	+4.0 kV
Cathode pad voltage	+2.3 kV	-
Maximum drift distance	5 cm	1.45 cm
Average drift velocity	6.5 cm/ μs	9.7 cm/ μs
Bend view resolution	± 0.53 mm	± 0.35 mm
Non-bend view resolution	± 3 mm	± 0.35 mm

Chapter 3

Data Collection and Particle Identification

The collection of data at $D\bar{O}$ proceeds with two levels of filtering that reduces the very high rate (~ 286 kHz) of data from all $p\bar{p}$ collisions, containing mostly uninteresting events, to a manageable speed (~ 2 Hz) that retains the desired interactions. The collected events are then subjected to offline reconstruction and identification of the original particles and their decay products. The objects of interest in this analysis are jets, muons, and a neutrino via missing transverse energy in the entire $D\bar{O}$ detector. Additionally useful is a direct measurement for the transverse momentum of the leptonically decaying W boson through missing transverse energy in the calorimeter only. A brief explanation of the calculation for the amount of data collected concludes this discussion on the Data Collection and Particle Identification.

3.1 Data Collection

The two sequential stages of data reduction begin with a framework of hardware based triggers (LEVEL1) followed by the more sophisticated software driven filters (LEVEL2), whose decisions are determined through quickly reconstructed particles. The LEVEL1 trigger framework receives data at a rate of ~ 286 kHz and passes events satisfying some minimal criteria at ~ 100 Hz. Events passing the LEVEL1

system are then subjected to further scrutiny by the LEVEL2 filters which reduce the data taking rate to ~ 2 Hz that is saved for offline analysis.

The LEVEL1 trigger framework provides 32 trigger conditions based on AND/OR logic decisions involving up to 256 inputs from the calorimeter, muon system, various scintillator and timing vetoes, and LEVEL0. (The LEVEL0 is a set of rectangular scintillators placed between the FDC and EC to detect hard scattering beam crossings. They measure the luminosity and z vertex position.) One of the 32 trigger conditions was reserved for this search for the top quark, $t\bar{t} \rightarrow \mu + \text{jets}$. Of the 256 inputs which the AND/OR logic operated upon, four were used for this search. A logical AND was used on the following hardware trigger conditions:

1. Data taking is turned *on* when a proton bunch in the Main Ring does *not* pass through the $D\bar{O}$ detector.
2. Event vertex determined by LEVEL0 has $|z| \leq 97$ cm.
3. At least one calorimeter trigger tower with $E_T \geq 5$ GeV. (Size of trigger tower is $\Delta\eta \times \Delta\phi = 0.2 \times 0.2$.)
4. At least one set of hits in the muon system with $|\eta_\mu| \leq 1.7$. (Hits are on cathode pads in roads six cells wide.)

Since the transverse size of a typical jet is larger than the trigger tower, there is no direct correspondence between a trigger tower and an offline reconstructed jet. However, in situations where a match between a trigger tower and jet exists, the 5 GeV trigger tower requirement is fully efficient for jets with $E_T \geq 30$ GeV.

Every one of the 32 LEVEL1 trigger conditions has one or more LEVEL2 filter requirements associated with it. An event passing the LEVEL1 trigger will have examined all LEVEL2 filter requirements accompanying the specific LEVEL1 trigger conditions which were satisfied. The LEVEL2 filter requirements are based on a

fast reconstruction of particles. The event reconstruction is performed on one of 48 Vaxstation 4000/60 (upgraded to 4000/90 for Run Ib) nodes which operate in parallel. This analysis imposed both following LEVEL2 requirements:

1. At least one μ with $p_T(\mu) \geq 8$ GeV/c.
2. At least one jet (cone algorithm described below having $\Delta R = 0.7$) with $E_T \geq 15$ GeV.

The quickly reconstructed muons utilize information only from the muon system and include a rejection against cosmic muons based on hits opposite in ϕ and η .³⁵

Events passing *any* LEVEL2 requirement associated with any successful LEVEL1 trigger are saved for offline analysis. Events used in this analysis are the subset that have satisfied both LEVEL1 and LEVEL2 conditions described above.

3.2 Particle Reconstruction and Identification

3.2.1 Jets

Jet Reconstruction

The $D\bar{0}$ standard for reconstructing jets is through a cone algorithm, similar to that used by the UA1 and CDF collaborations.^{36,37} The size of the cone used in the search for the top quark in all channels at $D\bar{0}$ is $\Delta R = \sqrt{(\Delta\eta)^2 + (\Delta\phi)^2} = 0.5$. The procedure consists of the following steps:³⁸

1. Sort the ($\Delta\eta \times \Delta\phi \approx 0.1 \times 0.1$) calorimeter towers in descending E_T .
2. Starting with the highest E_T tower in the list not yet assigned to a precluster, form a precluster by adding up contiguous towers within $|\Delta\eta| < 0.3$ and

$|\Delta\phi| < 0.3$, having $E_T > 1$ GeV. The precluster's (η, ϕ) values are calculated with an E_T weight from these towers.

3. Repeat step 2 until the calorimeter tower list is exhausted.
4. For each precluster generated in steps 2 and 3, form a new E_T weighted (η, ϕ) center from all towers within a cone of $\Delta R \leq 0.5$ around the previous (η, ϕ) center until the centroid of the jet cone stabilizes.
5. Split or merge jets based on the fractional energy shared relative to the lower E_T jet. If the shared energy is greater than 50% of the lower E_T jet, the jets are merged and the (η, ϕ) values are recalculated using all towers. If the shared energy is less than 50%, the jets are split and each shared tower is assigned to the closest jet.
6. Calculate the E_T of all jets, defined by:

$$E_T = \sqrt{E_x^2 + E_y^2} \quad (3.1)$$

where E_x and E_y are the sums of the components of the individual calorimeter cell energies:

$$E_x = \sum_i E_x^i \quad \text{and} \quad E_y = \sum_i E_y^i. \quad (3.2)$$

7. Discard jets below an E_T threshold of 8 GeV.

Jet Energy Corrections

The above procedure to reconstruct jets must be appended with several corrections that remedy the various sources which cause the jet energies to be incorrectly measured. The corrections assume that the *true* jet transverse energies (E_T^{true}) are modified in the following way to produce the *measured* jet transverse energies (E_T^{meas}).^{39,40}

$$E_T^{meas} = R_{had}(E_T, \eta, EMF) E_T^{true} (1 + C(E_T, \eta)) + U + N + Z \quad (3.3)$$

where R_{had} is the overall hadronic response depending on energy, η , and the fraction of energy in the electromagnetic cells (EMF); C is the fraction of energy in calorimeter that is not used in the jet algorithm (cells not in the jet cone); U is the contribution from the underlying event; N is the electronic and Uranium noise (dominated by Uranium); and Z is the systematic error introduced as a result of the “zero suppression” on the readouts of the cells.

The first corrections applied are the energy offsets due to U , N , and Z . The U and N corrections are determined using minimum bias data with the help of the LEVEL0 scintillators that are able to roughly predict the number of interactions in an event. The difference in energies in the cells of events with two interactions from those with one interaction were used to infer the effect of the underlying event which is $\frac{d^2U}{d\eta d\phi} = 0.310 + 0.034\eta_{detector}$. The same inferred result was used on events with one interaction to subtract out the effect of the underlying event, unveiling the magnitude of the noise, $\frac{d^2N}{d\eta d\phi} = 0.196$. Finally, the influence from the zero suppression is obtained by studying the energy offset after the zero suppression operation on cells that have no energy deposited from any real physics process and is measured to be $\frac{d^2Z}{d\eta d\phi} = 1.44 \sin \theta_{detector}$.

The second round of corrections are due to variations in the hadronic energy response, R_{had} , as a function of E_T , η , and EMF . The calculations for these corrections are derived with a single technique called the Missing E_T Projection Fraction (MPF) method. This technique relies on balancing the transverse momentum in events with typically only two objects (and no ν 's), where one of the objects is assumed to be better measured than the other. The better measured object is called the trigger; the other is called the probe. When correcting the

hadronic energy scale *absolutely*, the trigger is a highly electromagnetic jet while the probe is another jet, opposite in ϕ , having a smaller electromagnetic energy fraction. (The electromagnetic energy scale is assumed to be corrected *absolutely* by adjusting the invariant mass peak reconstructed from dielectron events to the Z mass value measured by the LEP experiments.⁴¹) When correcting the hadronic energy scale *relatively* from the CC across to the EC, for example, the trigger is a CC jet and the probe is an EC jet. The hadronic response, $R_{had}(X)$, for any property $X \in \{E_T, \eta, EMF\}$ of the probing jet is given by:

$$R_{had}(X) = 1 + \frac{\vec{E}_T \cdot \hat{E}_T^{trigger}}{E_T^{trigger}} \quad (3.4)$$

where \vec{E}_T is the magnitude and direction of the missing E_T , $E_T^{trigger}$ is the E_T of the triggered object, and $\hat{E}_T^{trigger}$ is its transverse direction. The correction factor, $R_{had}(E_T)$ for two slices of η as a function of the jet E_T are given in Figure 3.1.

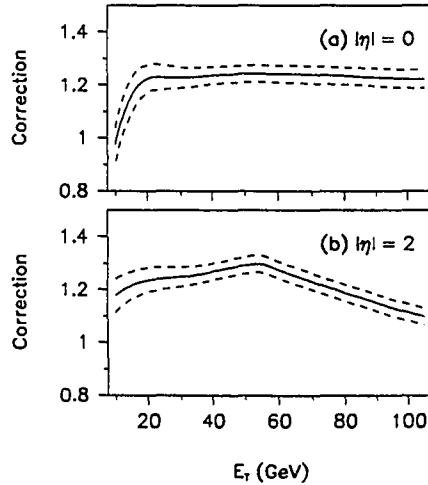


Figure 3.1: Jet energy scale correction as a function of the jet E_T , $R_{had}(E_T)$, in the (a) central, $|\eta| = 0.0$, and (b) forward, $|\eta| = 2.0$, regions.⁴²

The final set of corrections is for the fraction of energy not used in reconstruction (outside the cone), resulting from showering of the individual particles comprising the jet. The magnitude of this effect is calculated using the HERWIG⁴³ MC to produce simulated jets in the CC and measuring the differences in the reconstructed cone jets when applied to the outcomes from the two situations:

1. Hadrons in the jet deposit their energy in the first calorimeter cell encountered.
2. Hadrons are showered with profiles observed at the test beam.

The result for the $\Delta R = 0.5$ cone jets is a maximum value for C of ≈ 0.03 at small energies, vanishing with increasing energies.

Jet Energy Resolution

The resolution of the jet energies is calculated through a global fit⁴² of two data samples to the functional form given in Equation 2.5 which is restated here for convenience:

$$\left(\frac{\sigma_E}{E}\right)^2 = C^2 + S^2 \cdot \frac{1}{E} + N^2 \cdot \frac{1}{E^2} \quad (3.5)$$

with the constants C, S, and N representing the calibration errors, sampling fluctuations, and noise contributions, respectively.

The first data sample is composed of dijets. An asymmetry value, A ,

$$A = \frac{E_{T_1} - E_{T_2}}{E_{T_1} + E_{T_2}}, \quad (3.6)$$

is computed, where $E_{T_{1,2}}$ represents the E_T of the two jets in the event. The error in A may be expressed in terms of the errors in the jet energies as:

$$(\sigma_A)^2 = \left(\left|\frac{\partial A}{\partial E_{T_1}}\right| \sigma_{E_{T_1}}\right)^2 + \left(\left|\frac{\partial A}{\partial E_{T_2}}\right| \sigma_{E_{T_2}}\right)^2. \quad (3.7)$$

Assuming $E_T \equiv E_{T_1} = E_{T_2}$ and $\sigma_{E_T} \equiv \sigma_{E_{T_1}} = \sigma_{E_{T_2}}$ reduces Equation 3.7 to

$$\left(\frac{\sigma_{E_T}}{E_T}\right) = \sqrt{2}\sigma_A. \quad (3.8)$$

The E_T dependent σ_A is measured in the dijet sample and Equation 3.8 is used to convert $\sigma_A(E_T)$ to $\sigma_{E_T}(E_T)$, providing the data points to be fit to the functional form of Equation 3.5.

The other set of data used to extract best fit values of C , S , and N are direct photon + jet events. The well measured photon is used to calculate the correction needed for the jet by balancing the transverse energy in the event. Results of the global fit of both data sets for different η regions are given in Table 3.1.

Table 3.1: Jet energy resolution parameters for different η calorimeter regions.⁴²

η Region	Calibration Term (C)	Sampling Term (S)	Noise Term (N)
$ \eta < 0.5$	0.0 ± 0.005	0.81 ± 0.016	7.07 ± 0.09
$0.5 < \eta < 1.0$	0.0 ± 0.01	0.91 ± 0.019	6.92 ± 0.12
$1.0 < \eta < 1.5$	0.052 ± 0.006	1.45 ± 0.016	0.0 ± 1.4
$1.5 < \eta < 2.0$	0.0 ± 0.014	0.48 ± 0.07	8.15 ± 0.21
$2.5 < \eta < 3.0$	0.012 ± 0.58	1.64 ± 0.13	3.15 ± 2.5

3.2.2 Missing Transverse Energy

The two missing transverse energy quantities used in the search for the top quark are the missing E_T in the calorimeter only (\cancel{E}_T^{cal}) and the missing E_T measured by the entire detector (\cancel{E}_T). (\cancel{E}_T^{cal} is a direct measure of the p_T of the W boson that decays to the μ and ν ; \cancel{E}_T is a direct measure of the p_T of the ν .) \cancel{E}_T^{cal} is calculated by

$$\cancel{E}_T^{cal} = \sqrt{(\cancel{E}_{Tx}^{cal})^2 + (\cancel{E}_{Ty}^{cal})^2} \quad (3.9)$$

where

$$\cancel{E}_{Tx}^{cal} = - \sum_i E_i \sin(\theta_i) \cos(\phi_i) - \sum_j \Delta E_x^j \quad (3.10)$$

and

$$\cancel{E}_{Ty}^{cal} = - \sum_i E_i \sin(\theta_i) \sin(\phi_i) - \sum_j \Delta E_y^j. \quad (3.11)$$

The sums over i in Equations 3.10 and 3.11 include all cells in the calorimeter and ICD; the angles θ_i and ϕ_i are with respect to the reconstructed vertex. The sums on j are over the jets and electrons in the event and account for corrections applied to these objects. The jets here are reconstructed with a larger cone size of $\Delta R = 0.7$ to increase the resolution by minimizing the uncertainty of energies in calorimeter cells outside the cone. The resolution of \cancel{E}_T^{cal} can be parameterized as a linear function of the total amount of energy deposited in the calorimeter, called scalar E_T (ΣE_T), as shown in Figure 3.2.

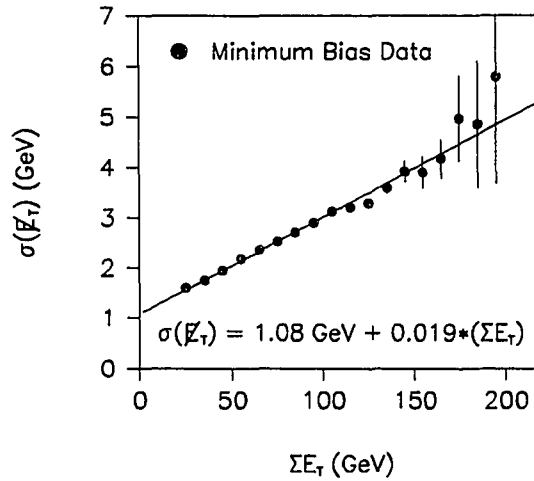


Figure 3.2: Resolution of \cancel{E}_T^{cal} determined from minimum bias data. A linear fit, along with its fit parameters, is also displayed.⁴²

Since muons are essentially invisible to the calorimeter, the \cancel{E}_T in an event is calculated by subtracting the momenta of all muons from \cancel{E}_T^{cal} ,

$$\mathbb{E}_{Tx} = \mathbb{E}_{Tx}^{cal} - \sum_i p_x^{\mu_i} \quad (3.12)$$

and

$$\mathbb{E}_{Ty} = \mathbb{E}_{Ty}^{cal} - \sum_i p_y^{\mu_i}, \quad (3.13)$$

resulting for the total \mathbb{E}_T :

$$\mathbb{E}_T = \sqrt{(\mathbb{E}_{Tx})^2 + (\mathbb{E}_{Ty})^2}. \quad (3.14)$$

In the presence of a high p_T muon, the resolution of the \mathbb{E}_T is dominated by the uncertainty of the muon momentum.

3.2.3 Muons

Muon Reconstruction

Muons are reconstructed globally, utilizing the muon system and the CDC (or FDC).⁴⁴ Activity in the Calorimeter around the expected path of a muon strengthens confidence in its identification. The global reconstruction uses a least squares fit to seven parameters:

- four describing the position and angle of the track before the calorimeter in bend (r - z) and nonbend (x - y) planes,
- two accounting for a change in *direction* of the muon from multiple scattering (MS) in the calorimeter,
 - Lateral *displacement* of muon from MS in calorimeter is ignored.
 - MS in the muon toroid is ignored.
- and one for the fitted muon momentum via its inverse, $\frac{1}{p_\mu}$.

The above seven parameters are fit to 16 data points:

- two describing the longitudinal and transverse vertex position,

- four accommodating the position and angle of a matching CDC track (if there is one) in the bend (r - z) and nonbend (x - y) planes,
- two accounting for angles representing the multiple scattering of the muon in the calorimeter,
- four allowing for the position and angle of an A-layer muon track segment in bend (r - z) and nonbend (x - y) planes,
- and four explaining the position and angle of the BC-layer muon track segment in bend (r - z) and nonbend (x - y) planes.

After the best fit muon momentum is found, a correction is added for the expected energy loss (typically 1–3 GeV) in the calorimeter based on MC simulations. This adjustment does not consider the deposition profile in the Calorimeter of a particular muon, but, rather, corrects on an average basis.

Identification of a Muon From a W Boson Decay

A muon from the decay of a W boson is expected to be isolated and central ($|\eta| \lesssim 1$), with a large p_T ($p_T \gtrsim 15$ GeV/c). The criteria for the muon can be categorized into three logical classes:

1. insuring the quality of the reconstructed muon,
2. rejecting nonisolated muons embedded in jets,
3. rejecting isolated muons originating in the atmosphere from cosmic sources.

To ensure the hits used in a reconstructed muon track were truly produced by a muon, the following criteria are imposed:

- *Minimum Hit Multiplicity*: Typically, a muon track has hits in 7–10 PDT planes. The requirement is to have hits in at least five planes.

- *Minimum Magnetic Path Length:* Muons traversing the thinner part of the toroid ($|\eta| \approx 0.9$) are vulnerable to a small background of punchthrough jets producing hits in the muon chambers, faking the existence of a muon. Also, passage through less toroidal material translates into less magnetic field for its momentum measurement, degrading the resolution. Requiring a minimum amount of integrated magnetic field traversed (or amount of toroid traversed), $\int Bdl \geq 1.83 \text{ T}\cdot\text{m}$, avoids these potential problems.
- *Calorimeter Confirmation:* A muon normally deposits 1–3 GeV in the Calorimeter. If a muon track has a CD track match within $\Delta\eta \leq 0.45$ and $\Delta\phi \leq 0.45$, an energy deposit of at least 0.5 GeV in the Calorimeter is required. If there is no CD track match, the energy deposit requirement is tightened to 1.5 GeV.
- *Muon Quality:* The initial reconstruction based on only the muon system generates a quantity called the *muon quality*. This quantity includes information about the number of modules providing hits on the track, impact parameters, and hit residuals. If a track fails more than one of the cuts imposed on the above quantities, the track is considered to be of poor *quality* and is rejected.

Rejection of nonisolated muons is accomplished by requiring minimal calorimeter activity in the vicinity of the muons:

- Muons must be well separated from any jet (above the reconstructed jet E_T threshold of 8 GeV) by $\Delta R > 0.5$, where ΔR is calculated using the muon track and the jet axis.
- Isolation from calorimeter activity failing jet reconstruction is achieved with an additional requirement that less than 4 (5) GeV of energy be deposited in an annular cone of $0.2 < \Delta R < 0.4$ around the muon direction for tracks in

the CC (EC). The inner cone with $\Delta R < 0.2$ is excluded to allow for energy deposition from bremsstrahlung photons.

Isolated muons from cosmic sources are reduced using track impact parameters, hits with a linear topology, and timing information.

- Three track impact parameter quantities are used:
 - *Impact Parameter (IP)*: *IP* is defined to be the distance of closest approach of the muon track to the reconstructed vertex in the bend plane. The requirement is $IP < 22$ cm.
 - *Bend View Impact Parameter (IP(bend))*: $IP(bend)$ is defined to be the distance between the z intercept of the muon track and the reconstructed vertex in the bend plane. This is required to satisfy $IP(bend) < 20$ cm.
 - *Nonbend View Impact Parameter (IP(nonbend))*: For a downward (or upward) travelling muon, $IP(nonbend)$ is defined to be the distance between the x intercept of the track and the reconstructed vertex in the nonbend plane. For a sideways traversing muon, $IP(nonbend)$ is calculated by the distance between the y intercept and the reconstructed vertex. The criterion is $IP(nonbend) < 20$ cm.
- *Back-to-Back Muons*: Events with hits or a track in the muon chambers opposite in η and ϕ to a reconstructed muon are rejected as likely containing a very energetic muon from a cosmic source.³⁵ The window of rejection is approximately 60 cm in the bend view by 150 cm in the non-bend view.
- *Track Timing*: Cosmic muons enter the muon detector at random times with respect to the $p\bar{p}$ beam crossings. A comparison for the timing of a cosmic muon to one produced by the beam can be made by calculating the best time offset, ΔT_0 , determined in a minimum χ^2 fit for the reconstructed track from

hits in the muon chambers. A loose timing coincidence of the muon track with the $p\bar{p}$ beam crossing is imposed by requiring $|\Delta T_0| < 100$ ns.

Identification of a Muon From a B Quark Decay

A muon decaying from a b quark is expected to have less p_T than that from a W boson and it is also anticipated to have calorimeter activity in its proximity. Therefore, a jet will be considered b-tagged if a nearby muon passes the following conditions:

1. $P_T(\mu) \geq 4$ GeV/c.
2. Must satisfy all quality cuts imposed on the *isolated* muons.
3. Must *fail* the isolation criteria, thus identified as *nonisolated*.

(Note, however, that this analysis will not *require* the existence of such muons and jets.)

Muon Momentum Resolution

The muon momentum resolution is estimated by comparing the invariant mass distribution of real data $Z \rightarrow \mu^+ + \mu^-$ events to those simulated in a smeared MC. The parameterization for the momentum resolution takes on the form:

$$\left(\frac{\sigma(1/p)}{(1/p)}\right)^2 = (C_{MS} \cdot \frac{(p - C_{Eloss})}{p})^2 + (C_{\Delta x} \cdot p)^2, \quad (3.15)$$

where C_{MS} models the multiple Coulomb scattering in the muon toroid, C_{Eloss} accounts for energy losses in the calorimeter and toroid, and $C_{\Delta x}$ accommodates the resolution of the position measurements in the muon system. Real data and MC simulation agree best for values of the three parameters:

- $C_{MS} = 0.18,$

- $C_{Eloss} = 2.$,
- $C_{\Delta x} = 0.008$,

where p is in GeV/c.

3.3 Luminosity

The amount of data accumulated is expressed in terms of an *integrated* luminosity, $\int \mathcal{L} dt$; the *instantaneous* luminosity, \mathcal{L} , is a measure for the rate of data collection and is proportional to the number of beam particles passing through a unit area per unit time. Conventional units for \mathcal{L} are $\text{cm}^{-2}\text{s}^{-1}$. (The typical value for \mathcal{L} during run 1A was $1-10 \times 10^{30} \text{ cm}^{-2}\text{s}^{-1}$.) \mathcal{L} is measured by observing the reaction rate, R , of processes with known cross sections, σ , in the straight-forward relation:

$$R = \sigma \cdot \mathcal{L}. \quad (3.16)$$

The dimensions of cross section is area; the conventional unit is a *barn*, where 1 barn = 10^{-24} cm^2 . (It's tough throwing a baseball to hit the side of *this* barn.) The particular processes used by DØ in its calculation for \mathcal{L} involved inelastic $p\bar{p}$ collisions having an estimated visible cross section of 48.2 mb, determined by averaging measurements from E710 and CDF.⁴⁵ The total amount of data used in this analysis for the top quark is calculated to be:

$$\int \mathcal{L} dt = 45.6 \pm 5.5 \text{ pb}^{-1}. \quad (3.17)$$

Chapter 4

Search For the Top Quark

The search for $t\bar{t} \rightarrow \mu + jets$ events is presented in this chapter. A description of the signal and its backgrounds motivates the use of the variables that are employed in the search. Once the variables have been selected, the expected contribution from the signal and all its backgrounds are calculable for any particular set of cuts on the variables. These calculations for the expected contributions are automated, allowing for an optimization which is based on minimizing the probability that the expected number of background events $\langle n_b \rangle$, with its error σ_b , fluctuates upward to fake the additional expected number of signal events $\langle n_s \rangle$: $P(\langle n_b \rangle \pm \sigma_b \rightarrow \langle n_b \rangle + \langle n_s \rangle)$. The derived optimal selection cuts are then applied to the real data sample, resulting in candidate events for the top quark signal. The number of observed events is found to be more than that anticipated from all known backgrounds; the significance is computed for the expected number of background events, with its errors, to equal or exceed the number of observed events. Finally, a cross section for the production of $t\bar{t}$ events as a function of the top quark mass is calculated based on the number of excess events observed.

4.1 Description of Top and Its Backgrounds

4.1.1 Top Quark Events

Top quarks are believed to be produced in pairs with the predominant production via the quark-antiquark fusion depicted in Figure 4.1. In this search, one of the W bosons is assumed to decay into a μ - ν pair, usually producing a high p_T isolated μ and large missing transverse energy (\cancel{E}_T), while the other W boson is understood to decay into a quark-antiquark pair, resulting in two jets, typically with significant E_T . For top quark masses higher than roughly $120 \text{ GeV}/c^2$, the b quarks' transverse momenta begin to surpass those from the W decay products, yielding two more large E_T jets. The same phenomenon also gives a nontrivial amount of transverse momentum $P_T(W)$ to the W bosons themselves. The spatial distribution of the decay products should also be characteristic of those coming from the decay of a highly massive object which is expected to be somewhat spherical. Finally, one of the b quarks may produce another μ which remains embedded in the jet of the decayed b quark. So, summarizing the $t\bar{t} \rightarrow \mu + \text{jets}$ signatures:

1. One high P_T isolated μ .
2. Possibly a second μ embedded in a jet.
3. Large \cancel{E}_T .
4. Typically four jets with large E_T .
 - Can have more than four jets if a gluon is radiated from any of the signal quarks or from any other parton not even involved in the $t\bar{t}$ decay.
 - Can have fewer than four jets if the jet reconstruction merges two closely spaced partons.

5. Significant $P_T(W)$ if the top quark mass is large.
6. Spherical topology.

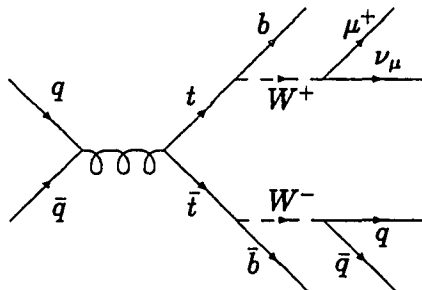


Figure 4.1: Feynman diagram of $t\bar{t}$ production and decay to $\mu + \text{jets}$.

4.1.2 W + Jets Background

The primary background to the $t\bar{t} \rightarrow \mu + \text{jets}$ signal are those events with the production of a real W boson accompanied with the generation of multijets. Figure 4.2 illustrates a typical Feynman diagram describing the production mechanism. Since the W boson is real, the leptonic decay products exhibit similar qualities that are expected for the top signal: an isolated high p_T μ and large \cancel{E}_T . However, since the jets are produced through radiative processes, the jets are expected to have smaller transverse energies. Furthermore, the distribution of the transverse energies among the jets are not expected to be uniform. As for the topology of the jets, one might expect a planar shape for the following reason. Consider the case of a single dominating gluon recoiling against the leptonically decaying W boson as in Figure 4.2. This highly energetic gluon radiates into two less energetic gluons

that define a plane. Subsequent radiative processes of these two gluons are then somewhat bounded to this plane, since further emissions involve lower Q^2 . Note, however, that if a gluon radiates from the \bar{q} in Figure 4.2 and also forms a jet, the topology of the jets in the event becomes less planar. The collection of features of the main background can be classified into two categories. Inherent properties similar to the top quark signal form the first category:

1. One high P_T isolated μ .
2. Large \cancel{E}_T .

while those different in nature comprise the second:

1. Jets with smaller E_T .
2. E_T of jets not evenly distributed.
3. Topology of jets perhaps planar.

4.1.3 QCD Background

A background which has no physical underlying similarities to the signal, but can nevertheless produce events looking like those of top, are purely multijet events with the decay of one of its jets providing a μ . To appear as a top signal event, the jet containing the μ must also have its hadronic activity fluctuate low to give the illusion of an isolated μ as shown in Figure 4.3. This hadronic fluctuation may be physical where no additional missing transverse energy is introduced. (Physically, this is the situation of the μ decaying in the boost direction of its parent while the other decayed siblings are projected against the boost.) But, the source of the hadronic fluctuation may also be due to a mismeasurement of the hadronic energy which can also create false missing transverse energy in the event. A nontrivial

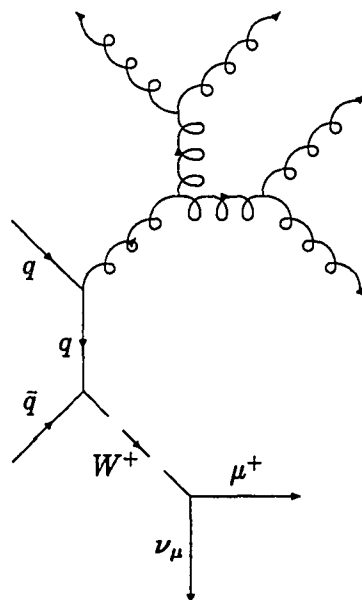


Figure 4.2: Feynman diagram of W + Jets background.

amount of \cancel{E}_T is required for the event to look like the top quark signal. A very likely cause for large false \cancel{E}_T is a mismeasurement of the μ momentum. As stated earlier in Equation 3.15, the momentum resolution of muons is:

$$\left(\frac{\sigma(1/p)}{1/p}\right)^2 = \left(0.18 \cdot \frac{(p-2)}{p}\right)^2 + (0.008 \cdot p)^2, \quad (4.1)$$

where the units of the μ momentum are in GeV/c. The gaussian resolution in $1/P(\mu)$ results in an asymmetric error in $P(\mu)$ giving rise to a substantial chance of observing wrongly measured muons with very large momenta. Table 4.1 shows the 1σ and 2σ confidence level limits for a few examples of measured μ momenta using Equation 4.1. Although the magnitude of the \cancel{E}_T is affected by a poorly measured μ momentum, the component of the \cancel{E}_T perpendicular to the μ direction remains unchanged.

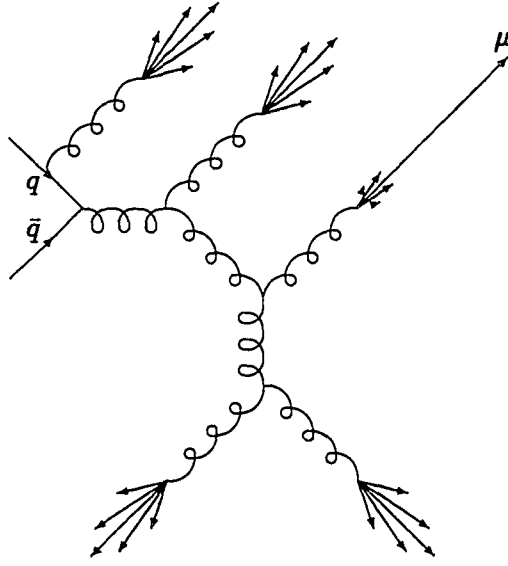


Figure 4.3: Feynman diagram of QCD background.

Table 4.1: Examples of upper and lower limits for measured μ momenta. All momenta entries are in GeV/c.

$p_{measured}(\mu)$	$\frac{\delta(\frac{1}{P(\mu)})}{P(\mu)}$	$P^{-2\sigma}(\mu)$	$P^{-1\sigma}(\mu)$	$P^{+1\sigma}(\mu)$	$P^{+2\sigma}(\mu)$
15	0.197	10.8	12.5	18.7	24.7
20	0.228	13.7	16.3	25.9	36.7
25	0.260	16.5	19.9	33.8	52.0
30	0.293	18.9	23.2	42.4	72.4
40	0.363	23.2	29.4	62.8	146.
50	0.436	26.7	34.8	88.6	389.
70	0.587	32.2	44.1	169.	∞
100	0.819	37.9	55.0	553.	∞

Jet production is primarily through radiative processes as in the primary background. The jets are thus expected to exhibit properties similar to the $W + jets$

background. Since the QCD background has no inherent resemblance to the signal, its attributes are only those different from the signal:

1. Usually smaller values of $P_T(\mu)$, \cancel{E}_T , and $P_T(W)$ than top signal, unless μ momentum is grossly mismeasured.
2. Jets with less E_T .
3. E_T of jets not evenly distributed.
4. Topology of jets perhaps planar.

4.1.4 Z + Jets Background

The final background considered is almost identical to the primary one. It is the production of a real $Z(\rightarrow \mu^+ + \mu^-)$ boson along with multijets where one of the muons from the Z boson is either undetected or embedded in a jet to falsely tag that jet as a b quark jet. A Feynman diagram representing this Z + jets background is presented in Figure 4.4.

In the case where one μ goes undetected, the μ essentially replaces the ν in the W + jets background topology. This is so because the missing μ is a daughter of a massive Z boson decay just as the ν is the result of a massive W boson decay. The dynamics of the jets are identical in both situations. So, both feature lists of the W + jets background apply here for the undetected μ case.

For the situation of the μ accidentally being embedded in a jet, since both muons are found, the \cancel{E}_T is expected to be small here. Summarizing the salient properties of the $Z(\rightarrow \mu^{iso} + \mu^{nonisol}) + jets$ background into the two classes, the first includes those comparable to the signal:

1. High P_T isolated μ .

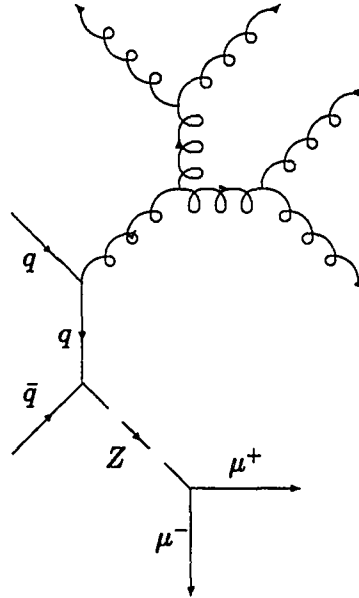


Figure 4.4: Feynman diagram of Z + Jets background.

2. A second μ embedded in a jet.

while the second accommodates ones which differ from top:

1. Smaller \cancel{E}_T than the top signal.
2. Jets with less E_T .
3. E_T of jets not evenly distributed.
4. Topology of jets perhaps planar.

4.2 The Variables

The variables used to separate the top signal from all its backgrounds are chosen to exploit the different distinguishing features discussed above. However, before a

discussion about the variables can begin, it is necessary to explain the different samples that will be used to study the behavior of the signal and its backgrounds. Top quark signal events for various masses are generated with the ISAJET⁴⁶ MC, unless specified otherwise. The $W + \text{jets}$ and $Z + \text{jets}$ backgrounds are produced with the VECBOS⁴⁷ MC. (The jet activity in events produced by the VECBOS MC is verified with data, as shown in Appendix A.) All MC events are subjected to a detector simulation *via* the DØ shower library. The nominal cuts imposed on the top and $W + \text{jets}$ events at the outset are:

- Exactly one isolated μ with $P_T \geq 15 \text{ GeV}/c$ and $|\eta| \leq 1.0$
- Four or more jets with $E_T \geq 15 \text{ GeV}$ and $|\eta| \leq 2.0$
- $\cancel{E}_T \geq 15 \text{ GeV}$
- $\cancel{E}_T^{cal} \geq 15 \text{ GeV}$

while those of the $Z + \text{jets}$ are:

- Exactly one isolated μ with $P_T \geq 15 \text{ GeV}/c$ and $|\eta| \leq 1.0$
- Three or more jets with $E_T \geq 15 \text{ GeV}$ and $|\eta| \leq 2.0$.

The QCD background will be described by two different real data samples. The first sample, QCD($\mu^{nonisol}$), is selected to study the μ and missing transverse energy quantities. The requirements are:

- Passing the signal LEVEL1 and LEVEL2 triggers defined on pages 65 and 66, respectively.
- Exactly one nonisolated μ with $P_T \geq 15 \text{ GeV}/c$ and $|\eta| \leq 1.0$.
- Two or more jets with $E_T \geq 15 \text{ GeV}$ and $|\eta| \leq 2.0$.

The second QCD real data sample, QCD(5 jets), is chosen to examine the quantities involving the jets. The necessary conditions are:

- Triggered on the Run Ia one jet trigger with E_T threshold at 30 GeV for cone size $R = 0.7$.
- Five or more jets with $E_T \geq 15$ GeV and $|\eta| \leq 2.0$.
- At least one jet in fiducial μ region of $|\eta| \leq 1.0$ and with $E_T \geq 15$ GeV.

Of the jets in the fiducial μ region, one is randomly selected to simulate the μ . All jet quantities are then calculated with respect to the remaining jets.

Distributions of any variable for the signal and the backgrounds will refer to the data samples just described, unless specified otherwise.

The first group of variables that will be used to separate the top signal from its copious backgrounds are driven by the leptonic decay of the W boson which should produce a central, isolated, high p_T μ and significant missing transverse energy, \cancel{E}_T . Figure 4.5 shows the $\eta(\mu)$ distribution of top MC events generated with $m_{top} = 180$ GeV/ c^2 , Top(180), before and after μ trigger efficiencies are taken into account and provides the motivation to restrict the search to isolated muons with $|\eta(\mu)| \leq 1.0$. (The top MC data sample used to make Figure 4.5 has had the $|\eta(\mu)| \leq 1.0$ requirement relaxed to $|\eta(\mu)| \leq 1.7$.) The transverse momentum of the isolated μ , $P_T(\mu)$, and the \cancel{E}_T are two variables which will be used to separate the signal from the backgrounds. Figures 4.6 and 4.7 display distributions of these variables for a top signal of mass 180 GeV/ c^2 as well as for all three backgrounds considered. It is worth noting that the distributions of $P_T(\mu)$ and \cancel{E}_T for the top signal are not very sensitive to the value of its mass.

Because a poorly measured μ momentum can easily introduce a large amount of false \cancel{E}_T into an event, it is desirable to have a quantity which calculates the minimum value of \cancel{E}_T in an event regardless of the μ momentum. The geometry

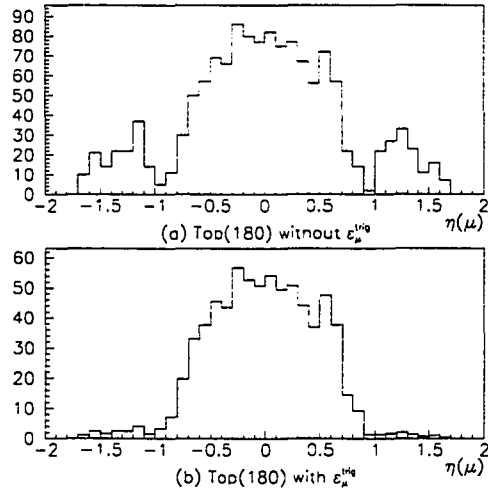


Figure 4.5: Distribution of $\eta(\mu)$ for Top(180) before and after the μ efficiencies are considered. Normalization is arbitrary.

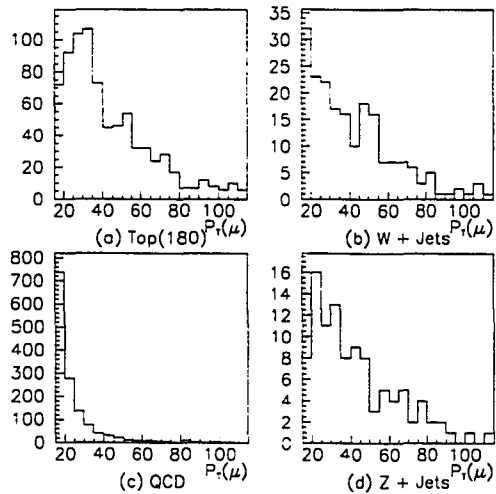


Figure 4.6: Distribution of $P_T(\mu)$ (GeV/c) for Top(180) and its backgrounds. Normalization is arbitrary.

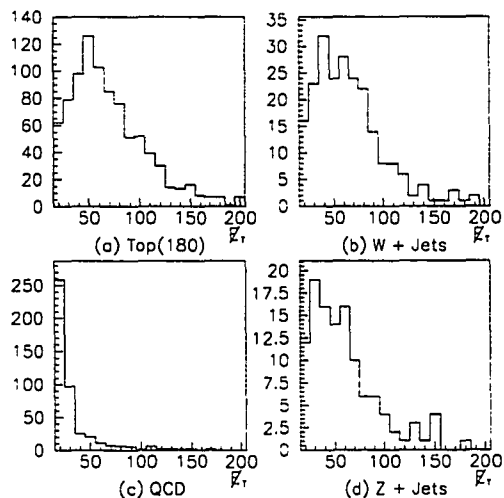


Figure 4.7: Distribution of E_T (GeV) for Top(180) and its backgrounds. Normalization is arbitrary.

for the μ and E_T^{cal} that are used to calculate such a quantity is shown in Figure 4.8.

Note that the calorimeter effectively does not see the μ , so:

$$\vec{E}_T^{cal} = \vec{\nu}_T + \vec{\mu}_T = \vec{E}_T + \vec{\mu}_T$$

or

$$\vec{E}_T = \vec{E}_T^{cal} - \vec{\mu}_T.$$

where the transverse projections of the 3-momenta $\vec{\mu}$ and $\vec{\nu}$ are $\vec{\mu}_T$ and $\vec{\nu}_T$. Figure 4.8(a) depicts the scenario where the directions of the μ and E_T^{cal} are in opposite ϕ -hemispheres, $\delta\phi(\mu, E_T^{cal}) \geq \frac{\pi}{2}$. If one is to allow the μ momentum to take on all possible values from 0 to ∞ GeV/c, the available solutions for \vec{E}_T are represented by the family of vectors whose arrows terminate on the dashed line. Irrespective of the momentum for the μ , the minimal value of E_T (E_T^{min}) in the event is E_T^{cal} . Figure 4.8(b) illustrates the situation where the μ and E_T^{cal} are in the same ϕ -hemisphere. If $\delta\phi(\mu, E_T^{cal})$ is the difference in the azimuthal angle between the μ

and \vec{E}_T^{cal} directions, the minimum value that E_T can have, independent of the μ momentum, is $E_T^{cal} \cdot \sin(\delta\phi(\mu, \vec{E}_T^{cal}))$. (Note that the evaluation of E_T^{min} assumes the presence of only one muon. Expanding the algorithm for multiple muons results in unacceptable losses in efficiency for the top signal (reduced by $\sim 7\%$ for $m_{top} = 180 \text{ GeV}/c^2$), while having only a modest gain in rejection against the QCD background (lowered by $\sim 0.2\%$.) Distributions of E_T^{min} for the top quark signal and its backgrounds are shown in Figure 4.9. The QCD fake background is observed to be substantially reduced with the use of this variable. (See Appendix B for a comparison between a cut on E_T^{min} and a contour cut in $\Delta\phi(\vec{\mu}, \vec{E}_T) - E_T$ space.)

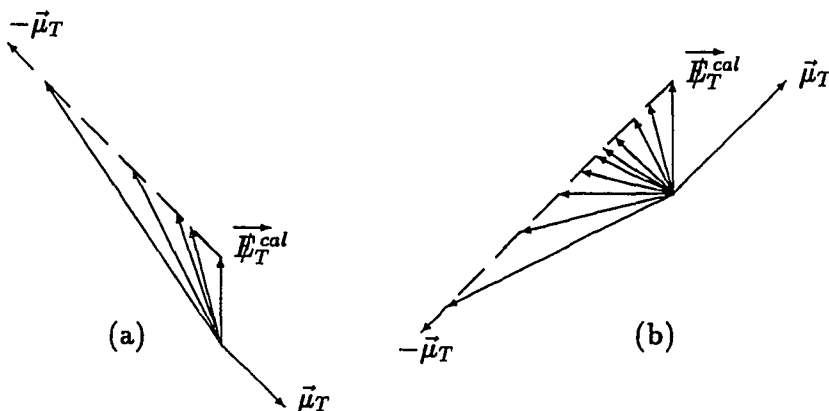


Figure 4.8: Geometry for E_T^{min} variable in the transverse plane.

- (a) Case of $\delta\phi(\mu, \vec{E}_T^{cal}) \geq \frac{\pi}{2}$: $E_T^{min} = E_T^{cal}$.
- (b) Case of $\delta\phi(\mu, \vec{E}_T^{cal}) < \frac{\pi}{2}$: $E_T^{min} = E_T^{cal} \cdot \sin(\delta\phi(\mu, \vec{E}_T^{cal}))$.

The final variable that is related to the leptonically decaying W boson is the p_T of the boson itself. It was remarked above that the μ is effectively invisible to the calorimeter, resulting in

$$\vec{E}_T^{cal} = \vec{v}_T + \vec{\mu}_T = \vec{W}_T$$

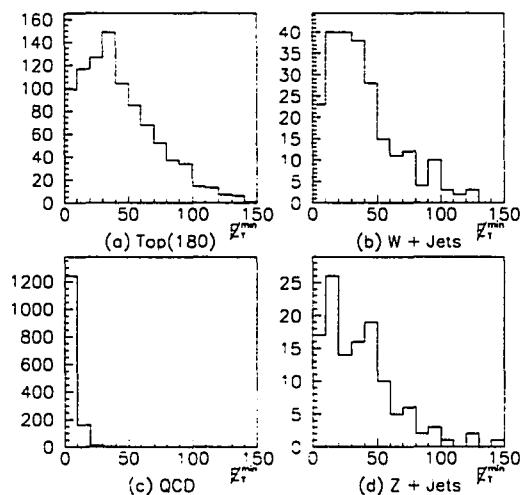


Figure 4.9: Distribution of E_T^{min} (GeV) for Top(180) and its backgrounds. Normalization is arbitrary.

where \vec{W}_T is the transverse projection of the 3-momentum for the W boson. Hence, E_T^{cal} is a direct measure for the p_T of the boson. Figure 4.10 displays the behavior of E_T^{cal} for the signal and its backgrounds.

The second group of variables used to disentangle the top quark signal from its backgrounds are motivated by the jet activity characteristic of that coming from the decay of a massive object. Recall that if all the decay products of the $t\bar{t}$ system are seen by the detector, four central jets of significant transverse energies are expected to be observed. Thus, a natural requirement for all events is to demand the presence of four central jets above a transverse energy threshold. Figure 4.11 shows the η distributions for the four highest E_T jets in top MC events with a top quark mass of 180 GeV/ c^2 and demonstrates that a requirement of $|\eta| \leq 2.0$ is very efficient for the signal. (The top MC data sample used to make Figure 4.11 has had the $|\eta(jet)| \leq 2.0$ requirement relaxed to $|\eta(jet)| \leq 4.0$.) Resorted jet distributions,

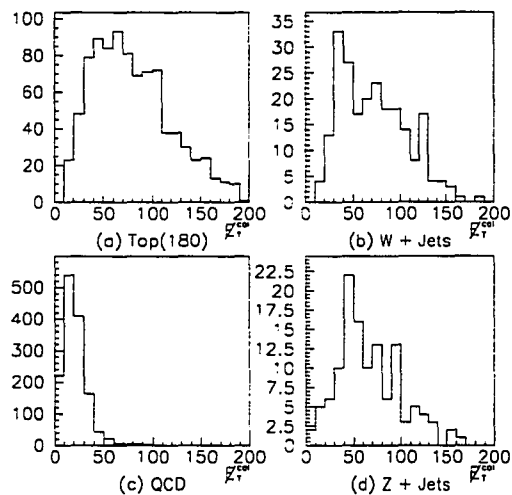


Figure 4.10: Distribution of E_T^{cal} (GeV) for Top(180) and its backgrounds. Normalization is arbitrary.

ordered by E_T , are remade with the added condition of $|\eta| \leq 2.0$ for every jet. Figure 4.12 shows distributions for the fourth highest E_T jet, E_T^{Jet4} , in an event for the signal and the backgrounds. The quantity E_T^{Jet4} is found to be worthy of being included in the list of variables that will separate the top quark signal from its backgrounds.

Another very useful quantity which models the massive decay signature of the $t\bar{t}$ system is simply the scalar sum of the transverse energies of all central jets. The H_T variable is such a measure and is defined to be:

$$H_T \equiv \sum_{i=1}^{N_{jets}} E_T^{jet(i)} \quad (4.2)$$

where the requirements for each jet to be included in the sum are:

- $E_T^{jet(i)} \geq 15$ GeV.
- $|\eta(jet(i))| \leq 2.0$.

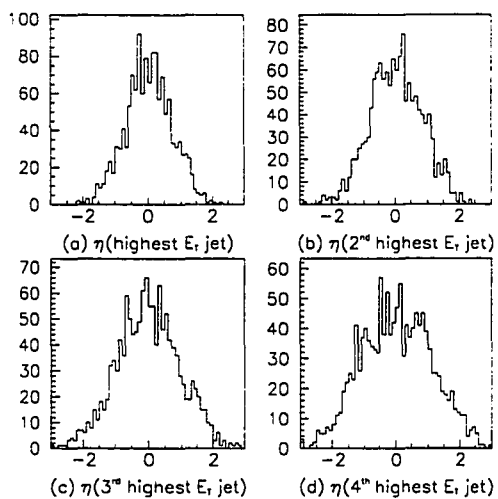


Figure 4.11: Distribution of η for four highest E_T jets in Top(180). Normalization is arbitrary.

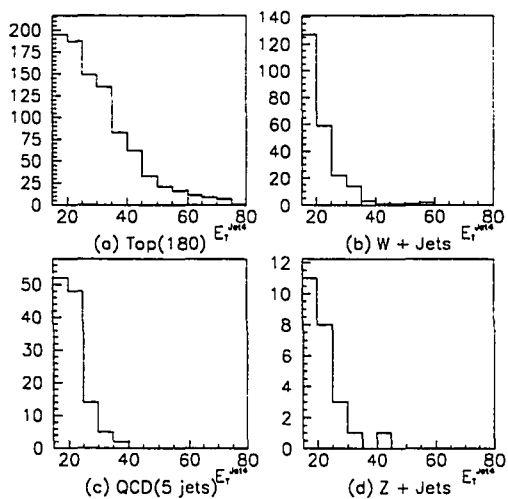


Figure 4.12: Distribution of E_T^{Jet4} (GeV) for Top(180) and its backgrounds. Normalization is arbitrary.

It is seen in Figure 4.13 that this variable is very useful in separating the top signal from its primary background, the $W + \text{jets}$, unlike the variables motivated by the leptonically decaying W boson. The distribution of the H_T variable for the signal is very dependent upon the mass of the top quark. This dependence is exploited in extracting a value for the top quark mass from the candidate signal events in the next chapter.

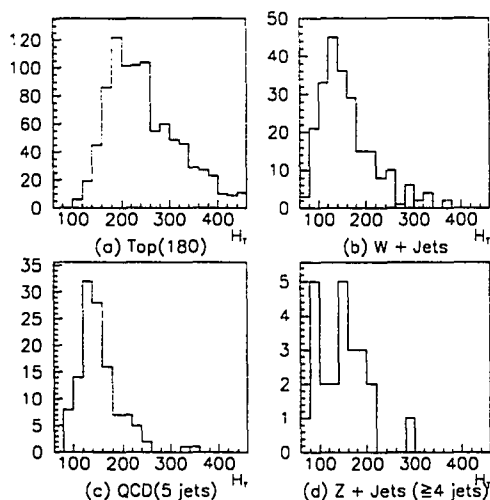


Figure 4.13: Distribution of $H_T(\text{GeV})$ for Top(180) and its backgrounds. The requirements for the $Z + \text{Jets}$ background has been tightened to ≥ 4 jets with $E_T^{\text{jet}} \geq 15$ GeV. Normalization is arbitrary.

The final quantity that will take advantage of the massive decay character will involve the spatial distribution of the jets in a scale invariant way. The variable to obtain a measure of this is the aplanarity, \mathcal{A} , and is calculated as follows.

1. Calculate the normalized momentum tensor M_{ab} :

$$M_{ab} = \frac{\sum_i p_{ia} p_{ib}}{\sum_i p_i^2} \quad (4.3)$$

- p_i is the 3-momentum of the i^{th} jet in the laboratory reference frame.

- a,b run over the x,y,z components.
2. Compute the eigenvalues Q_j and order them.
 - $Q_1 \leq Q_2 \leq Q_3$
 - $Q_1 + Q_2 + Q_3 = 1$
 - $Q_1 \geq 0$
 3. $\mathcal{A} = \frac{3}{2}Q_1$
 - Normalized to be in the range $0 \leq \mathcal{A} \leq 0.5$

To achieve a physical comprehension of the relation between the eigenvalues and the spatial distribution of the jets, note that:

- for spherical events, $Q_1 \approx Q_2 \approx Q_3$
- for planar events, $Q_1 \ll Q_2$
- for linear events, $Q_2 \ll Q_3$.

Figure 4.14 displays the \mathcal{A} distributions for the signal and its backgrounds. It is clear that this \mathcal{A} variable is not as powerful as the H_T , but it will nonetheless be used in the search for the optimal cut to discriminate the top quark signal from its backgrounds.

In summary, seven variables will initially be used in the optimization to extract a top quark signal from all its backgrounds. Four of these variables ($P_T(\mu)$, \cancel{E}_T , \cancel{E}_T^{min} , and \cancel{E}_T^{cal}) are related to the leptonically decaying W boson, while the remaining three variables (E_T^{Jet4} , H_T , and \mathcal{A}) exploit the massive decay nature of the $t\bar{t}$ system by looking at the jet debris in the events.

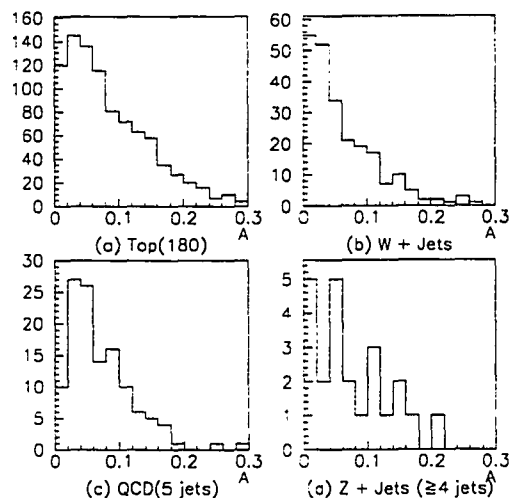


Figure 4.14: Distribution of \mathcal{A} for Top(180) and its backgrounds. The requirements for the Z + Jets background has been tightened to ≥ 4 jets with $E_T^{jet} \geq 15$ GeV. Normalization is arbitrary.

4.3 Calculation of the Number of Top and Background Events

In the search for the optimal cut values for the seven variables discussed in the previous section, an automated procedure will be required which calculates the expected number of signal and background events of each type. The method of calculation for the signal and each background for any particular set of cut values imposed is the subject of this section. The interpretation for the worth of any particular set of cut values as well as how it is used in deriving the optimal cut is the subject of the next section, the Grid Search.

The seven variables used to separate the signal from the backgrounds are:

- $P_T(\mu)$: P_T of the *isolated* μ with $|\eta| \leq 1.0$

- \cancel{E}_T : Missing transverse energy.
- \cancel{E}_T^{min} : Minimum missing transverse energy, regardless of the μ momentum value.
- \cancel{E}_T^{cal} : Missing transverse energy in the calorimeter. This is roughly equal to the P_T of the $W(\mu, \nu)$.
- E_T^{Jet4} : E_T of the fourth highest E_T jet in $|\eta| \leq 2.0$.
- H_T : Scalar sum of all transverse jet energies for jets with $|\eta| \leq 2.0$ and $E_T \geq 15$ GeV.
- \mathcal{A} : Aplanarity of all jets with $|\eta| \leq 2.0$ and $E_T \geq 15$ GeV.

4.3.1 Top Quark Events

The particular data sample used for the signal is top MC with a mass of 180 GeV/ c^2 generated by ISAJET.⁴⁶ The top MC is normalized by an order α_s^3 corrected cross section with a resummation of the leading soft gluon correction in all orders of perturbation theory.²⁷ Operationally, the calculation for the expected number of signal events passing any particular set of cuts is:

$$\langle n_s \rangle = \int \mathcal{L}_{data} dt \cdot \sigma_{Laenen}(m_{top} = 180 \text{ GeV}/c^2) \cdot \frac{\sum_{i=1}^{N_{Isajet(pass all cuts)}} \epsilon_i^{trig, reco}}{N_{Isajet(all)}} \quad (4.4)$$

where

- $\int \mathcal{L}_{data} dt = \int \mathcal{L}_{Ia} dt + \int \mathcal{L}_{Ib} dt = 9.8 \text{ pb}^{-1} + 35.8 \text{ pb}^{-1} = 45.6 \text{ pb}^{-1}$
- $\sigma_{Laenen}(m_{top} = 180 \text{ GeV}) = 4.21 \text{ pb}$
- $\frac{\sum_{i=1}^{N_{Isajet(pass all cuts)}} \epsilon_i^{trig, reco}}{N_{Isajet(all)}} = \text{fraction of Isajet top quark } (m_{top} = 180 \text{ GeV}/c^2) \text{ events passing cuts on all variables, weighted by the trigger and reconstruction efficiencies.}$

- $\epsilon^{trig,reco}$ represents the trigger and reconstruction efficiencies for events having only one isolated μ or having one isolated μ and an additional *nonisolated* μ . The values are calculated with an $\int \mathcal{L} dt$ weight for measurements in real data from runs Ia and Ib:

$$\epsilon^{trig,reco} = \frac{\int \mathcal{L}_{Ia} dt}{\int \mathcal{L}_{Ia} dt + \int \mathcal{L}_{Ib} dt} \cdot \epsilon_{Ia}^{trig} \cdot \epsilon_{Ia}^{reco} + \frac{\int \mathcal{L}_{Ib} dt}{\int \mathcal{L}_{Ia} dt + \int \mathcal{L}_{Ib} dt} \cdot \epsilon_{Ib}^{trig} \cdot \epsilon_{Ib}^{reco} \quad (4.5)$$

The trigger and reconstruction efficiencies for events with an isolated μ with and without an additional nonisolated μ are collected in Table 4.2.

Table 4.2: Trigger and reconstruction μ efficiencies.^{49–51}

$N(\text{isolated } \mu)$	$N(\text{nonisolated } \mu)$	ϵ_{Ia}^{trig}	ϵ_{Ia}^{reco}	ϵ_{Ib}^{trig}	ϵ_{Ib}^{reco}	$\epsilon^{trig,reco}$
1	0	0.67	0.95	0.67	0.85	0.58
1	1	0.74	0.90	0.74	0.80	0.61

4.3.2 W + Jets Background

The primary background, W + jets, is modeled by the VECBOS⁴⁷ MC and is normalized to the data *via* the jet scaling law:

$$N_4^{data} = \frac{N_3^{data}}{N_2^{data}} \cdot N_3^{data} \quad (4.6)$$

where N_i^{data} is the number of events with a $W(\mu, \nu) + i$ jets, inclusive. This normalization is derived from theoretical expectations⁴⁸ suggesting the ratio of number of events with W + n jets to number of events with W + ($n + 1$) jets to be roughly constant,

$$\alpha = \frac{W + (n + 1) \text{ jets}}{W + n \text{ jets}}. \quad (4.7)$$

Figure 4.15 illustrates the jets scaling law with real electron + jets data, $W(\rightarrow e + \nu) + \text{jets}$ VECBOS MC, and real QCD data. The validity of the law is estimated to be 20%.

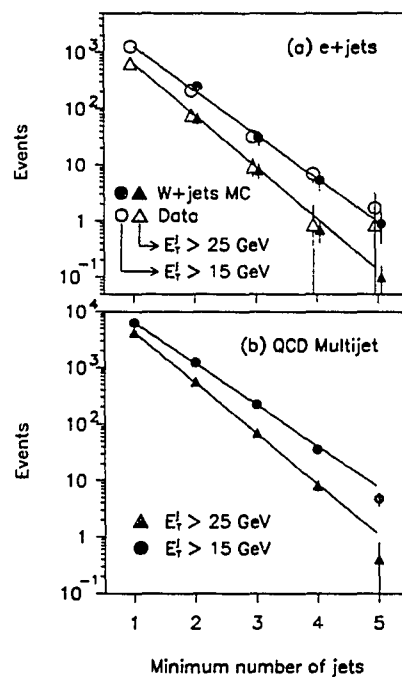


Figure 4.15: Jet multiplicity distribution in $W(\rightarrow e + \nu) + \text{jet}$ events for MC and real data in (a) and QCD real data events in (b).⁴²

The jet scaling law is used to normalize the $W(\rightarrow \mu + \text{jets})$ background by measuring N_2^{data} and N_3^{data} in real data through counting the number of events passing the following criteria:

- Pass the signal trigger (defined on pages 65 and 66)
- $P_T(\mu, \text{data}) \geq P_T(\mu, \text{CUT})$
- $\cancel{E}_T^{cal}(\text{data}) \geq \cancel{E}_T^{cal}(\text{CUT})$
- $\cancel{E}_T(\text{data}) \geq \cancel{E}_T(\text{CUT})$
- $\cancel{E}_T^{min}(\text{data}) \geq \cancel{E}_T^{min}(\text{CUT})$
- $E_T^{Jeti}(\text{data}) \geq E_T^{Jeti}(\text{CUT})$ for $i = 2$ or 3

where ‘‘CUT’’ indicates a cut value for the particular variable, while ‘‘data’’ refers to the value of the that variable for each data event.

The number of $W(\mu, \nu) + \text{jet}$ background events is then estimated to be:

$$\langle n_b^{W+\geq 4\text{jets}} \rangle = N_4^{\text{data}} \cdot \frac{N_{W+\text{jets}}^{\text{VECBOS}}(\text{pass all cuts})}{N_{W+\text{jets}}^{\text{VECBOS}}(\text{pass norm cuts})} \quad (4.8)$$

where $N_{W+\text{jets}}^{\text{VECBOS}}(\text{pass norm cuts})$ is the number of events in the W VECBOS sample that pass the same cuts imposed on the N_2^{data} and N_3^{data} events above, but with the jet requirement imposed on the fourth highest E_T jet, $E_T^{\text{Jet4}}(\text{data}) \geq E_T^{\text{Jet4}}(\text{CUT})$. $N_{W+\text{jets}}^{\text{VECBOS}}(\text{pass all cuts})$ is the number of events in the W VECBOS sample that pass cuts imposed on *all* seven variables.

4.3.3 QCD Background

The estimation for the QCD contamination will proceed with the use of the two real data samples explained on page 87, the $\text{QCD}(\mu^{\text{nonisol}})$ and $\text{QCD}(5 \text{ jets})$ data sets. The effect of the rejection on the variables $P_T(\mu)$, \cancel{E}_T , $\cancel{E}_T^{\text{min}}$, $\cancel{E}_T^{\text{cal}}$, and E_T^{Jet4} are determined from the $\text{QCD}(\mu^{\text{nonisol}})$ sample. The number of events passing cuts in these variables is denoted by $N_{\text{QCD}}^{\text{noniso}}$. Ideally, the $\text{QCD}(\mu^{\text{nonisol}})$ sample would come from the entire real data set with $\int \mathcal{L}_{\text{data}} dt = 45.6 \text{ pb}^{-1}$, however finite resources have limited this sample to a meager $\int \mathcal{L}(\text{QCD}(\mu^{\text{nonisol}})) dt = 5.8 \text{ pb}^{-1}$. (The lean size of $\int \mathcal{L}(\text{QCD}(\mu^{\text{nonisol}})) dt$ does not compromise the result, though, since the final QCD contribution at the optimal cut is estimated to be 0 ± 0.099 events.)

The necessity of the $\text{QCD}(5 \text{ jets})$ data set is due to the lack of statistics in the $\text{QCD}(\mu^{\text{nonisol}})$ sample. It provides further understanding of the rejection due to the remaining variables, H_T and \mathcal{A} . The total number of events in the $\text{QCD}(5 \text{ jets})$ data

set is designated by N_{QCD}^{jets} (no H_T, \mathcal{A} cuts). The subset of events that pass the H_T and \mathcal{A} cuts as well:

- $H_T(\text{data}) \geq H_T(\text{CUT})$
- $\mathcal{A}(\text{data}) \geq \mathcal{A}(\text{CUT})$

is denoted by N_{QCD}^{jets} (pass H_T, \mathcal{A} cuts).

The probability for a *nonisolated* muon to appear as an isolated muon, P_{fake}^μ , is calculated by studying $b\bar{b}$ favored real data events and measuring the rate of muons passing the isolation criteria. P_{fake}^μ is determined to be 0.06 ± 0.02 over a robust range in \cancel{E}_T .^{49,50}

Gathering the information from the two real data sets and the fake rate, P_{fake}^μ , the calculation for the expected number of QCD background events is:

$$\langle n_b^{QCD} \rangle = N_{QCD}^{noniso} \cdot \frac{\int \mathcal{L}_{data} dt}{\int \mathcal{L}(QCD(\mu^{nonisol})) dt} \cdot \frac{N_{QCD}^{jets}(\text{pass } H_T, \mathcal{A} \text{ cuts})}{N_{QCD}^{jets}(\text{no } H_T, \mathcal{A} \text{ cuts})} \cdot P_{fake}^\mu. \quad (4.9)$$

4.3.4 Z + Jets Background

The calculation for the Z + jets contribution uses the Z VECBOS⁴⁷ MC which is then scaled by the real data to the number of events satisfying the following criteria:

- Pass the signal trigger (defined on pages 65 and 66)
- 2 isolated muons satisfying $P_T(\mu, \text{data}) \geq P_T(\mu, \text{CUT})$
- $\cancel{E}_T^{min}(\text{data}) \geq \cancel{E}_T^{min}(\text{CUT})$
- $\cancel{E}_T^{cal}(\text{data}) \geq \cancel{E}_T^{cal}(\text{CUT})$
- $E_T^{Jet3}(\text{data}) \geq E_T^{Jet4}(\text{CUT})$

The above cuts are imposed on the real data ($\int \mathcal{L}_{data} dt = 45.6 \text{ pb}^{-1}$) and VECBOS samples. The number of real data events satisfying the above cuts is denoted by N_{Z+jets}^{data} , while those of VECBOS passing is $N_{Z+jets}^{VECBOS}(\text{pass norm cuts})$. The number of VECBOS events satisfying the cuts on all variables is represented by $N_{Z+jets}^{VECBOS}(\text{pass all cuts})$. The estimated number of $Z(\mu^+, \mu^-) + \geq 4$ jets background events is calculated to be:

$$\langle n_b^{Z+jets} \rangle = N_{Z+jets}^{data} \cdot \frac{N_{Z+jets}^{VECBOS}(\text{pass all cuts})}{N_{Z+jets}^{VECBOS}(\text{pass norm cuts})}. \quad (4.10)$$

Recall that the calculation for \cancel{E}_T^{min} uses the direction and magnitude of \cancel{E}_T^{cal} and the direction of only the highest p_T muon. So, in events with two isolated high p_T muons, \cancel{E}_T^{min} becomes an estimate for the minimal p_T of the second highest p_T muon based on \cancel{E}_T^{cal} and $p_T(\mu, \text{highest})$.

The error on the estimated number of events for each background ($\sigma_b^{W+\geq 4jets}$, σ_b^{QCD} , and σ_b^{Z+jets}) through equations 4.8, 4.9, and 4.10 is calculated using common error propagation techniques taking into account both the statistical and systematic errors for the real data and MC samples. For each background, the systematic uncertainties in the jet energy scale in both the real data and MC are taken into account. The $\sigma_b^{W+\geq 4jets}$ calculation has an additional 20% error in assuming the validity of the jet scaling law⁴² of Equation 4.6.

4.4 Derivation of Optimal Selection Cuts (Grid Search)

The previous section discussed the calculation for the expected number of signal ($\langle n_s \rangle$) and background ($\langle n_b^i \rangle$) events of each type. The present discussion* will address the question of how one optimizes the cut values after automated calculations for $\langle n_s \rangle$ and the $\langle n_b^i \rangle$'s exist. This will be followed up in the next section with the application of the optimal cut to the real data sample where excess events for the signal will prevail.

The goal of an optimal cut is to maximize the difference in the expected outcomes for the two hypotheses, one where the sought-after signal exists and the other where there is only background. Maximizing the difference is equivalent to minimizing the similarity in the anticipated results. The strategy for deriving the optimal cut values will be to quantify the similarity of the predicted outcomes with a probability and minimizing it. A general discussion of the Grid Search will first be presented followed by its application to the search for the top quark in the $\mu +$ jets channel in the succeeding subsection.

4.4.1 General Discussion

For each variable x_i , a range and granularity is selected to be used in the automated search. Then, a systematic step through all the possible combinations of cut values is done while recording the particular values for each variable which minimize the probability for the expected number of background events ($\langle n_b \rangle$), with

*For a more general discussion of the Grid Search, see [52].

its uncertainty (σ_b), to exceed the sum of the expected number of background ($\langle n_b \rangle$) and signal ($\langle n_s \rangle$) events. Quantitatively, this probability is⁵³:

$$P(\langle n_b \rangle \pm \sigma_b \rightarrow \langle n_b \rangle + \langle n_s \rangle) = \int_0^\infty dn_b \frac{1}{\sqrt{2\pi}\sigma_b} \cdot \exp^{-\frac{(n_b - \langle n_b \rangle)^2}{2\sigma_b^2}} \left\{ \sum_{N'_{TOT}=0}^\infty \frac{\exp^{-(n_b + \langle n_s \rangle)} (n_b + \langle n_s \rangle)^{N'_{TOT}}}{N'_{TOT}!} \left[\sum_{n'_b=N'_{TOT}}^\infty \frac{\exp^{-(n_b)} (n_b)^{n'_b}}{n'_b!} \right] \right\} \quad (4.11)$$

where

$$\langle n_b \rangle = \sum_j \langle n_b^j \rangle \quad (4.12)$$

and

$$\sigma_b = \sqrt{\sum_j (\sigma_b^j)^2}. \quad (4.13)$$

(The calculation for the error in the backgrounds by Equation 4.13 can, in principle, be modified to accommodate common systematic errors.) The quantity in the square brackets in Equation 4.11 is the probability for n_b background events to fluctuate above N'_{TOT} signal and background events. N'_{TOT} is not a measured quantity, but rather is only an expectation that is subject to Poisson statistics. Hence, the term on the second line incorporates this information. The uncertainty in the calculated number of background events, σ_b , is implemented through a Gaussian approximation. In principle, there should also be a term for the uncertainty in the expectation for the number of signal events. However, in the task of discovering a new particle with no measured cross section, assigning an error to $\langle n_s \rangle$ is somewhat arbitrary and it is decided to not incorporate such information.

4.4.2 Application to $t\bar{t} \rightarrow \mu + \text{Jet}$ Events

The values of each variable that are tested in the optimization procedure are given in Table 4.3. The resulting optimal cut values are shown in Table 4.4 and it is seen that the \mathcal{A} variable is not needed for the optimal cut. (It is interesting to note that identical optimal cut values are obtained when the signal is top with mass 160 GeV/c².) The efficiencies of the optimal cut and MC reconstruction for top of several mass values are gathered in Table 4.5, along with the effects of more lenient cuts. The expected yield of signal events for various top quark masses as well as the backgrounds are summarized in Table 4.6. (Note that there is a dependence of the optimal cuts and its worthiness on the $\int \mathcal{L} dt$; see Appendix C.)

Table 4.3: Range and granularity for each quantity in the Grid Search.

Quantity	Minimum Value	Step Size	Number of Steps
$P_T(\mu)$	15 GeV/c	5 GeV/c	5
\cancel{E}_T^{cal}	15 GeV	5 GeV	10
\cancel{E}_T	15 GeV	5 GeV	5
\cancel{E}_T^{min}	15 GeV	5 GeV	5
E_T^{Jet4}	15 GeV	5 GeV	5
H_T	100 GeV	10 GeV	16
\mathcal{A}	0.00	0.01	11

Table 4.4: Optimal cut values resulting from the Grid Search.

Quantity	Optimal Cut Value
$P_T(\mu)$	15 GeV/c
\cancel{E}_T^{cal}	50 GeV
\cancel{E}_T	15 GeV
\cancel{E}_T^{min}	15 GeV
E_T^{Jet4}	15 GeV
H_T	160 GeV
\mathcal{A}	0.00

Table 4.5: Cut efficiencies for top events within the $t\bar{t} \rightarrow \mu + \text{jet}$ decay channel. The efficiencies in Table 4.2 are not included here, although that of the MC reconstruction is taken into account. The ϵ^{reco} in Table 4.2 is a *relative* correction of real data with respect to MC.

Loose Cut: Minimal cuts in grid search (Table 4.3) modified with $H_T \geq 0$.

Min Grid Cut: Minimal cuts in grid search in Table 4.3.

Optimal Cut: Optimized cuts in Table 4.4.

$m_{\text{top}}(\text{GeV}/c^2)$	$\epsilon(\text{loose cut})$	$\epsilon(\text{min grid cut})$	$\epsilon(\text{optimal cut})$
140	0.134	0.133	0.063
160	0.144	0.142	0.090
180	0.171	0.171	0.121
200	0.175	0.175	0.136

Table 4.6: Expected number of signal and background events passing optimal cuts.

Event Type	Expected Number of Events
Top($m_{\text{top}} = 140 \text{ GeV}/c^2$)	4.19
Top($m_{\text{top}} = 160 \text{ GeV}/c^2$)	2.92
Top($m_{\text{top}} = 180 \text{ GeV}/c^2$)	2.02
Top($m_{\text{top}} = 200 \text{ GeV}/c^2$)	1.22
All Backgrounds	1.40 ± 0.71
W + Jets Background	1.13 ± 0.62
QCD Background	0.00 ± 0.10
Z + Jets Background	0.27 ± 0.33

A feel for the dynamics in the cut values can be achieved in any pair of the variables through use of a cumulative lego plot. Figure 4.16 demonstrates this conceptual vehicle with the interaction between the H_T and $\cancel{E}_T^{\text{cal}}$ variables. The height of each tower in Figure 4.16(a) corresponds to the probability defined in Equation 4.11 for a cut represented by the corner of the bin with the smallest values. Cut values of the other variables were at their optimal. (See Appendix D for the optimization probability dependence in all other possible pairs of variables.)

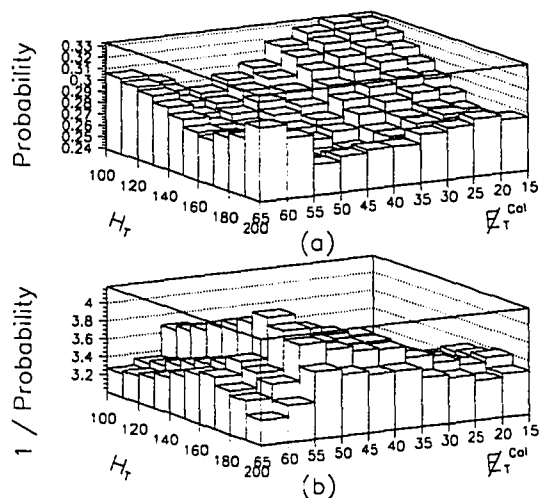


Figure 4.16: Cumulative probability lego plots in H_T (GeV) and E_T^{cal} (GeV).
 (a) Probability defined in Equation 4.11.
 (b) Reciprocal of the probability is plotted to visualize the optimal location which is hidden in the probability plot.

The E_T^{cal} variable and its cut value are much different from previous searches for the top quark^{1,2} which warrant a little more discussion. First of all, Figure 4.16 does illustrate a well behaved nature for the predictive power of E_T^{cal} (as well as for H_T). Secondly, the jet scaling law is seen to be respected for E_T^{cal} as demonstrated in Figure 4.17(a) which shows that α (defined in Equation 4.7) is constant over a large range in cut values of E_T^{cal} . The predicted number of events for $W + 4$ or more jets, via the scaling law of Equation 4.6, agrees very well with that observed, as shown in Figure 4.17(b). The agreement is good independent of the E_T^{cal} cut. The slight observed excess is consistent with a small content of top quark events. The values used to scale the W VECBOS MC events are those predicted by the scaling law.

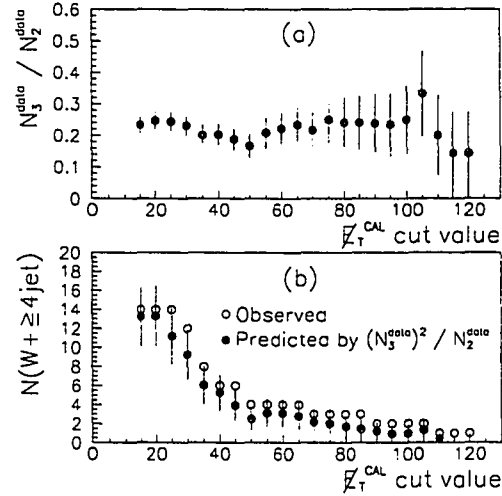


Figure 4.17: Consistency check of the jet scaling assumption. Optimal cuts are applied to the $P_T(\mu)$, E_T^{jet} , and E_T^{min} variables. The jet E_T cuts are $E_T^{\text{Jet 2 or Jet 3 or Jet 4}} \geq 15$ GeV. There are no cuts on any other variable. E_T^{CAL} cut values are in GeV.

(a) Demonstration that $\frac{N_3^{\text{data}}}{N_2^{\text{data}}} \propto \alpha_S$ is roughly constant as expected from the jet scaling law.

(b) Comparison between predicted number of $W + \geq 4$ jet events from Equation 4.6 and that observed. The predicted values are used to normalize the $W + \geq 4$ jet background estimation.

4.5 Application of Optimal Cuts to Data

The discussion now turns to the result of applying the optimal cuts shown in Table 4.4 to the real data. Any excess over the expected number of background events will be interpreted as a signal for top quark production and a significance calculation will be performed to determine the probability that the expected number of background events ($\langle n_b \rangle$) with its error ($\langle \sigma_b \rangle$) is consistent with the observed number of events (N_{obs}). An event excess will also provide the means for a cross section calculation for $t\bar{t}$ production as a function of the top quark mass.

The application of the optimal cuts in Table 4.4 yields four candidate events. Table 4.7 lists the values of the seven variables for each of the candidate events, while Appendix E contains the four-vectors of all objects in the events. Figures 4.18 and 4.19 show distributions of H_T , \cancel{E}_T^{cal} , \cancel{E}_T^{min} , and \mathcal{A} for real data events passing the loose cuts defined in the caption of Table 4.5. It seems rather unlikely that the backgrounds alone ($\langle n_b \rangle = 1.40 \pm 0.71$ from Table 4.6) can accommodate the number of observed events ($N_{obs} = 4$). However, the presence of a top quark signal ($\sim 2-3$ events) along with the background is consistent with the observed number of events. Quantitatively, a Poisson probability can be calculated to determine the chances of $\langle n_b \rangle \pm \sigma_b$ events equaling or exceeding N_{obs} events:

$$P(\langle n_b \rangle \pm \sigma_b \rightarrow N_{obs}/more) = \int_0^\infty dn_b \frac{1}{\sqrt{2\pi}\sigma_b} \exp\left(-\frac{(n_b - \langle n_b \rangle)^2}{2\sigma_b^2}\right) \cdot \left[\sum_{n'_b=N_{obs}}^\infty \frac{\exp^{-\langle n_b \rangle} \langle n_b \rangle^{n'_b}}{n'_b!} \right]. \quad (4.14)$$

The calculation yields:

$$P(1.40 \pm 0.71 \rightarrow 4/more) = 0.0814 \quad (4.15)$$

which, in the gaussian approximation, is a 1.7σ effect.

Table 4.7: Values of variables for candidate events.

Quantity	Run 58192 Event 137	Run 58203 Event 4980	Run 63183 Event 13926	Run 82694 Event 25595
$P_T(\mu)$ (GeV/c)	75.7	79.5	57.6	53.5
\cancel{E}_T^{cal} (GeV)	138.9	109.9	89.7	69.3
\cancel{E}_T (GeV)	70.5	122.0	57.7	42.9
\cancel{E}_T^{min} (GeV)	41.7	19.4	56.4	42.9
E_T^{Jet4} (GeV)	35.5	18.4	30.6	29.1
H_T (GeV)	246.7	200.2	195.4	247.3
\mathcal{A}	0.049	0.056	0.006	0.128

An m_{top} dependent cross section, $\sigma(m_{top})$, for the excess observed events can be calculated using the following formula:

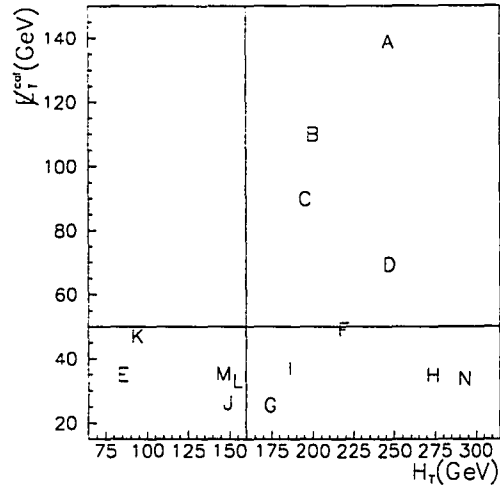


Figure 4.18: \cancel{E}_T^{cal} vs. H_T for real data passing the loose cuts defined in the caption of Table 4.5. The horizontal and vertical lines represent the boundaries of the optimal cuts, shown in Table 4.4, on \cancel{E}_T^{cal} and H_T , respectively. Events A, B, C, and D are the four candidates.

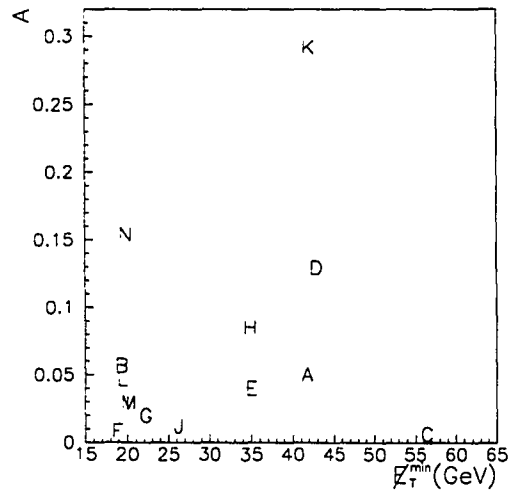


Figure 4.19: \mathcal{A} vs. \cancel{E}_T^{min} for real data passing the loose cuts defined in the caption of Table 4.5. Events A, B, C, and D are the four candidates.

$$\sigma(m_{top}) = \frac{N_{obs} - n_b}{\epsilon(m_{top}) \cdot Br \cdot [\int \mathcal{L} dt]} \quad (4.16)$$

where $\epsilon(m_{top})$ is the overall efficiency of $t\bar{t} \rightarrow \mu + \text{jet}$ events passing the signal trigger, being successfully reconstructed, and satisfying the optimal selection criteria. The Br is the 4/27 branching fraction of all top quark events that decay into the $\mu + \text{jets}$ channel. Numerical results of such a computation are summarized in Table 4.8. The systematic error takes into account uncertainties from the following sources:

1. The $\int \mathcal{L} dt$ estimated to be 12 % (5.5 pb^{-1}).⁴⁵
2. The jet energy scale.^{39,40}
 - Monte Carlo: $\approx 5\text{--}6$ %.
 - Real Data: $\approx 3\text{--}4$ %.
3. The validity of the jet scaling law used to normalize the $W + \text{jet}$ background, estimated at 20%.⁴²

It is seen that the dominant error is due to the small statistics of four candidate events. Combining the statistical and systematic errors in quadrature, Figure 4.20 illustrates the measured cross section for the excess events as a function of m_{top} .

Table 4.8: Cross Section values of excess events for different top quark masses.

m_{top} (GeV/ c^2)	$\hat{\sigma} \pm \Delta\sigma(stat.) \pm \Delta\sigma(syst.)$ (pb)
140	$10.5 \pm 8.5 \pm_{-2.9}^{+2.5}$
160	$7.3 \pm 5.9 \pm_{-1.7}^{+1.4}$
180	$5.4 \pm 4.4 \pm_{-1.2}^{+1.0}$
200	$4.8 \pm 3.9 \pm_{-1.1}^{+0.8}$

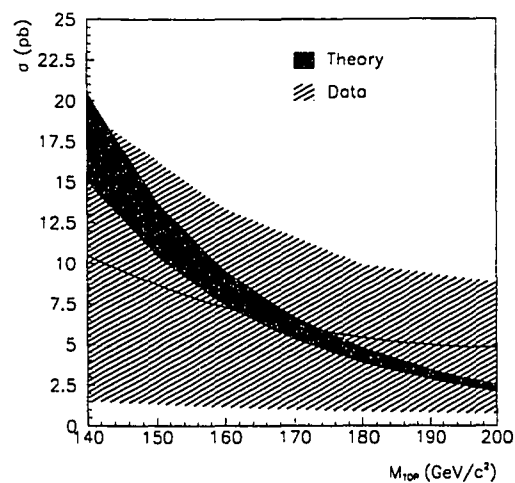


Figure 4.20: Cross section of excess events as a function of top quark mass. The central value of the cross section and its one standard deviation error are shown by the solid line and the borders of the lighter band. The theoretical estimate²⁷ for $t\bar{t}$ production is shown by the darker band.

Chapter 5

Top Quark Mass Analysis

The search for the top quark in the $\mu + \text{jets}$ channel yields four candidate events which is an excess over the expected background of 1.40 ± 0.71 . The assumption that this excess is the result of $t\bar{t}$ production allows for a calculation of the top quark mass which is presented in this chapter.

The H_T dependence on the top quark mass will be exploited in extracting the mass value. The use of such a global variable avoids the necessity of dealing with the jet combinatorics in the currently practiced kinematic fitting algorithms.^{1,2} The major advantage of using a method which bypasses the jet combinatoric problem is the reduction in the largest systematic error, that due to the uncertainty in the jet energy correction back to the parton. Consider a typical top event where a highly energetic b quark radiates a gluon of sufficient energy to create another jet far away in $\eta - \phi$ space as shown in Figure 5.1. The combinatoric dependent kinematic fitting method suffers from the inability to determine the b quark energy before the radiation occurred. However, use of H_T doesn't require such a mapping between the jet and parton energies. The effect of the radiated jet is taken into account in the H_T value if the radiated jet has $E_T \geq 15$ GeV and $|\eta| \leq 2.0$.

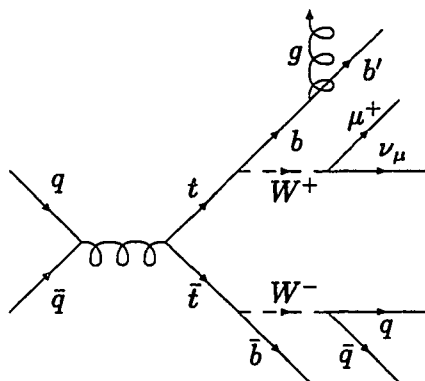


Figure 5.1: Feynman diagram of gluon radiation within the $t\bar{t}$ system.

5.1 Explanation of the Technique and Its Error

The method of parameterizing the H_T dependence on the top quark mass is first discussed and followed by a description of the mass extraction technique.

5.1.1 Parameterization of H_T

The parameterization process is a very straightforward one. The MC events generated using a particular top quark mass and passing the cuts in Table 4.4 are used to generate a probability density function in the H_T variable. The form of the function that is used to characterize the distribution is a double gaussian (sum of 2 gaussian functions). Probability density functions are generated from top events for masses 140, 160, 180, and 200 GeV/ c^2 . H_T distributions for the four top quark samples are shown in Figure 5.2. (Note that the H_T values in Figure 5.2 go below the $H_T = 160$ GeV cut to assist the parameterization.)

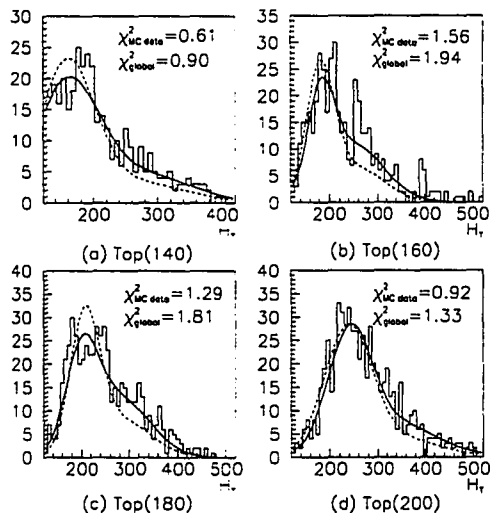


Figure 5.2: H_T (GeV) of top events for masses 140, 160, 180, and 200 GeV/c².

The solid curves are the best fits to the MC event sample; the dashed are (scaled) globally fit probability density functions (as shown in Figure 5.4) evaluated at the appropriate mass values. The χ^2 values are per degree of freedom.

Extracting the top quark mass dependent behavior of the H_T probability density function is accomplished by fitting each parameter of the double gaussian fit to a function of m_{top} . For example, Figure 5.3(a) shows an exponential fit to the mean of the left gaussian. (The left gaussian is near the peak, the right is in the tail.) The double gaussian has six parameters to be fit. However, the normalization takes care of the absolute values of the heights, so only the ratio of the heights of the two gaussians is relevant.

The results of the fits in Figure 5.3 provide the values of the double gaussian parameters for the desired top mass dependent H_T probability density functions. Samples of these curves for various top masses are shown in Figure 5.4 along with the background. The significant sources of background which survive the optimal

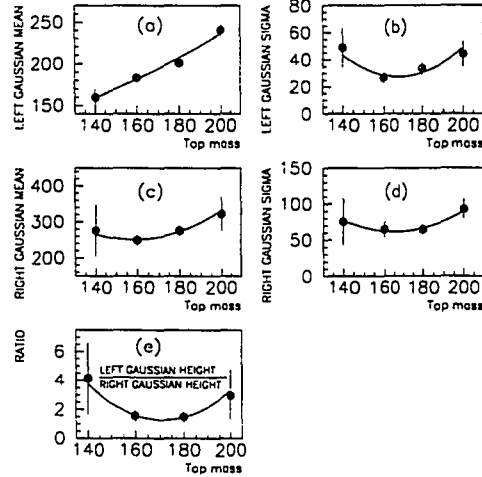


Figure 5.3: Fit of the double gaussian parameters for the top mass dependence. The functional forms used are an exponential in (a) and a quadratic in (b)-(e). Units for both axes in all windows are GeV/c², except for the vertical in (e) which is dimensionless.

cuts are the $W + \text{jet}$ (1.13 ± 0.62) and $Z + \text{jet}$ (0.27 ± 0.33) processes, as shown in Table 4.6. Both backgrounds are expected to have identical H_T behavior; the $W + \text{jet}$ VECBOS sample is used to model the H_T dependence for all backgrounds.

5.1.2 Mass Extraction Procedure

The mass extraction procedure uses a likelihood function analogous to that currently being used at both DØ and CDF. This likelihood function is defined with a gaussian constraint on the expected number of background events ($\langle n_b \rangle \pm \sigma_b$), a Poisson weight for the total number of observed events (N_{obs}) to have come from the sum of the best fit number of background and signal events ($n_b + n_s$), and a weighted mixture of background and signal using the probability density functions

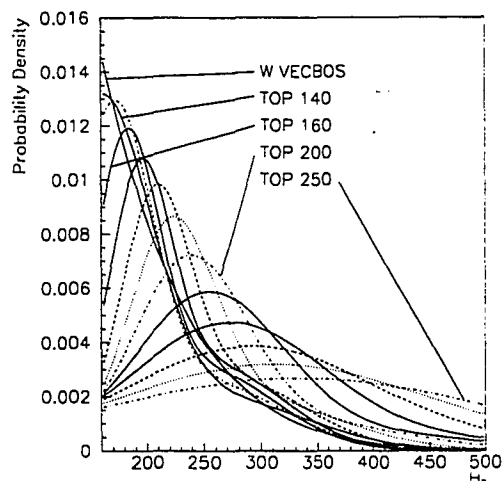


Figure 5.4: H_T (GeV) probability density curves for background and top of several mass values. The H_T curves are in 10 GeV/c^2 increments of top mass.

(f_b and f_s) in the variable that is sensitive to the top mass, H_T in this case. The likelihood function is:

$$L = \frac{1}{\sqrt{2\pi}\sigma_b} \exp\left[-\frac{(n_b - \langle n_b \rangle)^2}{2\sigma_b^2}\right] \cdot \frac{\exp^{-(n_s + n_b)} \cdot (n_s + n_b)^{N_{obs}}}{N_{obs}!} \cdot \prod_{i=1}^{N_{obs}} \frac{n_b f_b(H_T(i)) + n_s f_s(H_T(i), M_{top})}{(n_s + n_b)} \quad (5.1)$$

where n_s , n_b , and M_{top} are the fitted parameters which maximize the likelihood. The only difference between what has been published by DØ¹ and CDF² and the analysis here is the replacement of the “fitted mass functions” with the H_T functions.

5.2 Application To Data

The top mass extraction procedure is applied to the four candidate events, resulting in a most likely value with an associated statistical error. Calculations follow for the systematic errors due to the mass extraction procedure, the uncertainty in the jet energy scale, and the uncertainty due to the top MC generator. The best value and its various errors are then combined into the final result for the top quark mass.

5.2.1 Best Fit Top Mass Value and Its Statistical Error

The likelihood function, defined in equation (5.1), is maximized with the four data candidate events having H_T values listed in Table 5.1. The plots in Figure 5.5 show the behavior of the likelihood function, as well as the best fit number of background and signal events, as a function of different top mass hypotheses. The statistical error is determined by the range of hypotheses in top mass values that increase the $-\log(\text{likelihood})$ value by 0.5 from its optimal fit. The resultant best fit mass and its statistical error can be derived from Figure 5.5(b) and are:

$$M_{Top} = 185^{+16}_{-26}(\text{stat.}) \text{ GeV}/c^2. \quad (5.2)$$

Table 5.1: H_T values of candidate events.

H_T (GeV)	195	200	247	247
-------------	-----	-----	-----	-----

If the statistical error above is compared to the RMS values of m_{top}^{fit} from the four sets of 1000 simulated experiments as gathered in Table 5.2, it appears that

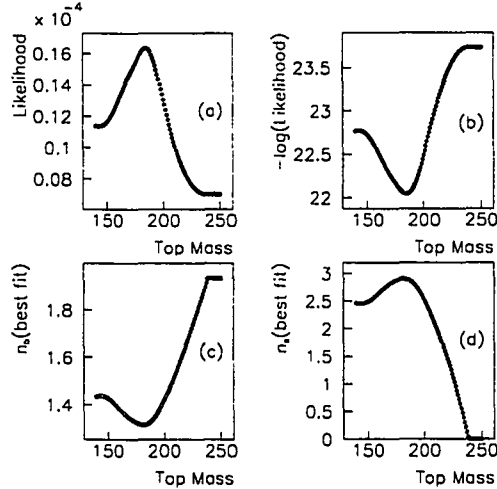


Figure 5.5: Result of fit for candidate events to the mass likelihood function. (a) Likelihood value. (b) $-\text{Log}(\text{likelihood})$. (c) Number of background events in best fit. (d) Number of signal events in best fit.

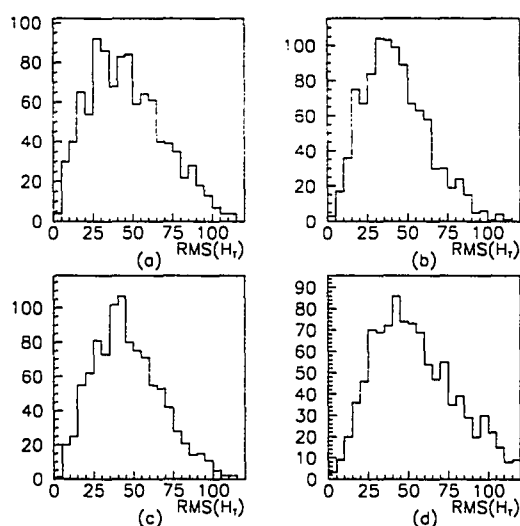
the observed error is smaller than expected. However, if the width of the observed H_T values is taken into consideration, the statistical error is seen to be very representative of what is anticipated. The RMS of the observed H_T values, as listed in Table 5.1, is 25 GeV. Comparison of this value to the simulated experiments, shown in Figure 5.6, illustrates that although the observed $\text{RMS}(H_T)$ value is smaller than expected, it is still a typical outcome. Recalculated $\text{RMS}(m_{top}^{fit})$ values for outcomes in the proximity of the observed, $15 \leq \text{RMS}(H_T) \leq 35$ GeV, are comparable to the observed statistical error, as collected in Table 5.2.

5.2.2 Error Attributed to the Method

The estimate for the systematic error due to the method is derived from the difference between the input top quark mass and the most probable outcome de-

Table 5.2: RMS of m_{top}^{fit} for simulated experiments. All entries are in GeV.

Input Top Mass	RMS(m_{top}^{fit})	RMS(m_{top}^{fit}) for $15 \leq \text{RMS}(H_T) \leq 35$
140	28	19
160	26	19
180	27	20
200	28	19

Figure 5.6: RMS(H_T)(GeV) for simulated experiments generated with top mass of (a) 140 GeV/ c^2 , (b) 160 GeV/ c^2 , (c) 180 GeV/ c^2 , and (d) 200 GeV/ c^2 .

terminated by many simulated experiments having a large number of signal and background events in a mixture commensurate with that observed. One thousand experiments are generated with 65 signal events and 35 background events. The H_T value for each signal event is randomly generated using the appropriate fitted solid curve in Figure 5.2; the background events use the W VECBOS curve in Figure 5.4. In the evaluation of the likelihood function, $\langle n_b \rangle$ and σ_b are set to 35 and 0.1, respectively. Each simulated experiment is required to be sensitive enough to retrieve the mass information by demanding a reduction in the likelihood value,

L, by at least $e^{-0.5}$ of its maximum (one standard deviation error) for top mass values away from its best fit. Results of the simulated experiments generated with three different m_{top} values are shown in Figure 5.7. (The $H_T \geq 160$ GeV cut gives rise to pathologic results for simulations produced with $m_{top} = 140$ GeV. This is so because the cut causes the mean values of the evaluating global H_T curves in Figure 5.4 to *increase* as m_{top} *decreases* below 150 GeV/c². Lowering the H_T cut would lower the m_{top} pathologic border. As this analysis concerns itself only in the region around the $m_{top} = 185$ GeV/c² observed, this behavior has no effect on the result.)

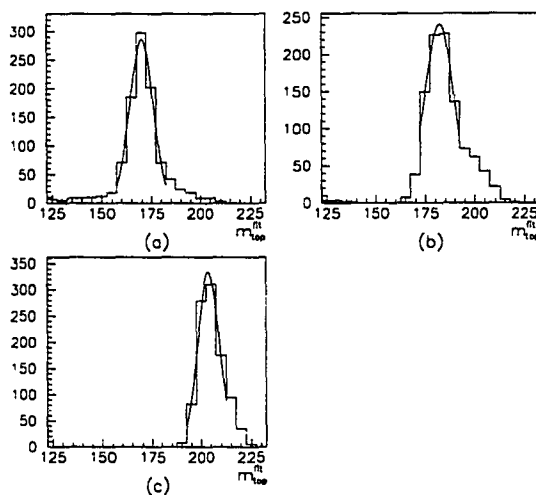


Figure 5.7: Top mass of best fit to the likelihood function for 1000 simulated experiments and samples of fits for the most probable m_{top} values. The input top masses are 160(a), 180(b), and 200(c) GeV/c².

The calculation for the most likely value proceeds by fitting the bins at the maxima to a gaussian function, as in Figure 5.7(a), and attributing the mean of the gaussian as a contributor to the estimate of the most probable outcome. To minimize any effect introduced by a particular choice of binning, the same fitting

procedure is repeated four more times with bins offset by one GeV/c^2 from the previous iteration and the average of the five gaussian means is then the estimate for the most probable outcome. The results of such an operation on the experiments generated with the three m_{top} values are entered in Table 5.3. (See Appendix F for fit results for all offsets.)

Table 5.3: Most probable m_{top} from the simulated experiments and the resulting estimated systematic error due to the method. All entries are in GeV/c^2 .

Input m_{top}	Most Probable m_{top}	Error in m_{top}
160	170	+10
180	182	+2
200	203	+3
$\sigma_{M_{top}}^{\text{method}}$		± 3

Since the data gives $m_{top} = 185 \text{ GeV}/c^2$, the error due to the likelihood procedure in extracting a mass value for the top quark will be determined by the largest discrepancy between the most probable outcome and the input mass value among the experiments generated with $m_{top} = 180 \text{ GeV}/c^2$ and $m_{top} = 200 \text{ GeV}/c^2$. The results gathered in Table 5.3 show that the simulations produced with $m_{top} = 200 \text{ GeV}/c^2$ give the larger disparity. So, the assessed error due to the method will be:

$$\sigma_{M_{top}}^{\text{method}} = \pm 3 \text{ GeV}/c^2. \quad (5.3)$$

5.2.3 Error Due to Uncertainty of Jet Energy Scale

The systematic error due to the uncertainty of the jet energy scale is determined by repeating the likelihood fits for the four candidates with the jet energies modified by one standard deviation in the data and MC separately, as is done for the cross section calculation in Section 4.5. The error is then calculated assuming

independence in the lack of knowledge of the energy scale between data and MC. This assumption of independence between data and MC is warranted, since much of the uncertainty in the jet energy corrections for data involve issues not considered in the MC case.⁴⁰ For example, two items are:

- The actual selection cuts on the real data samples which the energy correction studies are based upon.
- The uncertainty in the transverse momenta, K_T , of the quarks in the $\bar{p}p$ beam.

The departures of the minima from 185 GeV/c² in the plots of Figure 5.8 provide the errors due to the particular jet energy modifications. Quantitative results of Figure 5.8 are collected in Table 5.4. The total error due to the uncertainty in the jet energy scale is:

$$\sigma_{M_{top}}^{\text{energy scale}} = {}_{-7}^{+5} \text{ GeV}/c^2 \quad (5.4)$$

where errors with the same sign were added in quadrature.

Table 5.4: Effect on best fit top mass result from modifications to jet energy responses on MC H_T probability curves and data candidate events. All entries are in GeV/c².

	Jet Energy Correction	
	Low	High
Applied to MC	+3	-5
Applied to Data	-5	+4

5.2.4 Error Due to Uncertainty in Top Quark MC Generator

To estimate the uncertainty the top MC generator introduces into the value of the top quark mass, the entire mass extraction procedure is repeated with top

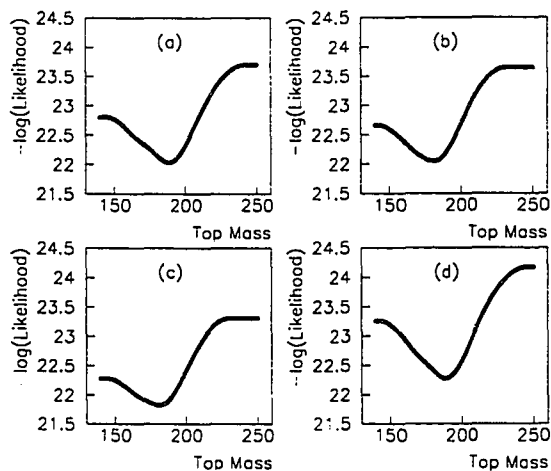


Figure 5.8: Effect of jet energy scale uncertainty on top quark mass result. Likelihood fits for: (a) MC jet energies lowered, (b) MC jet energies raised, (c) DATA jet energies lowered, and (d) DATA jet energies raised.

events produced with the HERWIG⁴³ MC. (Recall that ISAJET⁴⁶ is the default MC used for the top quark signal.) The H_T distributions for the HERWIG MC are shown in Figure 5.9. This can be compared to the default ISAJET distributions in Figure 5.2. The final result obtained by completing the mass analysis with the HERWIG top events are displayed in Figure 5.10 where the ISAJET version is Figure 5.5. Figure 5.10(a) shows a hint of an unexpected secondary peak in the likelihood near 140 GeV/c². However, if the attention is restricted to the region around the globally optimal value, the peak of the likelihood function occurs at ≈ 184 GeV/c². So, the error that will be assigned to the uncertainty of the MC modeling the top signal is:

$$\sigma_{M_{top}}^{top MC} = \pm 1 \text{ GeV}/c^2. \quad (5.5)$$

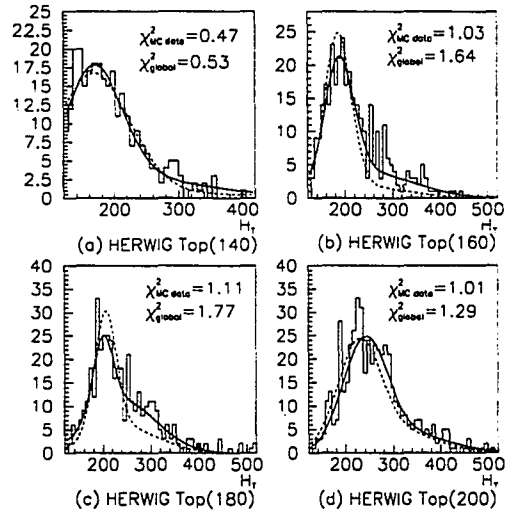


Figure 5.9: H_T of HERWIG MC top events for masses 140, 160, 180, and 200 GeV/c^2 . The solid curves are the best fits to the MC data; the dashed are (scaled) globally fit probability density functions (HERWIG version of those shown in Figure 5.4) evaluated at the appropriate mass values. The χ^2 values are per degree of freedom.

5.2.5 Top Quark Mass Result

Summarizing the best fit mass results and the errors from equations (5.2), (5.3), (5.4), and (5.5) provides the final result:

$$M_{top} = 185^{+16}_{-26}(\text{stat.})^{+6}_{-8}(\text{syst.}) \text{ GeV}/c^2$$

where the systematic errors were combined in quadrature.

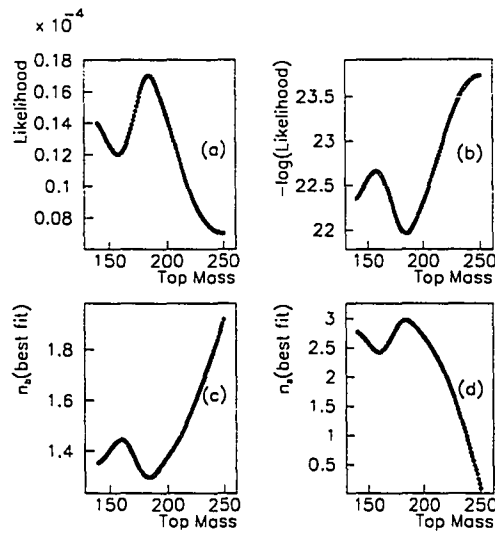


Figure 5.10: HERWIG result of fit for candidate events to the mass likelihood function. (a) Likelihood value. (b) $-\log(\text{likelihood})$. (c) Number of background events in best fit. (d) Number of signal events in best fit.

Chapter 6

Conclusions

A search for the top quark in the $t\bar{t} \rightarrow \mu + \text{jet}$ channel yields four observed events over an expected background of 1.40 ± 0.71 . The probability for the known backgrounds, alone, to explain the number of observed events is:

$$P(1.40 \pm 0.71 \rightarrow 4/\text{more}) = 0.0814, \quad (6.1)$$

corresponding to a 1.7σ effect in the gaussian approximation. Limited statistics provide calculated cross section values just above zero at the one standard deviation level, as presented in Table 4.8 and Figure 4.20; for example,

$$\sigma(m_{top} = 180 \text{ GeV}) = 5.4 \pm 4.4_{-1.2}^{+1.0} \text{ pb}. \quad (6.2)$$

An evaluation for the top quark mass is performed, using the transverse jet activity, H_T , in an event. The result from this mass analysis is:

$$m_{top} = 185_{-26}^{+16}(\text{stat.}) \text{ } _{-8}^{+6}(\text{syst.}) \text{ GeV}/c^2. \quad (6.3)$$

The excess number of observed events implying the existence for the top quark, its cross section, and the mass value are all consistent with the earlier reported results by the $D\bar{O}$ ¹ and CDF² collaborations, both derived from analyses including other channels as well. Those results and that concluded here are summarized in Table 6.1.

Table 6.1: Summary of discoveries of the top quark by DØ¹ and CDF,² with supporting evidence from this analysis.

DØ_{μ+jets} refers to the analysis presented here.

* The cross section is calculated by interpolating the results to $m_{top} = 185 \text{ GeV}/c^2$.

	Background Fluctuation Confidence Level (σ)	m_{top} (GeV/ c^2)	Cross Section (pb)
DØ ¹	4.6	$199_{-21}^{+19}(\text{stat.}) \pm 22(\text{syst.})$	6.4 ± 2.2
CDF ²	4.8	$176 \pm 8(\text{stat.}) \pm 10(\text{syst.})$	$6.8_{-2.4}^{+3.6}$
DØ _{μ+jets}	1.7	$185_{-26}^{+16}(\text{stat.})_{-8}^{+6}(\text{syst.})$	$5.3 \pm 4.4^*$

Appendix A

Verification of VECBOS MC Jet Activity With Data

The jet activity in the primary $W + \text{jet}$ background events is heavily relied upon for extracting a signal above the backgrounds and determining the top quark mass value. Specifically, H_T is an excellent variable in discriminating the top quark signal from its largest background, the $W + \text{jet}$ events, as seen in Figure 4.13. The analysis for the top quark mass is totally dependent on the success of a correct H_T modelling of this primary background; Figure 5.4 illustrates its importance.

The accuracy of the jet activity in $W + \text{jet}$ events produced by the VECBOS MC is checked in a comparison to real data with events containing $e + \geq 2$ jets and $e + \geq 3$ jets. Lepton universality implies identical results for the jet recoil against W bosons decaying to $\mu + \bar{\nu}_\mu$ or $e + \bar{\nu}_e$. Figure A.1 shows excellent agreement between the VECBOS MC and real data for $W + \geq 2$ jet and $W + \geq 3$ jet events.

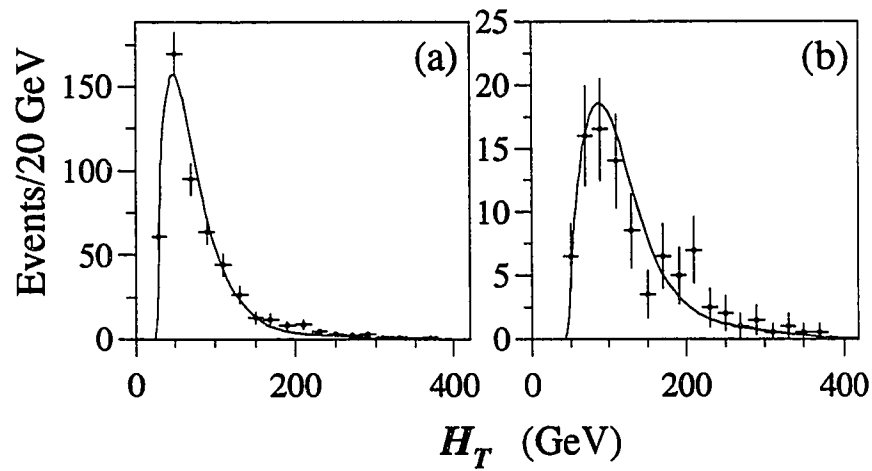


Figure A.1: Verification of VECBOS MC jet activity with data. The observed H_T distributions (points) agree with that predicted by the VECBOS MC (curve) in $W \rightarrow e+\text{jets}$ events for $\cancel{E}_T > 25$ GeV and (a) $e+ \geq 2$ jets and (b) $e+ \geq 3$ jets.¹

Appendix B

Comparison Between a Cut in \cancel{E}_T^{min} and a Contour Cut in $\Delta\phi(\vec{\mu}, \vec{\cancel{E}}_T) - \cancel{E}_T$ Space

Standard $D\bar{O} t\bar{t} \rightarrow \mu + \text{jet}$ analyses (with and without b-tags) use a complicated contour cut in $\Delta\phi(\vec{\mu}, \vec{\cancel{E}}_T) - \cancel{E}_T$ space to eliminate events having a muon with a very poorly measured momentum that artificially creates a large \cancel{E}_T in the event. The motivation for such a cut is provided by examining dijet events containing nonisolated muons which should have little \cancel{E}_T (relative to $t\bar{t}$ events). Real data events passing the two requirements:

1. at least two jets with $E_T \geq 15$ GeV
2. at least one *nonisolated* μ with $p_T \geq 15$ GeV/c ($\Delta R(\mu, \text{jet}) = 0.5$)

are entered in Figure B.1(a). Events with a wrongly measured muon momentum will have its true \cancel{E}_T modified parallel (anti-parallel) to the μ direction if the momentum is undermeasured (overmeasured). The $\sigma(\frac{1}{p})$ nature of the μ momentum error accommodates overmeasured muon momenta more readily than undermeasured ones, as illustrated in Table 4.1; this accounts for the events with very large \cancel{E}_T which have the μ and \cancel{E}_T back-to-back, having no large \cancel{E}_T counterpart with μ and \cancel{E}_T parallel. The result of a $\cancel{E}_T^{min} \geq 15$ GeV cut on this *nonisolated* muon real data sample is shown in Figure B.1(b), along with the anticipated effect of the contour cut on these surviving events. The consequence of the contour cut, derived from

the distribution in Figure B.1(a), on $\text{top}(m_{\text{top}} = 180\text{GeV}/c^2)$ MC is illustrated in Figure B.1(c). Application of an $\cancel{E}_T^{\text{min}} \geq 15 \text{ GeV}$ cut on the $\text{top}(m_{\text{top}} = 180\text{GeV}/c^2)$ MC, as shown in Figure B.1(d), demonstrates the similarity of a cut on $\cancel{E}_T^{\text{min}}$ to the more complicated contour cut. Table B.1 quantifies the results of two cuts on $\cancel{E}_T^{\text{min}}$ and the contour cut for the rejection against the dijet sample with poorly measured μ momenta and the efficiency for keeping $\text{top}(m_{\text{top}} = 180\text{GeV}/c^2)$ events. The quantitative outcomes are very similar, with a $\cancel{E}_T^{\text{min}} \geq 15 \text{ GeV}$ cut being slightly more efficient for $\text{top}(m_{\text{top}} = 180\text{GeV}/c^2)$ than the contour cut for the same background rejection.

Table B.1: Comparison between $\cancel{E}_T^{\text{min}}$ cut and contour cut for rejection of events with poorly measured μ momenta and efficiency of top quark events.

	Rejection Factor Against Dijet Sample	Efficiency For Top($m_{\text{top}} = 180\text{GeV}/c^2$)
Contour Cut	0.97	0.83
$\cancel{E}_T^{\text{min}} \geq 15 \text{ GeV}$	0.97	0.85
$\cancel{E}_T^{\text{min}} \geq 20 \text{ GeV}$	0.99	0.76

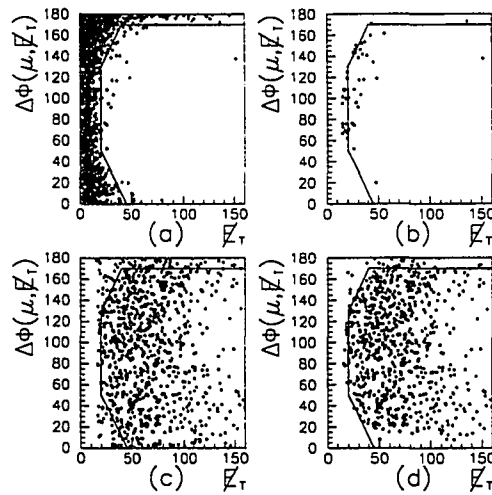


Figure B.1: Effect of E_T^{min} and contour cuts in $\Delta\phi(\vec{\mu}, \vec{E}_T)$ (degrees)- E_T (GeV) space for real data with a nonisolated μ and for top MC.

(a) Events are real data with *nonisolated* muons, passing the two requirements stated in the text. The contour cut is derived from this information.

(b) Subset of events in (a) passing a cut of $E_T^{min} \geq 15$ GeV.

(c) Events are top($m_{top} = 180\text{GeV}/c^2$) MC. Imposed on the top MC events were the cuts: an *isolated* muon with $p_T \geq 15$ GeV/c, four or more jets with $E_T \geq 15$ GeV, $E_T \geq 15$ GeV, and $E_T^{cal} \geq 15$ GeV.

(d) Subset of events in (c) passing a cut of $E_T^{min} \geq 15$ GeV.

Appendix C

Dependence of Optimal Selection Cut Values and Its Validity on $\int \mathcal{L} dt$

To demonstrate the dependence of the optimal selection cut values and its validity on the amount of data analyzed, another grid search is performed for $\int \mathcal{L} dt = 9.8 \text{ pb}^{-1}$. The resulting optimal cut values derived for both $\int \mathcal{L} dt$ values are given in Table C.1; the expected number of events for the signal ($\text{top}(m_{\text{top}} = 180 \text{ GeV}/c^2)$), backgrounds, and error in the backgrounds are provided in Table C.2. In the $\int \mathcal{L} dt = 9.8 \text{ pb}^{-1}$ case, the error in the background is larger than the anticipated signal, rendering the expectation of such a search meaningless.

Table C.1: Optimal cut values resulting from the Grid Search for two cases of $\int \mathcal{L} dt$.

Quantity	Optimal Cut Value For	
	$\int \mathcal{L} dt = 45.6 \text{ pb}^{-1}$	$\int \mathcal{L} dt = 9.8 \text{ pb}^{-1}$
$P_T(\mu)$	15 GeV/c	15 GeV/c
$\cancel{E}_T^{\text{cal}}$	50 GeV	15 GeV
\cancel{E}_T	15 GeV	15 GeV
$\cancel{E}_T^{\text{min}}$	15 GeV	15 GeV
$\cancel{E}_T^{\text{jet4}}$	15 GeV	15 GeV
H_T	160 GeV	110 GeV
\mathcal{A}	0.00	0.00

Table C.2: Expected number of signal and background events passing optimal cuts designed for two cases of $\int \mathcal{L} dt$.

	Number of Events For	
	$\int \mathcal{L} dt = 45.6 \text{ pb}^{-1}$	$\int \mathcal{L} dt = 9.8 \text{ pb}^{-1}$
$\langle N_{180 \text{ GeV}/c^2(\text{Top})} \rangle$	2.02	0.62
$\langle N(\text{All Backgrounds}) \rangle$	1.40	2.74
$\sigma(\text{All Backgrounds})$	0.71	0.83

Appendix D

Optimization Probability Projected In Pairs of Variables

The optimization probability (defined by Equation 4.11) projected in all possible pairs of variables is collected here. The remaining $N - 2$ variables are set to their optimal values as given in Table 4.4. In each Figure below are the contents:

- (a) probability in “forward” view,
- (b) probability in “reverse” view,
- (c) inverse of probability in “forward” view,
- (d) and inverse of probability in “reverse” view.

Recall that the optimal cut is at the *minimum* probability for the background to fluctuate and explain the background *and* signal existing. Since the minimum is difficult to see in these lego plots, the inverse probability is plotted to unveil the optimal location. The cut for each tower is denoted by the smallest values of its four corners.

Figures D.9(d) and D.19(d) have bins arbitrarily assigned an unphysical value of $\frac{1}{\text{Probability}} = 0.5$. The cuts corresponding to these bins have reduced discriminating power due to at least one of the following conditions:

- $N_2^{data} = 0$ (Equations 4.6 and 4.8)
- $N_3^{data} = 0$ (Equations 4.6 and 4.8)
- $N_{W+jets}^{VECBOS}(\text{pass norm cuts}) = 0$ (Equation 4.8)

- $N_{W+jets}^{VECBOS}(\text{pass all cuts}) = 0$ (Equation 4.8)
- $N_{QCD}^{jets}(\text{no } H_T, \mathcal{A} \text{ cuts}) = 0$ (Equation 4.9)
- $N_{QCD}^{jets}(\text{pass } H_T, \mathcal{A} \text{ cuts}) = 0$ (Equation 4.9)
- $N_{Z+jets}^{VECBOS}(\text{pass norm cuts}) = 0$ (Equation 4.10)
- $N_{Z+jets}^{VECBOS}(\text{pass all cuts}) = 0$ (Equation 4.10)

Furthermore, the same conditions were imposed on the data sets having their jet energies modified high and low; these extra data sets were used to estimate the error due to the jet energy scale uncertainty. Cuts represented by these bins are not considered in the optimization process.

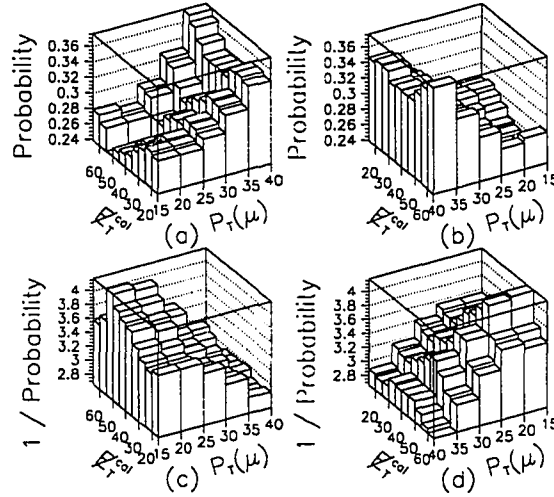


Figure D.1: Optimization probability for $H_T^{cal}(\text{GeV})$ vs. $P_T(\mu)(\text{GeV}/c)$.

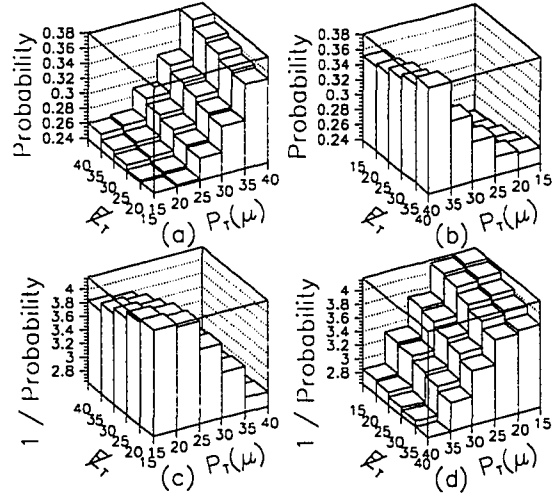


Figure D.2: Optimization probability for $\#_T$ (GeV) vs. $P_T(\mu)$ (GeV/c).

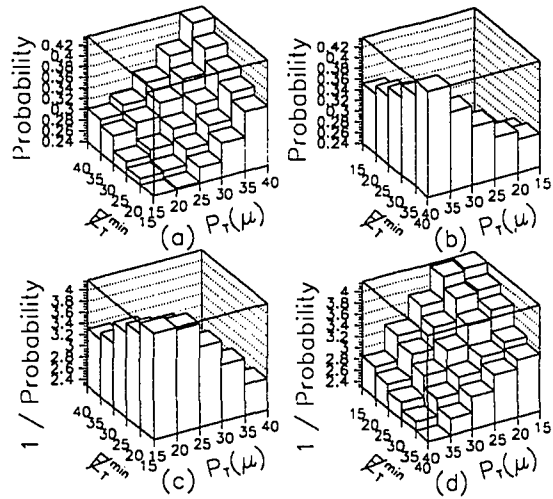


Figure D.3: Optimization probability for $\#_T^{\min}$ (GeV) vs. $P_T(\mu)$ (GeV/c).

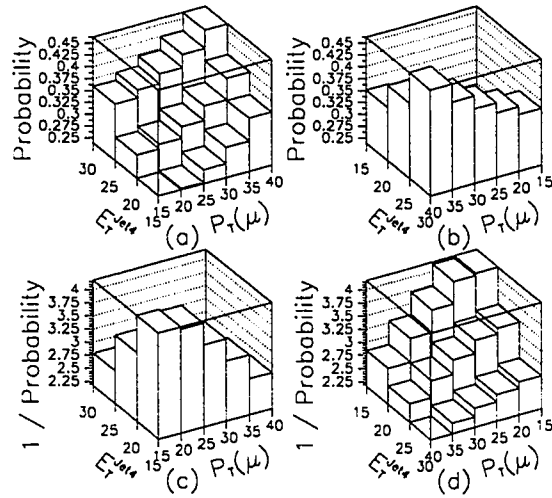


Figure D.4: Optimization probability for E_T^{jet4} (GeV) vs. $P_T(\mu)$ (GeV/c).

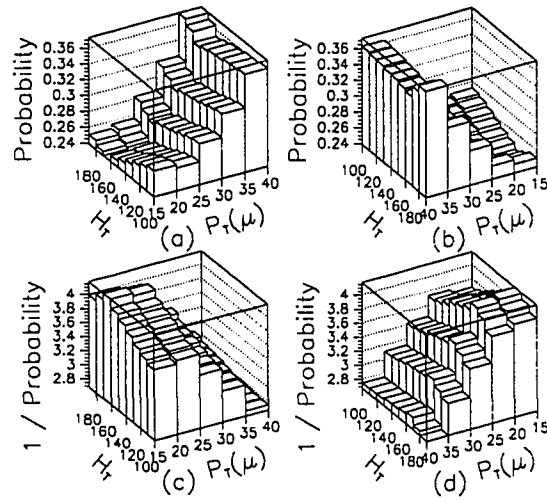


Figure D.5: Optimization probability for H_T (GeV) vs. $P_T(\mu)$ (GeV/c).

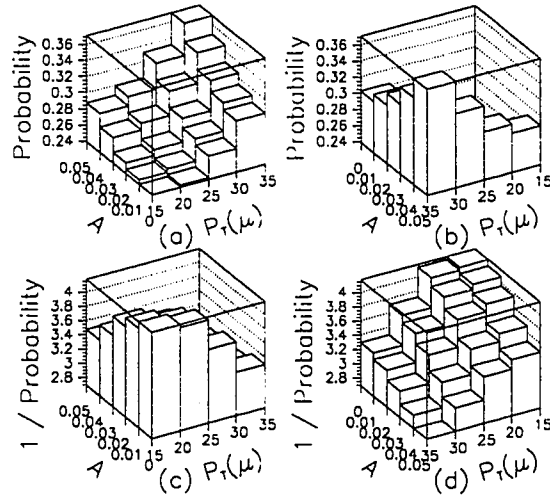


Figure D.6: Optimization probability for \mathcal{A} vs. $P_T(\mu)$ (GeV/c).

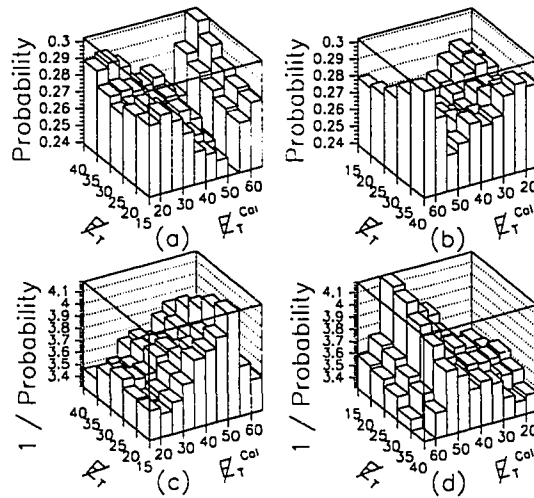


Figure D.7: Optimization probability for E_T (GeV) vs. E_T^{cal} (GeV).

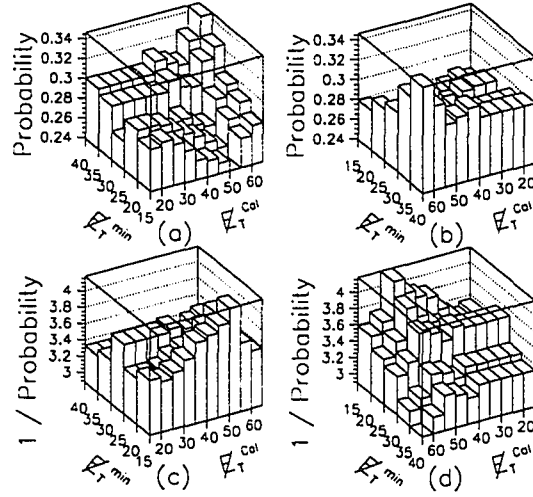


Figure D.8: Optimization probability for $E_T^{min}(\text{GeV})$ vs. $E_T^{cal}(\text{GeV})$.

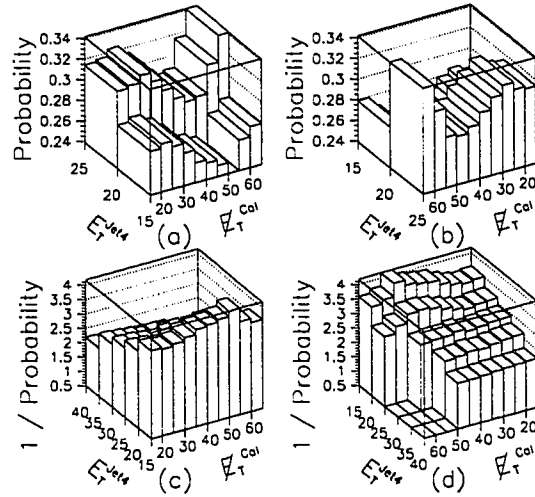


Figure D.9: Optimization probability for E_T^{Jet4} (GeV) vs. p_T^{cal} (GeV). Note that the E_T^{Jet4} range in (a) and (b) represent only two cuts at 15 and 20 GeV, while the range in (c) and (d) are 15 to 35 in 5 GeV increments. See the beginning of this appendix for an explanation of the unphysical bins in (d) with value $\frac{1}{\text{Probability}} = 0.5$.

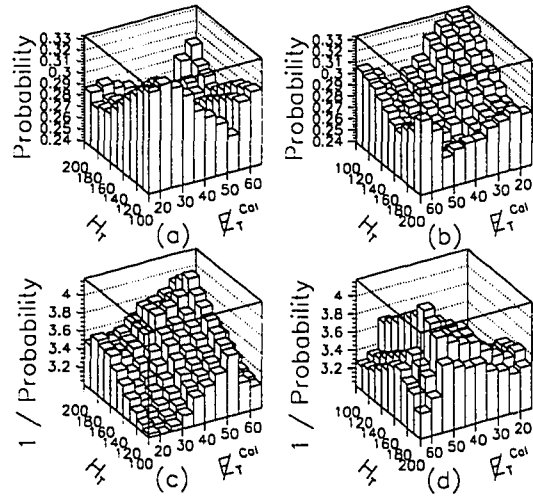


Figure D.10: Optimization probability for H_T (GeV) vs. E_T^{cal} (GeV).

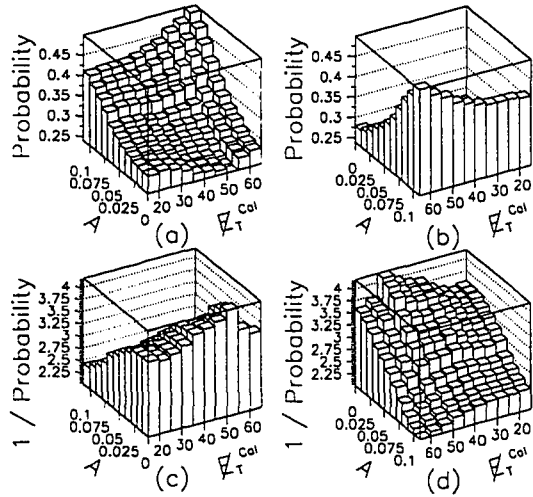


Figure D.11: Optimization probability for A vs. E_T^{cal} (GeV).

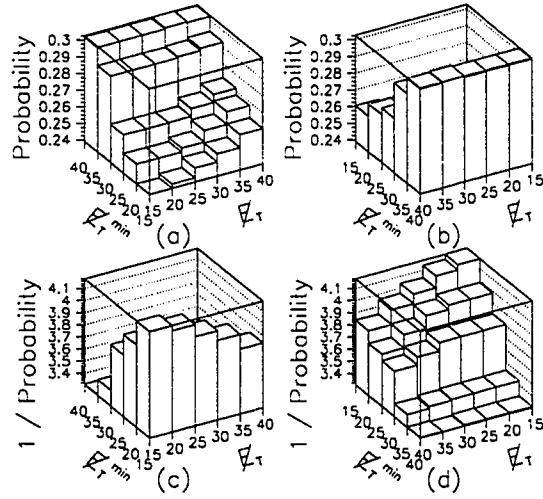


Figure D.12: Optimization probability for $E_T^{min}(\text{GeV})$ vs. E_T (GeV).

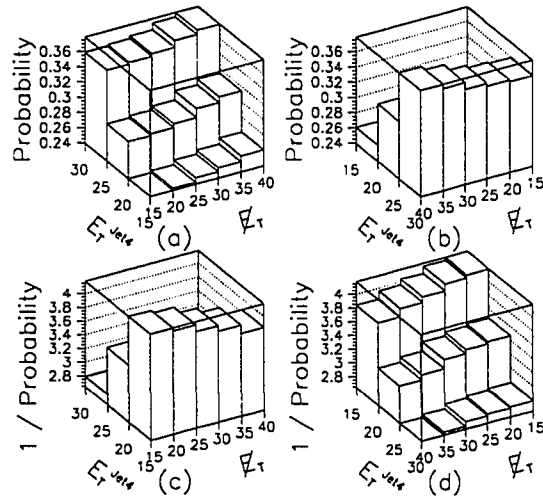


Figure D.13: Optimization probability for $E_T^{Jet4}(\text{GeV})$ vs. E_T (GeV).

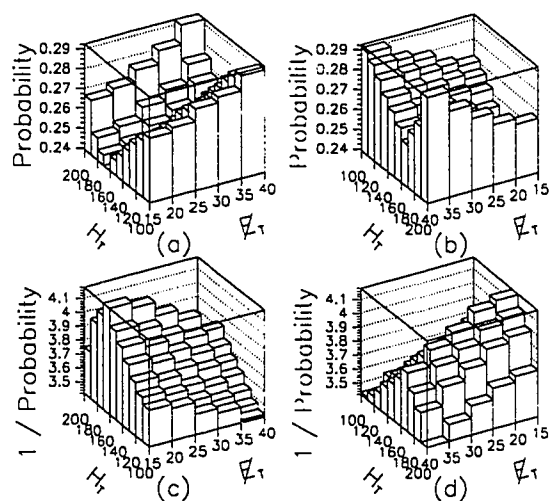


Figure D.14: Optimization probability for H_T (GeV) vs. E_T (GeV).

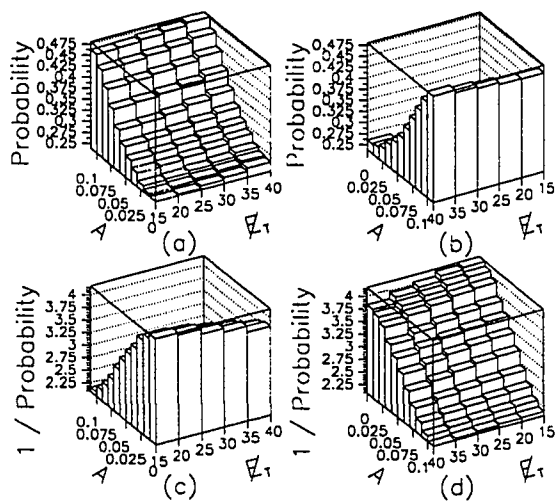


Figure D.15: Optimization probability for A vs. E_T (GeV).

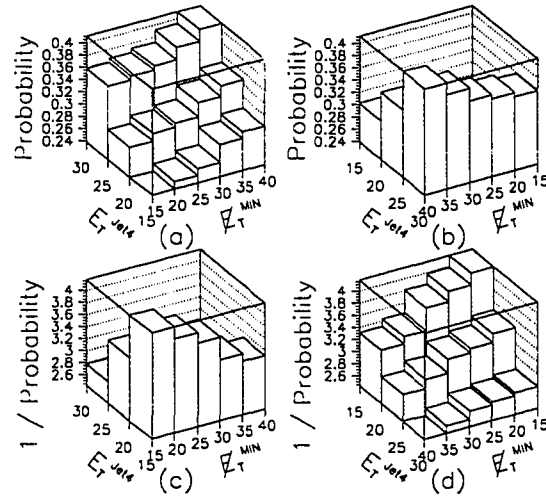


Figure D.16: Optimization probability for E_T^{Jet4} (GeV) vs. E_T^{min} (GeV).

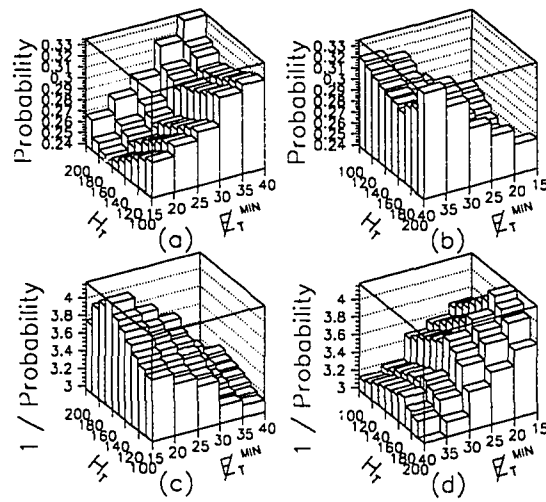


Figure D.17: Optimization probability for H_T (GeV) vs. E_T^{min} (GeV).

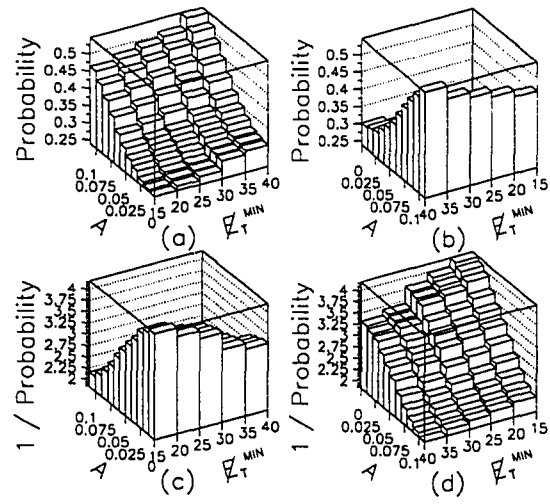


Figure D.18: Optimization probability for \mathcal{A} vs. E_T^{min} (GeV).

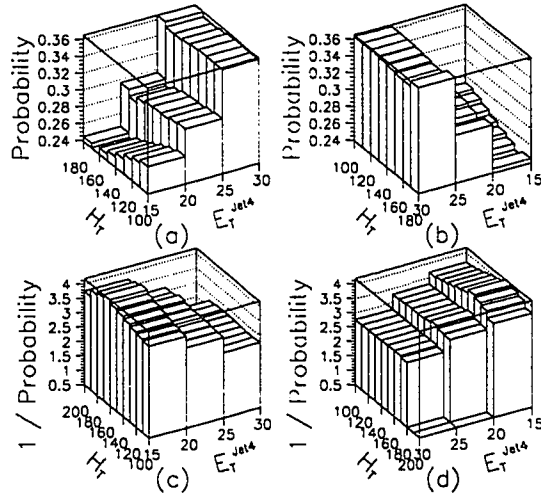


Figure D.19: Optimization probability for H_T (GeV) vs. E_T^{Jet4} (GeV).

Note that the H_T range in (a) and (b) represent cut values from 100 to 170 in 10 GeV increments, while the range in (c) and (d) are 100 to 190 in 10 GeV increments.

See the beginning of this appendix for an explanation of the three unphysical bins in (d) with value $\frac{1}{Probability} = 0.5$.

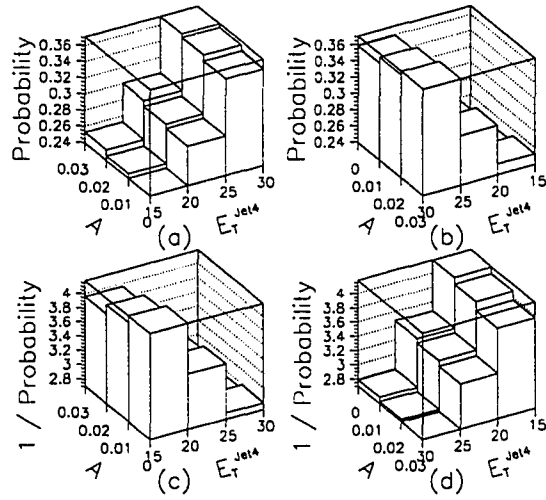


Figure D.20: Optimization probability for \mathcal{A} vs. E_T^{Jet4} (GeV).

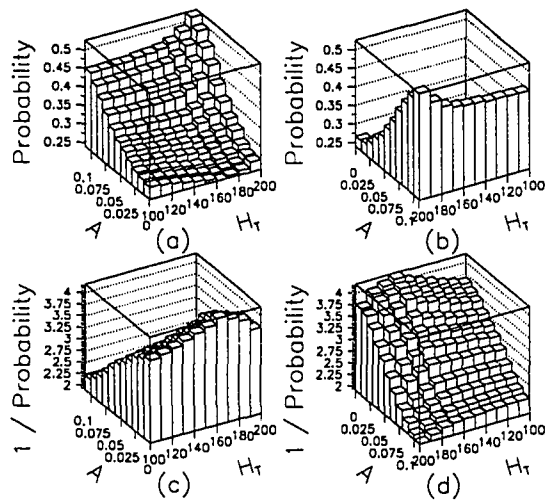


Figure D.21: Optimization probability for \mathcal{A} vs. H_T (GeV).

Appendix E

Candidate Events

The four-vector of all objects in the four candidate events are gathered in this appendix.

Table E.1: Four-vector of objects in Run 58192, Event 137.

Run 58192, Event 137				$H_T = 246.7$ GeV		
Object	p_x	p_y	p_z	E	E_T	η
Muon	-42.9	-62.3	-6.6	75.9	75.7	-0.09
\cancel{E}_T	-8.1	-77.2	-	77.6	77.6	-
Jet 1	46.4	126.0	84.8	160.7	134.3	0.60
Jet 2	32.9	23.4	47.6	62.7	40.3	1.00
Jet 3	-30.5	20.2	-10.0	38.7	36.6	-0.27
Jet 4	-8.9	-34.3	-75.8	83.8	35.5	-1.50
Tag μ	10.3	6.8	14.0	18.7	12.4	0.97

Table E.2: Four-vector of objects in Run 58203, Event 4980.

Run 58203, Event 4980				$H_T = 200.2$ GeV		
Object	p_x	p_y	p_z	E	E_T	η
Muon	-20.7	76.7	44.1	90.9	79.5	0.53
\cancel{E}_T	-38.8	29.8	-	48.9	48.9	-
Jet 1	22.2	-109.6	14.5	114.1	111.9	0.13
Jet 2	33.4	-13.9	10.7	38.3	36.2	0.29
Jet 3	11.3	31.9	54.6	64.5	33.8	1.26
Jet 4	-17.2	-6.3	-14.0	23.4	18.4	-0.70
Tag μ	12.6	-7.2	2.8	14.8	14.5	0.19

Table E.3: Four-vector of objects in Run 63183, Event 13926.

Run 63183, Event 13926				$H_T = 195.4$ GeV		
Object	p_x	p_y	p_z	E	E_T	η
Muon	56.9	10.8	19.2	60.7	57.6	0.33
\cancel{E}_T	22.6	-53.1	-	57.7	57.7	-
Jet 1	-16.7	58.0	-68.1	91.4	60.3	-0.97
Jet 2	-59.7	-5.2	-43.4	74.6	60.0	-0.67
Jet 3	-39.5	-20.5	-4.6	45.8	44.5	-0.10
Jet 4	23.0	20.1	-14.6	34.3	30.6	-0.46

Table E.4: Four-vector of objects in Run 82694, Event 25595.

Run 82694, Event 25595				$H_T = 247.3$ GeV		
Object	p_x	p_y	p_z	E	E_T	η
Muon	35.4	-40.1	-22.6	58.1	53.5	-0.41
\cancel{E}_T	32.8	27.6	-	42.9	42.9	-
Jet 1	-101.3	38.0	-12.6	110.2	108.2	-0.12
Jet 2	47.0	4.3	-96.7	108.1	47.2	-1.47
Jet 3	-19.7	-38.5	-2.0	43.7	43.3	-0.05
Jet 4	-28.5	5.8	-32.3	44.4	29.1	-0.96
Jet 5	5.5	18.8	24.5	31.6	19.6	1.05

Appendix F

Fitting Results For Most Probable Top Mass Values From Simulated Experiments

Collected here are the fits used to determine the most probable outcomes for the value of the top quark mass from simulated experiments as explained in Section 5.2.2.

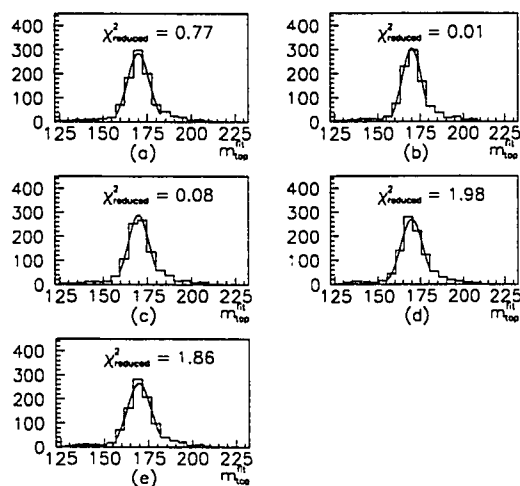


Figure F.1: Fits used in determining the most probable outcome for the 1000 simulated experiments generated with $m_{top} = 160 \text{ GeV}/c^2$. Bins in (a) are centered on multiple values of five. Bins in (b), (c), (d), and (e) are shifted to the right by 1, 2, 3, and 4 GeV/c^2 , respectively.

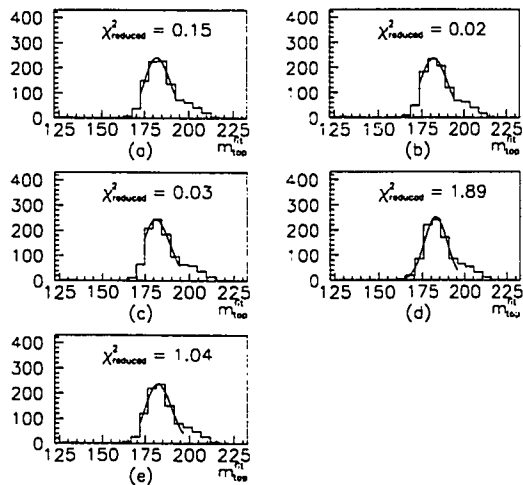


Figure F.2: Fits used in determining the most probable outcome for the 1000 simulated experiments generated with $m_{top} = 180 \text{ GeV}/c^2$. Bins in (a) are centered on multiple values of five. Bins in (b), (c), (d), and (e) are shifted to the right by 1, 2, 3, and 4 GeV/c^2 , respectively.

Table F.1: Means of fitted gaussian functions on simulated experiments generated with $m_{top} = 160 \text{ GeV}/c^2$. $m_{top}^{peak}(160)$ is the average of the peak values and is the estimate for the most probable m_{top} value. All entries are in GeV/c^2 .

Bin Offset	Peak Value
0	170.1
1	170.1
2	170.0
3	169.9
4	169.8
$m_{top}^{peak}(160)$	170.0

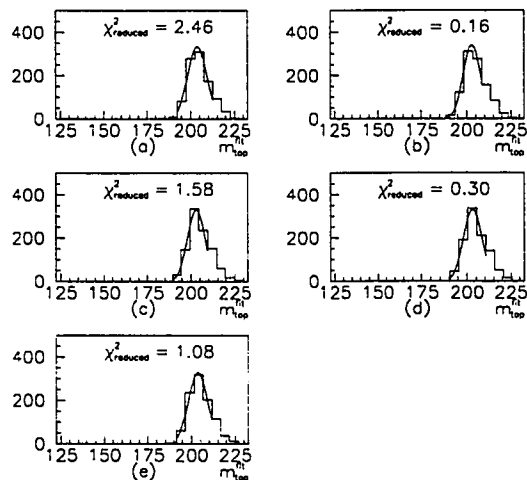


Figure F.3: Fits used in determining the most probable outcome for the 1000 simulated experiments generated with $m_{top} = 200 \text{ GeV}/c^2$. Bins in (a) are centered on multiple values of five. Bins in (b), (c), (d), and (e) are shifted to the right by 1, 2, 3, and 4 GeV/c^2 , respectively.

Table F.2: Means of fitted gaussian functions on simulated experiments generated with $m_{top} = 180 \text{ GeV}/c^2$. $m_{top}^{peak}(180)$ is the average of the peak values and is the estimate for the most probable m_{top} value All entries are in GeV/c^2 .

Bin Offset	Peak Value
0	182.2
1	181.8
2	181.3
3	182.7
4	182.5
$m_{top}^{peak}(180)$	182.1

Table F.3: Means of fitted gaussian functions on simulated experiments generated with $m_{top} = 200$ GeV/c². $m_{top}^{peak}(200)$ is the average of the peak values and is the estimate for the most probable m_{top} value All entries are in GeV/c².

Bin Offset	Peak Value
0	203.8
1	202.9
2	203.0
3	203.2
4	203.7
$m_{top}^{peak}(200)$	203.3

Bibliography

- [1] S. Abachi *et al.* (DØ). *Phys. Rev. Lett.*, 74:2632, April 1995.
- [2] F. Abe. *et al.* (CDF). *Phys. Rev. Lett.*, 74:2626, April 1995.
- [3] Particle Data Group, *Phys. Rev.* **D50**(3), 1173 (1994)
- [4] Francis Halzen and Alan D. Martin, "Quarks & Lepton: An Introductory Course in Modern Particle Physics," John Wiley & Sons, 1984.
- [5] Gordon Kane, "Modern Elementary Particle Physics," Addison-Wesley Publishing Co., 1993 (Updated Edition)
- [6] Gordon L. Kane and Michael E. Peskin, *Nucl. Phys.* B195, 29 (1982)
- [7] Bean *et al.* (CLEO), *Phys. Rev.* **D35**, 3533 (1987)
- [8] Albajar *et al.* (UA1), *Phys. Let. B.*, 163 (1991)
- [9] Private communication with Sandip Pakvasa.
- [10] E. Ma, *Phys. Rev. Lett.* **57**, 535 (1986).
- [11] S. Pakvasa, D. P. Roy, S. U. Sankar. *Phys. Rev.* **D42**, 3160 (1990)
- [12] The LEP Collaborations and the LEP Electroweak Working Group, CERN-PPE/94-187; Schaille D. In *XXVII th Int. Conf. on High Energy Physics*, IOP Publishing, (1995).
- [13] CDF and DØ preliminary results, Y. Ducros, Proc. of the conference: *Results and Perspectives in Particle Physics*, La Thuile, March 6-12, 1994;
M. Demarteau et al., Combining W Mass Measurements, CDF/PHYS/CDF/PUBLIC/2552 and DØ NOTE 2115.
- [14] UA2 Collaboration, J. Alitti *et al.*, *Phys. Lett.* **B276** (1992) 354.

- [15] CDHS Collaboration, H. Abramowicz *et al.*, Phys. Rev. Lett. **57** (1986) 298;
CDHS Collaboration, A. Blondel *et al.*, Z. Phys. **C45** (1990) 361.
- [16] CHARM Collaboration, J. V. Allaby *et al.*, Phys. Lett. **B177** (1986) 446;
CHARM Collaboration, J. V. Allaby *et al.*, Z. Phys. **C36** (1987) 611.
- [17] CCFR Collaboration, C. G. Arroyo *et al.*, Phys. Rev. Lett. **72** (1994) 3452.
- [18] SLD Collaboration, K. Abe *et al.*, Phys. Rev. Lett. **73** (1994) 25.
- [19] Plot generated by Marcel Demarteau using calculations from Halzen and Kniehl²⁰ and code from the LEP Electroweak Working Group.²¹
- [20] F. Halzen and B.A. Kniehl, Nucl. Phys. **B353** (1991) 567.
- [21] LEP Electroweak Working Group, ZFITTER Program, Version 4.8, (unpublished).
- [22] U. Heintz in proceedings of the LaThuile conference, March 96;
K. Streets in proceedings of the Moriond conference, March 96.
- [23] Wimpenny and Winer, "The Top Quark," Annual Reviews of Nuclear Particle Science **46** (1996), page numbers not yet assigned.
- [24] D. Strom. Precision Electroweak Experiments at LEP. Proceedings of the 1995 SLAC Summer Institute: The Top Quark and the Electroweak Interaction (1995)
- [25] DØ Collaboration, S. Abachi *et al.*, Phys. Rev. Lett. **72**, 2138 (1994)
- [26] E. Laenen, J. Smith, and W. van Neerven, "Top Quark Production Cross Section," FERMILAB-Pub-93/270-T,(unpublished, 1993).
- [27] E. Laenen, J. Smith, and W. van Neerven, Phys. Lett. **321B**, 254 (1994)
- [28] Lynne H. Orr, Phys. Rev. **D44**, 88 (1991)
- [29] Joey Thompson, "Introduction to Colliding Beams at Fermilab," Fermilab-TM-1909

- [30] DØ Collaboration, NIM, A338, 185 (1994)
- [31] Scott Stuart Snyder. "Measurement of the Top Quark Mass at DØ." PhD thesis, State University of New York at Stony Brook, Stony Brook, New York, May 1995.
- [32] William Joseph Thompson. "Search for the Top Quark in the Muon + Jets Channel at DØ." PhD thesis, State University of New York at Stony Brook, Stony Brook, New York, Feb. 1994.
- [33] Paolo Franzini, NIM, A289, 438 (1990)
- [34] C. Brown *et al.*, NIM, A279, 331 (1989)
- [35] H. T. Diehl, "Cosmic Ray Muon Rejection in the Level 2 Filter at DØ," DØ NOTE 1517, (unpublished);
H. T. Diehl, "Updates to Cosmic Ray Muon Rejection in MUON_L2," DØ NOTE 1517A, (unpublished)
- [36] UA1 Collaboration, G. Arninson *et al.*, Phys. Lett. **123B**, 115, (1983); Phys. Lett. **132B**, 21, (1983).
- [37] CDF Collaboration, F. Abe *et al.*, Phys. Rev. Lett. **69**, 2898, (1992).
- [38] N. Hadley, "Cone Algorithm for Jet Finding," DØ Note 904, (unpublished, 1989).
- [39] Bob Kehoe, "Determination of the DØ Jet Energy Corrections," DØ Note 2597, (unpublished, 1995)
- [40] Private communication with Rich Astur.
- [41] The LEP Collaborations ALEPH, DELPHI, L3, OPAL, and the LEP Electroweak Working Group, CERN-ppe/94-187, 1994.
- [42] S. Abachi *et al.*, Phys. Rev. **D52** 4877 (1995).
- [43] G. Marchesini *et al.*, Comput. Phys. Commun. **67**, 465, (1992)

- [44] C. Gerber *et al.*, “Muon Momentum Determination,” DØ Note 2140, (unpublished, 1994).
- [45] N. Amos *et al.*, “Change to the DØ Luminosity Monitor Constant,” FERMILAB-TM-1911, (unpublished, 1995).
- [46] F. Paige and S. Protopopescu, BNL Report no. BNL38034, 1986 (unpublished), release v 6.49.
- [47] W. Giele, E. Glover, and D. Kosower, Nucl. Phys. B403, 633 (1993)
- [48] F. A. Berends, H. Kuijf, B. Tausk, and W. T. Giele, Nucl. Phys. B357, (1991) 32.
- [49] Private communication with Joey Thompson.
- [50] Private communication with John Hobbs.
- [51] Private communication with Tom Rockwell.
- [52] C. Yoshikawa, “A Cookbook Recipe For Optimizing Cuts In New Particle Searches,” DØ Note 2570.1, (unpublished, 1995)
- [53] Jim Linnemann, “How Hard Should You Cut When the Data Sample is Finite?” DØ Note 2748, (unpublished, 1995)